INFORMATION TO USERS

This manuscript has been reproduced from the microfilm master. UMI films the text directly from the original or copy submitted. Thus, some thesis and dissertation copies are in typewriter face, while others may be from any type of computer printer.

The quality of this reproduction is dependent upon the quality of the copy submitted. Broken or indistinct print, colored or poor quality illustrations and photographs, print bleedthrough, substandard margins, and improper alignment can adversely affect reproduction.

In the unlikely event that the author did not send UMI a complete manuscript and there are missing pages, these will be noted. Also, if unauthorized copyright material had to be removed, a note will indicate the deletion.

Oversize materials (e.g., maps, drawings, charts) are reproduced by sectioning the original, beginning at the upper left-hand corner and continuing from left to right in equal sections with small overlaps.

Photographs included in the original manuscript have been reproduced xerographically in this copy. Higher quality 6" x 9" black and white photographic prints are available for any photographs or illustrations appearing in this copy for an additional charge. Contact UMI directly to order.

Bell & Howell Information and Learning
300 North Zeeb Road, Ann Arbor, MI 48106-1346 USA
800-521-0600

UMI®

Reproduced with permission of the copyright owner. Further reproduction prohibited without permission.

MORPHOLOGY AND PHOTOCATALYSIS OF TITANIUM DIOXIDE AEROGELS

by

Sean Kelly

A dissertation submitted to the Graduate Faculty in Physics in
partial fulfillment of the requirements for the degree of Doctor of
Philosophy, The City University of New York

2000

UMI Number: 9959193

UMI Microform 9959193

Bell & Howell Information and Learning Company
300 North Zeeb Road
P.O. Box 1346
Ann Arbor, MI 48106-1346

Approval Page

This manuscript has been read and accepted for the Graduate Faculty in Physics in satisfaction of the dissertation requirement for the degree of Doctor of Philosophy.

Dec 21, 1999 Micha Tomkiewicz

Date Professor Micha Tomkiewicz, Chair of Examining Committee

12/21/99

Date Professor Louis Celenza, Executive Director

Professor Pedro Montano

Professor Fred Pollak

Professor Fred Smith

Professor Ken Miyano

Supervisory Committee

The City University of New York

Abstract

MORPHOLOGY AND PHOTOCATALYSIS OF TITANIUM DIOXIDE AEROGELS

by

Sean Kelly

Advisor: Professor Micha Tomkiewicz

Pollution of our environment has become one of the most serious problems of this century. Titanium dioxide aerogels is composed of nanocrystallites of TiO_2 close-packed in roughly spherical mesospheres, which are agglomerated to form a highly-porous sponge. Aerogel morphology produces porosities of around 80% and surface area that can be as large as $1000 m^2/g$. The aerogels efficiently adsorb organic materials from the environment and when illuminated with UV light, decompose or oxidize the organic pollutants, ultimately to safe by-products such as CO_2 and H_2O.

In this work we modify the synthetic conditions to produce aerogels with different morphologies and measure the photocatalytic activity for photodecomposition of salicylic acid, as a function of size of the nanocrystallites. The results show that the quantum efficiency increases monotonically with the surface area and that the quantum efficiency per unit surface area increases linearly with the size of the nanocrystallites. These results are interpreted in terms of a “cracking model” of fixed size mesospheres and limited penetration of the salicylic acid into the mesospheres.

We use non-invasive, non-destructive techniques such as Raman scattering and EXAFS to follow the evolution of the TiO_2 structure as it is generated in the sol-gel, as well as changes in the structure after the aerogel is made and modified by annealing. Both techniques reveal structural information in the liquid and solid phases and enable us to monitor the crystallinity in the gelation process in a way that might lead to an ability to control the synthetic process and achieve a desired morphology.

Acknowledgments

I would like to begin by thanking my committee members for taking the time and energy to be a part of my Ph.D. process. Thanks to Professor Frederick Smith for serving on my committee and for being so flexible when it came to the difficult task of scheduling. Thanks to Professor Pedro Montano who assisted me with the EXAFS measurements and was still willing to sit on my committee. Professor Ken Miyano who is an inspiration to watch as he grows as an educator and as a mentor; thank you for the discussion and the willingness to be a part of my committee, and also for your help in analyzing the EXAFS data. Thanks also go to Professor Fred Pollak for his help on our Q-Vector Relaxation Model paper. One of the high points of my time as a graduate student was arguing with Fred about the positive dispersion curve for anatase, convinced that it was right, but hearing from him, "That's just not physical my boy." The joy I felt upon discovering that it was possible to have a positive dispersion convinced me that I need to be involved in making scientific discoveries. I am especially grateful to my boss, Professor Micha Tomkiewicz. The road that I have followed certainly has not been straight and easy. At times I felt as though I would never reach this point in my life. Micha kept me faithfully on the path and took part in my education in ways which I never expected. He is certainly the best mentor I could have ever asked for. I owe my dissertation to him, and also the years of learning that being in the lab has given me. Micha and Louise Hainline have both given me a great gift with their support, sensitivity and caring. Micha put me in charge of Laurie Ferguson when I was ambivalent about becoming involved, and I am ever so

grateful for that experience. Mentoring Laurie has truly shown me some of what Micha must have gone through with me.

Although I am officially a graduate of the Graduate School and University Center of CUNY, the Brooklyn College Physics department has been my home these many years. I have enjoyed the best treatment ever in the hands of Mary Shea, Ellen Wisloh, Suzanne Whiter and of course Laura Incampo, the woman who runs the Physics department office. Laura has been a supportive, almost motherly force in my life at Brooklyn College, and I truly cherish my experiences with her. Not to forget the faculty of the Physics department. I am grateful for and would like to thank Professor Al Bond for being a mentor as I began to teach physics, and Professor Peter Lesser for the support and encouragement to begin teaching. I would also like to thank Professor Ming Liou for all his help over the years. He never seemed to lose patience with me. And not to forget Professor Larry Mendelsohn for bringing me to Brooklyn College in the first place. The many other faculty members here have enriched my experience and I am happy to finally be able to call them colleagues. I would also like to acknowledge the support of The Department of Energy, NY State Center for Advanced Technology and NASA for funding my research all these years. My thanks also go to Megan Gibbs and Professor Robert Alfano for all their kind support.

In another area of my life, but equally important are my wonderful friends and family. When I was missing faith in myself, my good friend, Tuan-Anh Cao Tran gave me his love and support to sustain me through a very difficult period of my life. Anh has also constantly pushed me to finish this work, knowing that this is just a prelude for the career that I have before me. Todd Holden obviously is a very close friend whom I cherish for his insight and clarity, and all the discussions in physics that actually helped me to understand more. I also would like to thank him for being such a wonderfully caring person. His friendship and support also proved invaluable to me. I also need to thank my good friend Simeon Doytchinov for his love and support. He has been steadfast and true all these years and I will cherish his friendship for many years to come.

Through all of this I have had the constant love and support of my family. I have enjoyed frequent visits from my brother Rob and his wife Ronna, as well as their gentle encouragement to finally go out into the real world. My brother Charles and his wife Angela have given me love and support and can truly appreciate how difficult this has been for me. Closer to home, I would like to thank and acknowledge my extended family here in New York for all their love and support: Joe and Laura and Colin Couillard, Joan Larsen, and the Garcia girls, Mairi and Maite. They have all made my life better and made it possible for me to finish this work

I would also like to thank in no particular order various people who have helped me in some way over the years: Wu-Mian Shen, GLMKS Kahanda, Zhu Zhu, Geula Dagan, Jonathan Margalit, Vladimir Asnin, Lyudmila Malikova, Jun-Zuo Wan, Sean Eagleton, Ed Look, Richard Belgrave, Sasha Gorer, David Daitch, Ada Rubin, Sheldon Clarke, Lumis Turell, Louis Tundis, Wojtiech Krystek, and Roland Scal. And not to forget, my prodigy student, Laurie Ferguson, who helped me to understand how important teachers are in our lives. They mold us in ways that cannot be measured merely by exams or grades, but only in the greater scope of our lives and the subtle or not so subtle variations in our paths.

I need to take a special moment to thank the one person who will finally be glad to not have to do paperwork for me anymore, Florence Kempner. Over the years Florence has helped me too many times to count, and I am grateful for her help, love and support.

I would like to thank my parents for the gift of my life. They made it possible for me and encourage me to pursue my dreams. From my mother I learned my desire for Truth, and a desire to be True to myself. From my inventive father I have grown to love working with my hands and to understand how things work and how to fix them.

Of course, more than anyone else in the whole world, I wish to acknowledge the love and support of my darling Mary Ellen Shea, soon to be Kelly. She was a friend to me for many years before our love blossomed and now she has become my muse. Inspiration flows easily from her lips and by her actions she remains to me a mighty example that I strive to equal. Her love has made me much stronger.

Thank you,

Sean Kelly

December 17, 1999

Table of Contents

MORPHOLOGY AND PHOTOCATALYSIS OF TITANIUM DIOXIDE AEROGELS i

Approval Page ii

Abstract iii

Acknowledgments v

Table of Contents ix

List of Tables xi

List of Figures xii

Chapter 1 - Introduction 1

Chapter 2 - Background 7
- TiO_2 Introduction 7
- TiO_2 Applications 10
- TiO_2 Photochemistry 14
- TiO_2 Nanocrystalline Solar Cells 16
- TiO_2 Aerogels 18
- Synthesis of TiO_2 Aerogels 21
- Characterization of TiO_2 Aerogels 22
- Monitoring gel formation 28
- Objective 29

Chapter 3 - Synthesis of TiO_2 Aerogels 30
- Chemical Synthesis 30

Chapter 4 - SEM and TGA\SDT 51
- SEM 51
- TGA\ SDT 55
  - Scanning Differential Thermometry 56

Chapter 5 - Raman Spectroscopy 60
- Theory of Raman Scattering in Crystals 60

Results 76
Raman Scattering in liquids 89

Chapter 6 - Extended X-ray Absorption Fine Structure 98
EXAFS Background 98
Results 111

Chapter 7 - Photocatalysis 115
Theory of Photocatalysis 115
Experimental Procedure 117
Experimental Results 119
Dark Adsorption 119
Interpretation 127

Chapter 8 - Conclusions and Future Work 131

Appendix 1 - Self-Organizing Aerogel 134

References 159

List of Tables

1-1 Morphological comparison of aerogel, powder and single crystal 5

3-1 Densities and molar masses of TiO_2 sol gel reactants 32

3-2 Volumes of reactants needed for a 1:25:3.5:0.08 TiO_2 gel 33

3-3 Measured and calculated surface area for TiO_2 aerogels and Degussa P25 40

5-1 Raman optical modes of anatase TiO_2 70

6-1 Number of nearest neighbors and average bond length for the sol-gel evolution . . 111

7-1 Salicylic acid surface coverage for TiO_2 aerogels and Degussa P25 120

List of Figures

1-1 Exxon Valdez Oil Spill 2
1-2 Solar Kidney 4

2-1 Titanium Dioxide - electrolyte energy band diagram 8
2-2 The anatase crystal structure 9
2-3 The rutile crystal structure 9
2-4 Super hydrophilic TiO_2 tiles 13
2-5 Electron hole pair creation in a TiO_2 nanocrystal 15
2-6 Schematic of the Grätzel solar electrochemical cell 17
2-7 Aerogel - "Solid Smoke" 20
2-8 Schematic of TiO_2 aerogel 23
2-9 Typical X-ray spectra of TiO_2 aerogel 24
2-10 Typical BET absorption Isotherm 26
2-11 The TiO_2 has two important length scales 27

3-1 Path in P-T space for super-critical drying 38
3-2 X-ray spectra for raw aerogel 39
3-3 X-ray spectra for aerogel baked at 500C 41
3-4 X-ray spectra for aerogel baked at 700C 42
3-5 UV absorption for aerogel wash water 44
3-6 TGA for unwashed aerogel 45
3-7 TGA for unwashed near 200C 47
3-8 TGA for washed aerogel 48
3-9 SDT of unwashed aerogel 49
3-10 SDT of washed aerogel 50

4-1 SEM image of raw aerogel 53
4-2 SEM image of aerogel baked at 900C 54
4-3 SDT of washed aerogel 57
4-4 Closeup of the 709C peak 59

5-1 Backscatter Raman setup 62
5-2 Ring of atoms for phonon dispersion 63
5-3 Positive phonon dispersion 66
5-4 Negative phonon dispersion 66
5-5 Raman spectra of anatase 71
5-6 Raman spectra of rutile 72
5-7 Raman spectra of Degussa P25 73
5-8 Raman spectra of aerogel 74
5-9 Raman spectra of aerogel heated to 500C 74
5-10 Raman spectra of aerogel heated to 700C 76

5-11 Raman spectra of aerogel heated to 900C 76
5-12 Raman 145cm^{-1} peak for large and small crystallite 77
5-13 Fractional Raman shift versus crystallite size 78
5-14 FWHM versus crystallite size 79
5-15 Fractional FWHM versus Fractional Raman shift 80
5-16 Simulated Raman 145cm^{-1} peak for large and small crystallite 82
5-17 Simulated Raman spectra for size distribution, mean of $2a_L$ 84
5-18 Simulated Raman spectra for size distribution, mean of $5a_L$ 85
5-19 Fit of simulation to FWHM versus (crystallite size)$^{-1}$ 86
5-20 Fit of simulation to Raman shift versus (crystallite size)$^{-1}$ 87
5-21 Raman setup for liquid/gel samples 90
5-22 Raman spectra of Ethanol 91
5-23 Raman spectra of sol at five minutes 92
5-24 Raman spectra of sol at sixty minutes 93
5-25 Raman spectra of gel at 275 minutes 95
5-26 Lorentzian fit of gel peak at 200cm^{-1} 96

6-1 X-ray emissions and absorption edges as designated by Sommerfeld 98
6-2 EXAFS is a result of nearest neighbor atom interference 99
6-3 EXAFS for crystalline and "fine-size" anatase 100
6-4 The EXAFS spectra are affected by number, distances of nearest neighbors 102
6-5 Raw EXAFS for TIP 105
6-6 $X(k)$ for TIP 107
6-7 Fourier transformed $k^3 \cdot X(k)$ for TIP 108
6-8 Back Fourier transform of first peak in TIP FT 109
6-9 XANES spectra of the TiO_2 sol-gel 113

7-1 Apparatus for photocatalysis experiments 117
7-2 Dark adsorption of salicylic acid 119
7-3 Concentration of SA during illumination 122
7-4 Hg lamp spectrum 123
7-5 Quantum efficiency versus BET surface area 124
7-6 Normalized quantum efficiency versus crystallite size 125
7-7 Schematic of fragmentation model 127
7-8 Differential coverage of mesospheres 129

Chapter 1 - Introduction

On March 24, 1989, the Exxon tanker Valdez ran aground on the Bligh Reef in Prince William Sound spilling 11.2 million gallons of oil into the ocean. In a titanic effort to cleanup the polluted waters, Exxon spent more than three billion dollars, over the next two years, to cleanup the oil and recover habitats damaged by the spill, as well as to convince the public that it has dedicated itself to making right what went so wrong on that fateful day[1]. More than 10 years later, Exxon continues to maintain a visible presence in Prince William Sound, especially on the world wide web (WWW) where there is a web site (Figure 1-1) devoted to the accident, the clean-up efforts, and public research related to the accident. Public interest has remained high as an informal search of the WWW turned up more than 1,000 different sites related to the Valdez oil spill or the remuneration effort in Prince Edward Sound[2].

The Valdez incident is just one of the many accidents which cause untold damage to our natural resources. The effect of the Valdez accident is still being assessed, and some of the damage to fish and other wildlife populations is only now being recognized. What is needed in cases like the Valdez is a “smart sponge”. A “smart sponge” floats on the surface of a polluted ocean, lake or river and adsorbs pollutants. The “smart sponge” is a semiconductor that absorbs sunlight creating electron-hole pairs and utilizes the charges to decompose the pollution into benign by-products. When the pollution is finally gone, the “smart sponge” can be scooped up and used another day. Titanium Dioxide aerogels

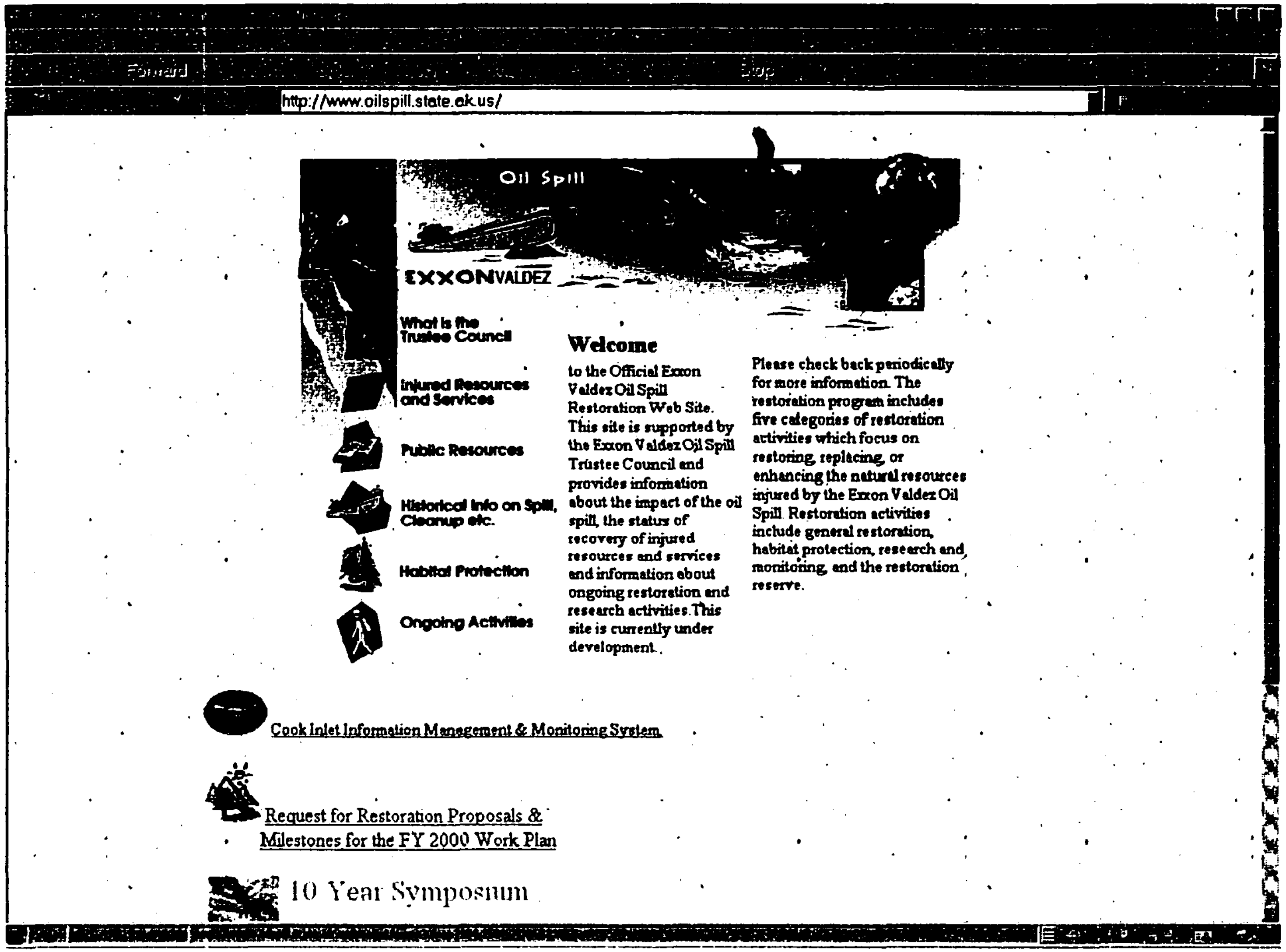

Welcome

to the Official Exxon Valdez Oil Spill Restoration Web Site. This site is supported by the Exxon Valdez Oil Spill Trustee Council and provides information about the impact of the oil spill, the status of recovery of injured resources and services and information about ongoing restoration and research activities. This site is currently under development.

Please check back periodically for more information. The restoration program includes five categories of restoration activities which focus on restoring, replacing, or enhancing the natural resources injured by the Exxon Valdez Oil Spill. Restoration activities include general restoration, habitat protection, research and monitoring, and the restoration reserve.

Figure 1-1 The Exxon webpage for the Valdez disaster is a beautiful example of what money can buy. It remains to be seen if they have in fact ameliorated the harm done by mucking up Prince Edward Sound.

can act as such a sponge.

As part of the Valdez cleanup, a commercial titanium dioxide powder called Degussa P25 (P25) was used to photocatalytically decompose some of the oil pollution[3]. This was an effective technique, but the material was lost at the end of the process. Titanium dioxide aerogel has been shown to be far superior to P25 in the photocatalytic decomposition of pollutants and it floats!

Aerogels, discovered only in this century, have become a sort of wonder material, holding records in 3 different material properties: density, porosity, and surface area. Aerogels have lower densities than any other person-made material, as low as 0.05 g/cm^3 . Aerogels are very porous as well, with total porosity of as much as 97%. The final remarkable property is the aerogel surface area which is a million or more times larger than a similar mass single crystal. Aerogels are remarkable in these properties, as well as the fact that their basic building blocks are nanocrystals as small as a few crystal lattices across. A comparison of the surface area, porosity and density of TiO_2 single crystal, Degussa P25 powder and aerogel is shown in Table 1-1. With their low densities aerogels can float on the surface of a polluted body of water and oxidize organic pollutants, acting as a kind of "solar kidney"(Figure 1-2)[4].

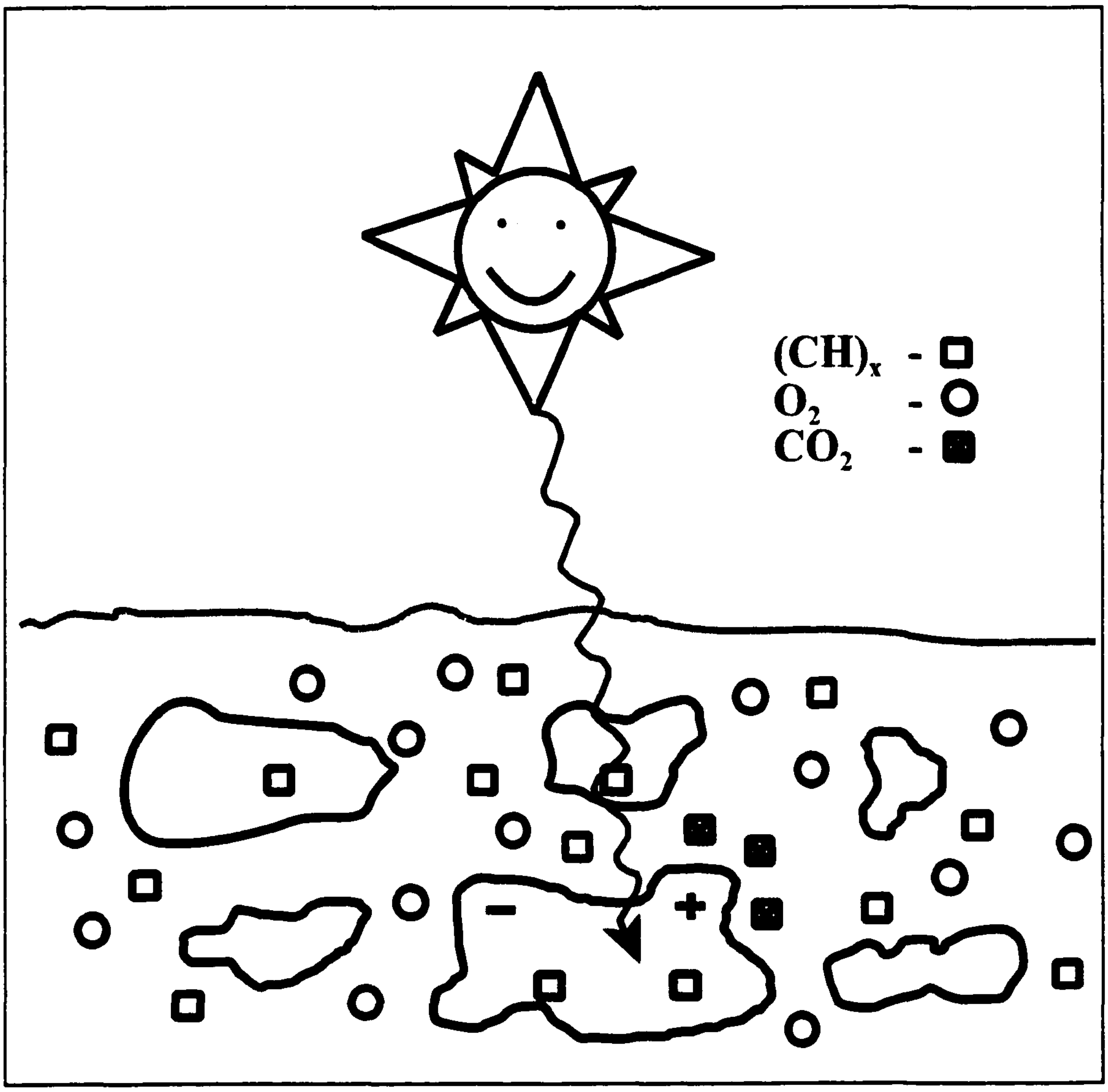

Figure 1-2 The monolithic TiO_2 aerogel (grey), acts as a “solar kidney” adsorbing organic pollutants and eventually decomposing them to CO_2 and H_2O.

TiO_2	BET Surface Area (m^2/g)	Porosity (%)	Density g/cm^3
Single Crystal	10^{-4}	0	3.79
Degussa P25 powder	50	10	0.5
Aerogel	700	97	0.05

Table 1-1: Comparison of various morphological parameters for TiO_2 single crystal, Degussa P25 powder and Aerogel.

Bulk rutile is a semiconductor with a band-gap of about 3.0eV. If bulk rutile is placed in an aqueous environment and illuminated, electron-hole pairs are created. The holes drift to the surface become powerful oxidizers as their potential is 3.0eV below that of a H+ electrode. This effect is not only responsible for the photocatalytic ability of the aerogels, but has also proven useful in the creation of the Grätzel cell, a titanium dioxide solar cell.

Aerogels are made through sol-gel chemistry, and it is clear that in order to fully take advantage of aerogels, it is necessary to understand how they form and how their morphology can be controlled in the synthetic process. The focus of this work has been to modify the morphology of titanium dioxide aerogels through synthetic conditions and to monitor those changes in a non-destructive way as a means of further understanding the aerogel growth and evolution. The techniques used to monitor the aerogel were Raman spectroscopy and Extended X-ray Absorption Fine Structure. These two techniques can in principle be used to monitor the sol-gel evolution through drying and also the aerogel structure after drying of the gel.

We hope that by understanding the titanium dioxide aerogel morphology that the photocatalytic ability of the aerogel can be optimized.

Chapter 2 - Background

TiO_2 Introduction

For many years, titanium dioxide in the form of rutile has been used as a photocatalytic substrate[5]. Rutile is an indirect band-gap semiconductor with a band-gap of about 3.0eV for bulk material[6,7]. In addition Rutile has behavior like that of a direct band-gap semiconductor[8]. When rutile is illuminated with photons of energy greater than the band-gap, electron-hole pairs are created. When bulk rutile is in contact with an electrolyte, bending of the valence band causes the holes to drift to the surface of the crystal, where they can oxidize materials absorbed on the surface and catalytically break them apart. From the electrochemical energy band diagram shown in Figure 2-1, the created holes have an oxidizing potential of at least 3eV below the potential of H^+. This oxidizing potential energy is sufficient to break even the strongest organic bonds. There is another less common form of titanium dioxide known as anatase.

Rutile and anatase are both tetragonal. The structure of anatase (Figure 2-2) and rutile (Figure 2-3)[9] both show a six-fold coordination of oxygen around each titanium atom. Oxygen-deficiency in the structure of rutile and anatase means that they are also both n-type semiconductors. Rutile belongs to the symmetry group D_{2h} while anatase belongs to D_{2d}[10]. From the pictures it is clear that rutile is packed more densely than anatase. There are other known phases of titanium dioxide, including Brookite and exotic forms of high-pressure and high-temperature TiO_2. While rutile is fairly common, it is impossible to

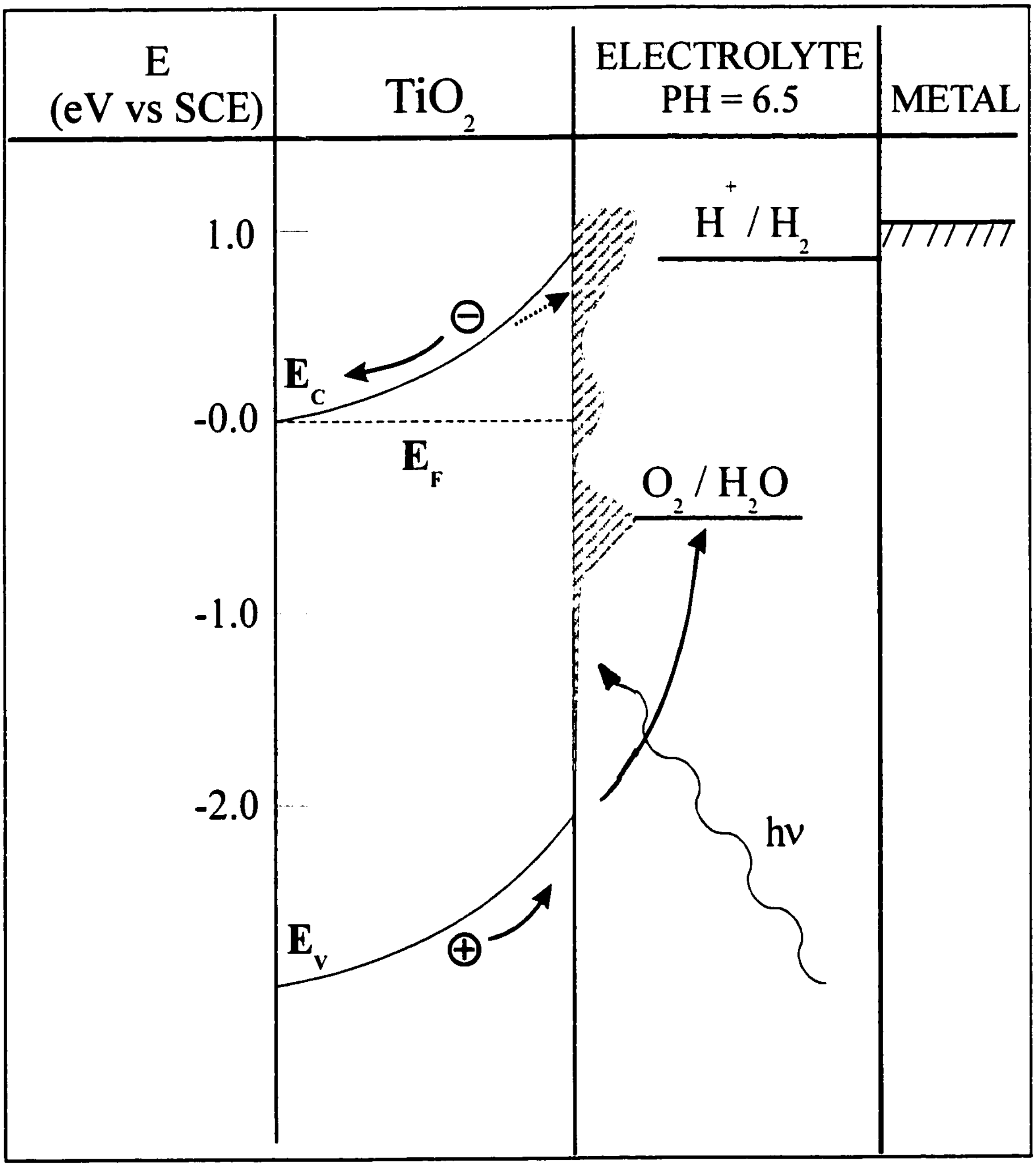

Figure 2-1 Schematic of the single crystal TiO_2 - electrolyte band structure. Surface states are represented by the shaded region.

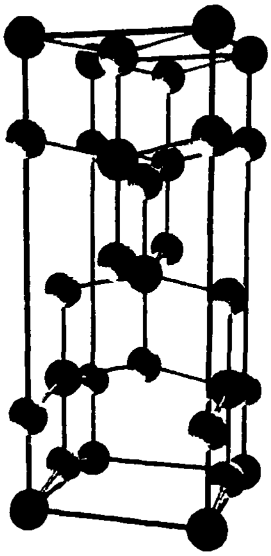

Figure 2-2 The crystal structure of anatase, with titanium(black) and oxygen(white). The atoms are not drawn to scale.

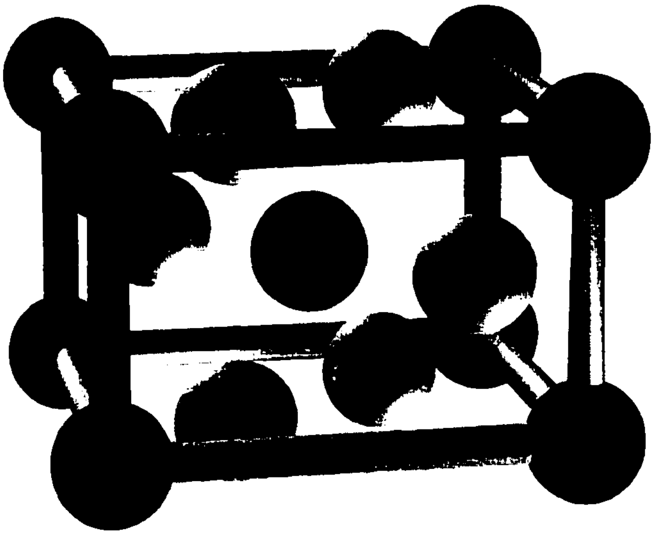

Figure 2-3 The crystal structure of rutile, with titanium(black) and oxygen(white). The atoms are not drawn to scale.

buy large, pure single crystals of anatase, and it is rather difficult to obtain them at all. In 1992, a group at the EPFL in Lausanne, Switzerland under the supervision of Michael Grätzel, created the largest undoped single crystals of anatase, about 5mm x 5mm in size. The crystals were made by chemical transport deposition[11]. The author has obtained a few small single crystals (≤ 2mm x 2mm) that were used for measurement of the single crystal Raman spectra of anatase.

Until 1992 very few experiments with titanium dioxide dealt specifically with the anatase phase. Although the x-ray diffraction spectra and the Raman spectra were partially known, only a few theoretical papers on the structure of anatase had been published[12,13]. It was thought (incorrectly) that anatase would be similar in electrical and chemical properties to rutile. The Lausanne group conducted experiments to determine the electrical properties of anatase and found that they were significantly different than rutile. The band structure of anatase also appears to be different with a band-gap of ~3.2eV for anatase and only 3.0eV for rutile. The charge transport properties also appear to be different.

TiO_2 Applications

Titanium dioxide is a remarkably common and frequently used material in the world around us. Titanium dioxide is attractive as an ingredient in commercial products because it is non-toxic, and behaves chemically like sand (SiO_2) in the body. The band-gap energy of about 3eV corresponds to photons of UV light which means that TiO_2

readily absorbs UV radiation. It is this property of TiO_2 which makes it especially useful in sun screens and paints, by absorbing UV radiation before it can damage our skin or our cars or houses. Titanium dioxide can also be found in items such as paint, paper and plastic, where it excels as a reflector of visible light because of its high refractive index (2.73) in the visible portion of the spectrum. Dupont is the world's leading supplier of TiO_2 pigments for paper, plastics and optical coatings[14] with their Ti-Pure line of products. They supply more than 50,000 tons annually for world consumption.

More recently, titanium dioxide has even found it's way into some more unusual products; as an ingredient in ceramic tiles and toilet seats. Produced by the Japanese company, TOTO , the tiles and toilet seats act as photocatalytic substrates, decomposing organic material like bacteria, mold and fungus which sit on the surface. Remarkably these materials can even function under very low illumination[15], which means they can be used indoors without needing separate UV illumination. The TiO_2 can be added as a thin film on other substrates, for example a UV-absorbing coating for glass, ceramic or even metals. It is possible to make a glazed window that uses the TiO_2 to absorb UV radiation, invisibly protecting the interior of our homes. The TiO_2 used in tiles and toilet seats works because when UV light irradiates the surface, a surface charge is generated which is capable of tearing apart any biological organisms on its surface. In Japan, TOTO has already created the first TiO_2 tiled operating room which is automatically sterilized clean under illumination. Curiously enough, these TiO_2 tiles have also been shown to be super-hydrophilic after irradiation with UV light. The super-hydrophilic surfaces are excellent anti-fog surfaces which work differently than other anti-fog coatings. Typical anti-fog surfaces are hydrophobic and work by repelling water vapor so that it will not condense on the surface. The droplets of condensation are the fog. The irradiated TiO_2 tiles are super-hydrophilic, so that when a droplet condenses on the surface, it is quickly pulled into a thin film which is effectively invisible (Figure 2-4).

In an aqueous environment the TiO_2 will break down organic compounds into smaller and smaller compounds, leaving as the final products CO_2 and H_2O. Titanium Dioxide is already being used in some third-world nations, especially in remote regions, for the decontamination of drinking water. Using solar energy as it's UV energy source the TiO_2 is activated and can easily breakdown bacteria and other organic impurities in drinking water[16].

The TiO_2 can also be used in gas phase catalysis, as demonstrated in a novel air scrubber produced by Marc Anderson[17] in collaboration with NASA and Kes Irrigation Systems. NASA was interested in finding a method for preserving fruits and vegetables for long space flights. The ripening process is triggered and accelerated by the presence of ethylene gas, so filtering the ethylene from the air would prevent foods from spoiling so quickly. Anderson's air scrubber utilizes glass beads coated with TiO_2 and irradiates the beads with UV light to decompose the ethylene gas into CO_2 and H_2O. In principle, the glass beads will never wear out and will only be replaced if they are somehow broken.

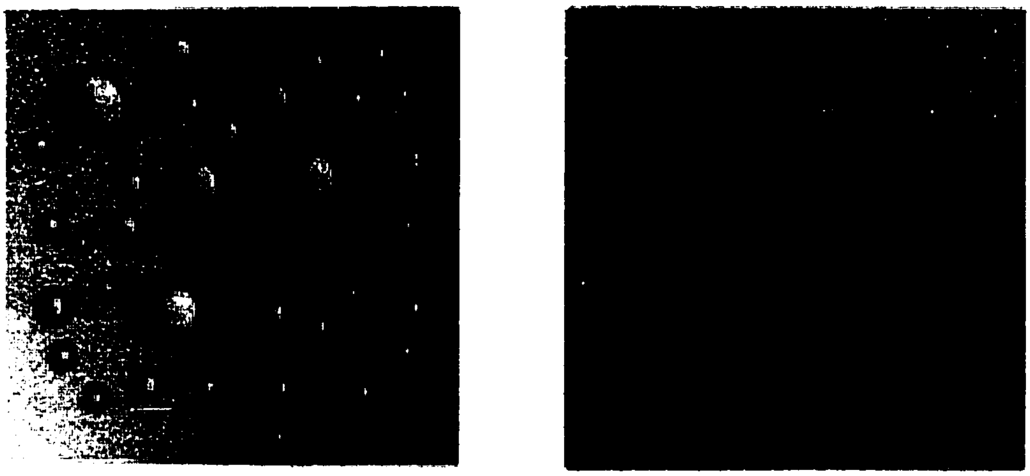

Before (droplets form)

After (no droplets)

Figure 2-4 A TiO_2 coated surface before and after illumination with UV light. After irradiation the surface is super hydrophilic and causes the condensed droplets to spread into a nearly invisible thin film.

Anderson's air scrubber has been proven so successful that it can extend the shelf life of fruits, vegetables and flowers from one to four weeks.

TiO_2 Photochemistry

The ability of TiO_2 to photocatalytically decompose organic pollutants is understood to originate with the band structure of n-type TiO_2. Serpone at al. has shown that the band-gap energy for both rutile and anatase TiO_2 has little particle-size dependence in the range $10Å < R_{part} < 134Å$, but are constants of about 3.0eV for rutile and 3.2eV for anatase[18]. The electron-hole pair created by absorption of UV radiation will catalyze the decomposition of organic pollutants as shown in Figure 2-5. The electron and hole can either recombine or they will diffuse to the surface and take part in a chemical process. The following reactions are possible when a semiconductor particle is in an aqueous environment with an organic pollutant RH_2 (Equation 2-1)

$$\begin{array}{l}
h^+ + H_2O \rightarrow OH_{ad} + H^+ \cdot aq \\
h^+ + RH_2 \rightarrow RH_{ad} + H^+ \cdot aq \\
OH_{ad} + RH_2 \rightarrow RH_{ad} + H_2O \\
RH + h^+ + H_2O \rightarrow RHOH + H^+ \cdot aq \\
RH + H_2O - e^- \rightarrow RHOH + H^+ \cdot aq \\
e^- + O_2 \rightarrow O_2^- \cdot aq \\
e^- + O_2^- + H_2O \rightarrow H_2O^- \cdot aq + OH^- \cdot aq \\
h^+ + e^- \rightarrow heat \\
h^+ + O_2 \rightarrow O_2 \\
e^- + O_{ad} \rightarrow OH^- \cdot aq
\end{array} \qquad \textbf{(2-1)}$$

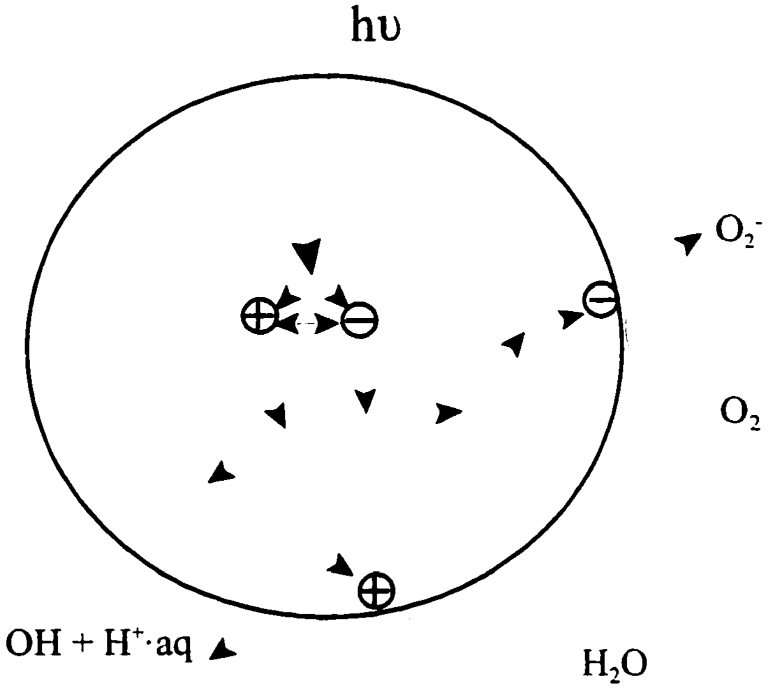

Figure 2-5 An illustration of light induced charge separation in a TiO_2 nanocrystallite embedded in an electrolyte.

Heinz Gerischer has shown that the quantum yield of this system is limited by the rate at which electrons can be transferred to the electrolyte[19], and this is a function of the particle size as well as the presence of shallow surface states on the particles which can trap electrons. All of the properties of the aerogel can be tied to the nanocrystallite size, including the optical properties[20], dielectric constant[21], mechanism of diffusion[22] and others.

Titanium dioxide aerogel has been used to photocatalytically decompose oil, phenol, salicylic acid and a variety of other organic compounds. Salicylic acid is used as the standard "pollutant" to gauge the photocatalytic ability of the aerogel, which also allows comparison with earlier results. Earlier results have shown that the surface area plays a significant part in overall quantum efficiency, with increasing surface area having increased quantum efficiency[23]

TiO_2 Nanocrystalline Solar Cells

Besides photocatalysis, the electron-hole pair may be harvested to yield electricity, the Grätzel cell. The Grätzel cell, named after it's creator, Michael Grätzel, consists of a thin film of nanocrystalline porous TiO_2 that are sensitized by the addition of a Ru-containing metal-organic dye (Figure 2-6). The sensitized TiO_2 is part of an electrochemical cell which includes an electrolyte with I_2 and I^- in surplus as the primary active ingredients. In addition there are other ingredients, in particular the positive ion from the salt which is the source of I^- ions. The dye is sensitive to visible light, and generates an electron-hole

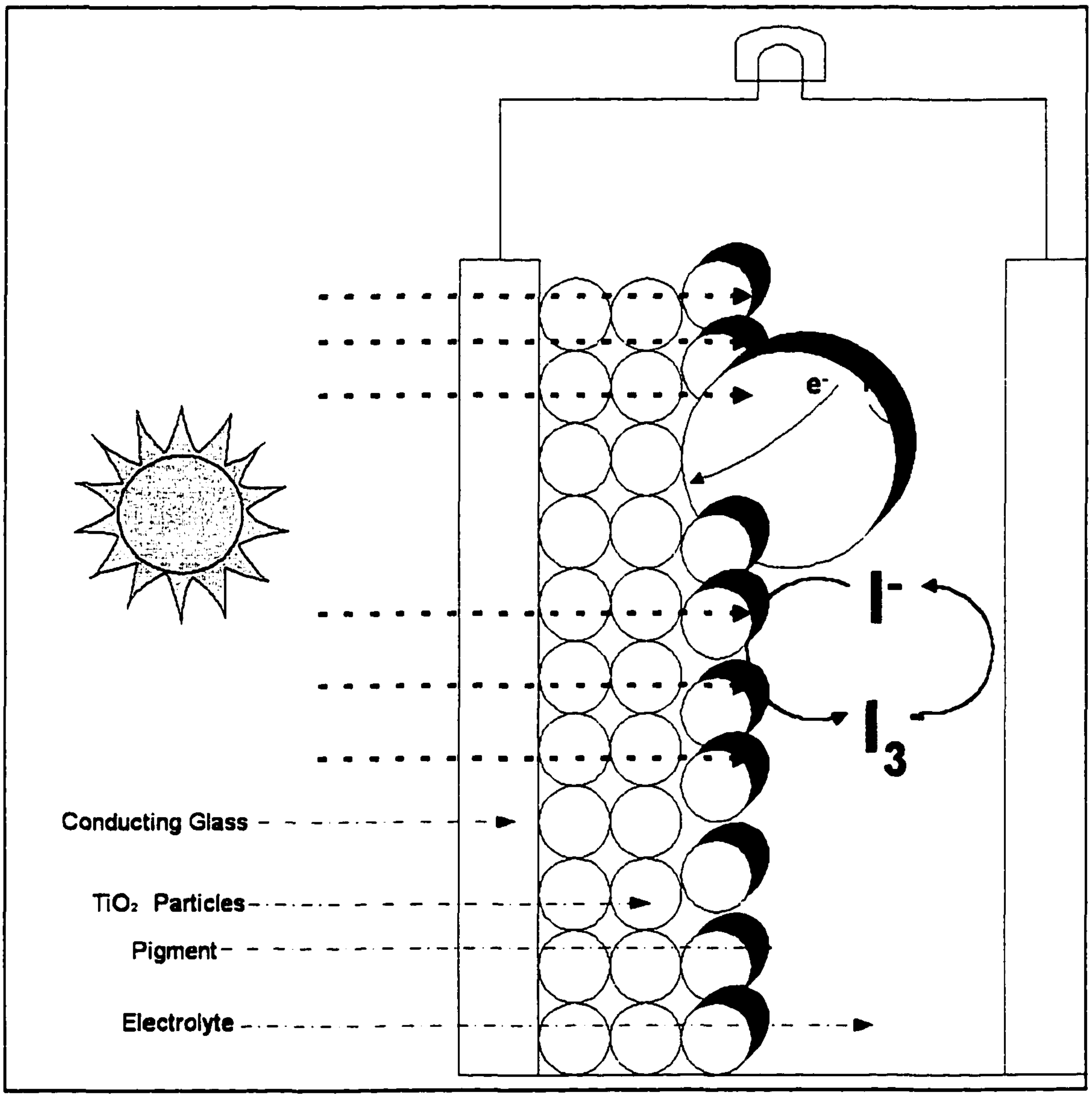

Figure 2-6 Schematic of the Grätzel cell, which utilizes TiO_2 particles and a light absorbing dye to achieve a high efficiency solar electrochemical cell.

pair. In a very short time, the I^- reduces the hole, subsequently forming I_2, which can then complex to form I_3^-. The electron is directly injected into the TiO_2 substrate where it can be carried away. In principle, the electron-hole recombination can always occur, but in this particular situation, the probability of recombination is drastically reduced, because both the electron and the complex it would reduce are negatively charged. This results in a very low recombination rate, and so an efficient electrochemical photovoltaic cell. The Grätzel cell is actively being researched in laboratories around the world as a possible source of inexpensive and renewable energy.

TiO_2 Aerogels

A small globule of green Jell-O™ sits in the sun. After a few hours it has nearly disappeared, leaving behind only the faintest trace of NutraSweet™ and dry gelatin. Nearly all gelatinous substances will shrink upon drying to a fraction of their original volume. Incredibly these dried gels can have as much as 50% empty space. The gelatin forms what is known as a spanning cluster[24], which fills the container in which it is being mixed. The gelatinous material, like a sponge, is riddled with pores. The sponge pores are filled with a fluid, known as the mother liquor, and give rise to the easily pliable structure we call a gelatin.

In 1931, S. S. Kistler at Stanford University invented the technique of "super-critical point drying" to dry a gelatin so that it could have as much as 98% air [25]. He called these materials aerogels. Normal drying in air causes the gel to collapse under the pull of liquid evaporating in the pores. Kistler dried his gels in an autoclave by first pressurizing then heating them. The density of ethanol liquid and vapor are identical above the critical point, which means that the liquid/vapor can be removed without collapsing the gel. His first materials were nearly transparent slabs of silica, and for this reason they were given the nickname "solid smoke"(Figure 2-7[26]). He went on to create aerogels from starting materials of alumina, tungsten, iron and tin oxides, nickel tartrate, cellulose, gelatin, egg white and rubber. He believed that there was literally no end to the possible materials that could be incorporated into an aerogel structure. In fact his prediction was quite accurate and aerogels have been made which incorporate a wide range of materials[27].

Thirty years passed without much change in the way aerogels were made, which was a lengthy and arduous process, and could be dangerous. The gel material was heated in a pressurized chamber, an autoclave, above the critical point of ethanol. At the critical point, liquid ethanol and vapor ethanol are identical, so there is no boundary between them and no surface tension. Kistler actually destroyed one of his laboratories, in the process of making a large monolithic aerogel, when an autoclave exploded. Then, in the early 1960's, Stanislas J. Teichner and his graduate student at the University of Lyons tried to repeat the experiments of Kistler. They succeeded in producing two aerogel samples after weeks of effort. The poor graduate student whose thesis was contingent on the ability to produce many of these aerogel samples had a nervous breakdown at the thought of how many years it would take to complete the research. Luckily for the graduate student, shortly after his recovery, a new method for producing aerogels was

Figure 2-7 A silicon dioxide aerogel is a translucent but hazy "solid smoke".

introduced that took only a day to complete[28]. This method involves cooling the gel sample and washing the ethanol out with liquid carbon dioxide, then removing the CO_2 by critical point drying. The CO_2 critical point drying method is the most commonly used technique for making aerogels. Kistler was able to make aerogels out of a number of materials, but a notable exception is the material of the current work, titanium dioxide.

Synthesis of TiO_2 Aerogels

Aerogels are made by drying a "wet" gel in a process called super-critical drying. The gels are a matrix of cross-linked titanium dioxide that is formed by the polymerization of a titanium isopropoxide precursor. The precursor is hydrolyzed in a solvent of ethanol by slowly adding drops of water. In addition, a small quantity of nitric acid is added to the solution. It is thought that the nitric acid acts as a control on the rate of the hydrolysis reaction by binding free water and keeping it from the hydrolysis reaction. The gel can form for a variety of chemical compositions and the resulting aerogels have remarkably different properties. For example by raising the amount of water present in the gel we can increase the density and decrease porosity of the aerogel, which results in a stronger overall structure. By decreasing the pH or increasing the ratio of nitric acid in the sol composition we can adjust the hydrolysis rate of the gel which also results in a stronger, more compact structure. In contrast by lowering the nitric acid content or the water content we can create less dense materials with much higher surface areas.

Aerogels are perhaps the simplest structure in which the fundamental building blocks are nanocrystallites so that their properties are associated with the properties of the nanocrystallites yet the nanocrystallites are interconnected to form a well defined pore structure. The nanocrystallites are about 5nm in diameter and are close-packed to form mesospheres about 50nm in diameter. The mesospheres are loosely packed to form the aerogel material itself (Figure 2-8). This picture is derived from a myriad of evidence regarding the aerogel morphology.

Characterization of TiO_2 Aerogels

The average crystallite size is determined from the powder x-ray diffraction spectrum. The X-ray spectrum identifies the particular phase of titanium dioxide in the aerogel as the series of peaks (location and relative size) is unique to each crystalline phase. The Full Width at Half Maximum (FWHM) of the largest peak can be used to estimate the crystallite size, through the Scherrer formula (Equation 2-2).

$$L = \frac{\kappa\lambda}{\Gamma\cos(\theta)} \qquad \textbf{(2-2)}$$

The Scherrer equation is a manifestation of the uncertainty principle in that the diffraction of x-rays must occur in a localized region (L) which is the size of the crystallites, which means that the x-ray momentum (and related wavelength) must be $\Delta q \sim 2\pi/L$. In the equation L is the average dimension of the crystallite, κ is a shape factor constant (assumed to be 1 for spherical particles), Γ is the FWHM(2θ), and θ is the angle of incidence of the x-ray beam. In Figure 2-9, the unique spectra of anatase TiO_2 can be seen. The crystallite is estimated to be 58nm from the FWHM.

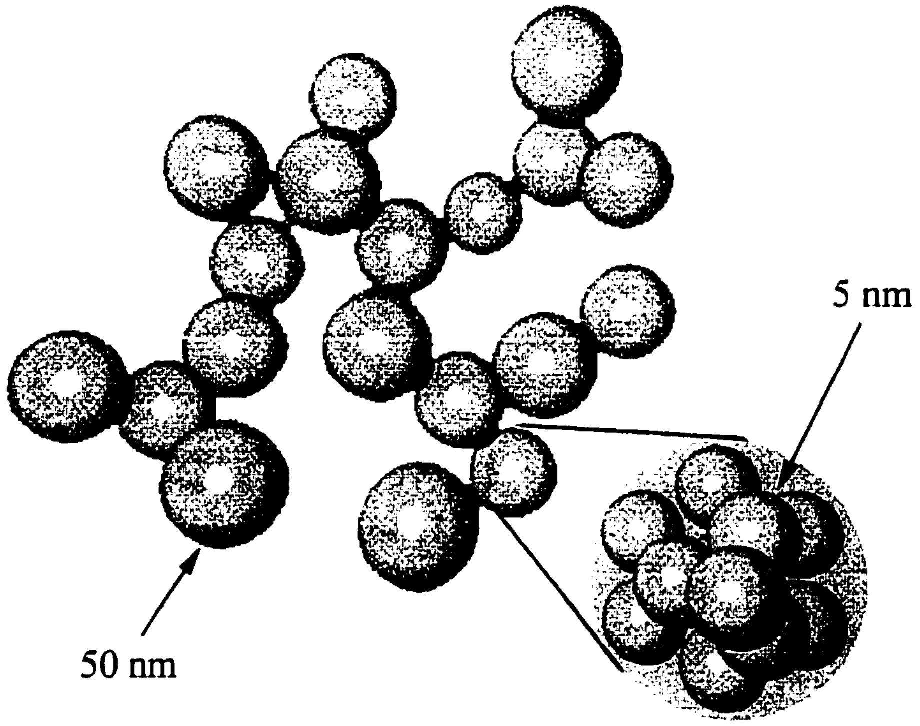

Figure 2-8 Schematic of aerogel structure. The Mesospheres are about 50nm in diameter and consist of close-packed nano-crystallites about 5nm in diameter

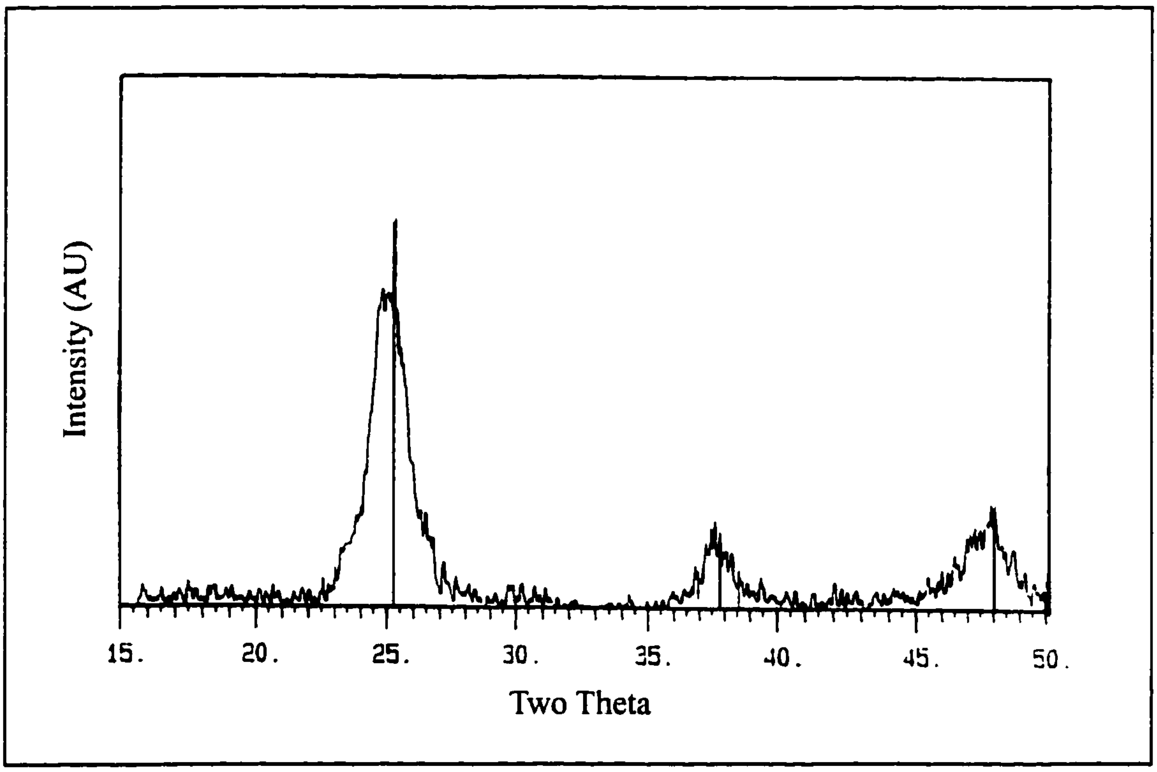

Figure 2-9 The X-ray diffraction spectra for an untreated aerogel shows peaks which are representative of the anatase spectra.

Zhu Zhu et al. used Small Angle Neutron Scattering to study the morphology of the aerogels, and found evidence of nanoparticles about 5nm in diameter[29]. Although it was impossible at the time of their measurement to detect large objects 50nm in diameter, there was some indication that the neutron scattering showed the beginning of another peak in the 50nm region.

Another invaluable technique for measuring the aerogel morphology is through Brunauer-Emmett-Teller (BET) N_2 absorption. The BET measurement is performed at liquid nitrogen temperature, and involves measuring the amount of N_2 gas which condenses on the surface of the aerogel with increasing pressure. As the pressure increases, more and more of the pore volume is reached by the N_2, hence it is also a measurement of the aerogel porosity. A typical BET measurement for the aerogel is shown in Figure 2-10. The N_2 absorption isotherm can be used to derive the pore size distribution as well. In reality, the nanocrystallites are not mono-disperse but are a distribution of sizes. Zhu and others have examined TiO_2 aerogels with a Transmission Electron Microscope, which can visualize roughly 5nm crystallites. Taken together, the evidence shows a bimodal distribution in the scales of the aerogel system, the 5nm nanocrystallites and the 50nm mesospheres (Figure 2-11)[30]

The aerogel structure is well-connected as Dagan et al showed by measuring the skeletal density with helium pyknometry. They measured a skeletal density of 2.7 - 3.9g/cm^3 which is in good agreement with the single crystal density of 3.79g/cm^3 for anatase TiO_2[23]

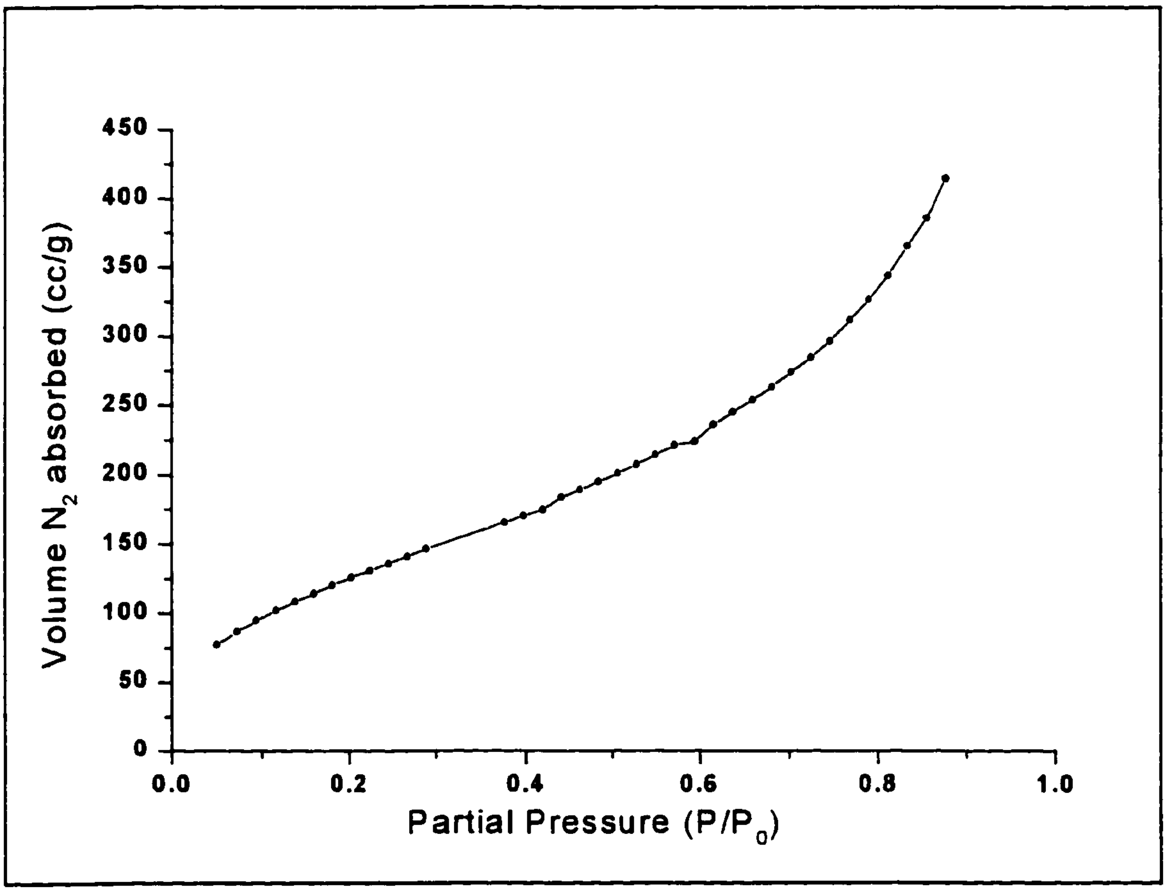

Figure 2-10 Standard BET N_2 absorption curve for a titanium dioxide aerogel.

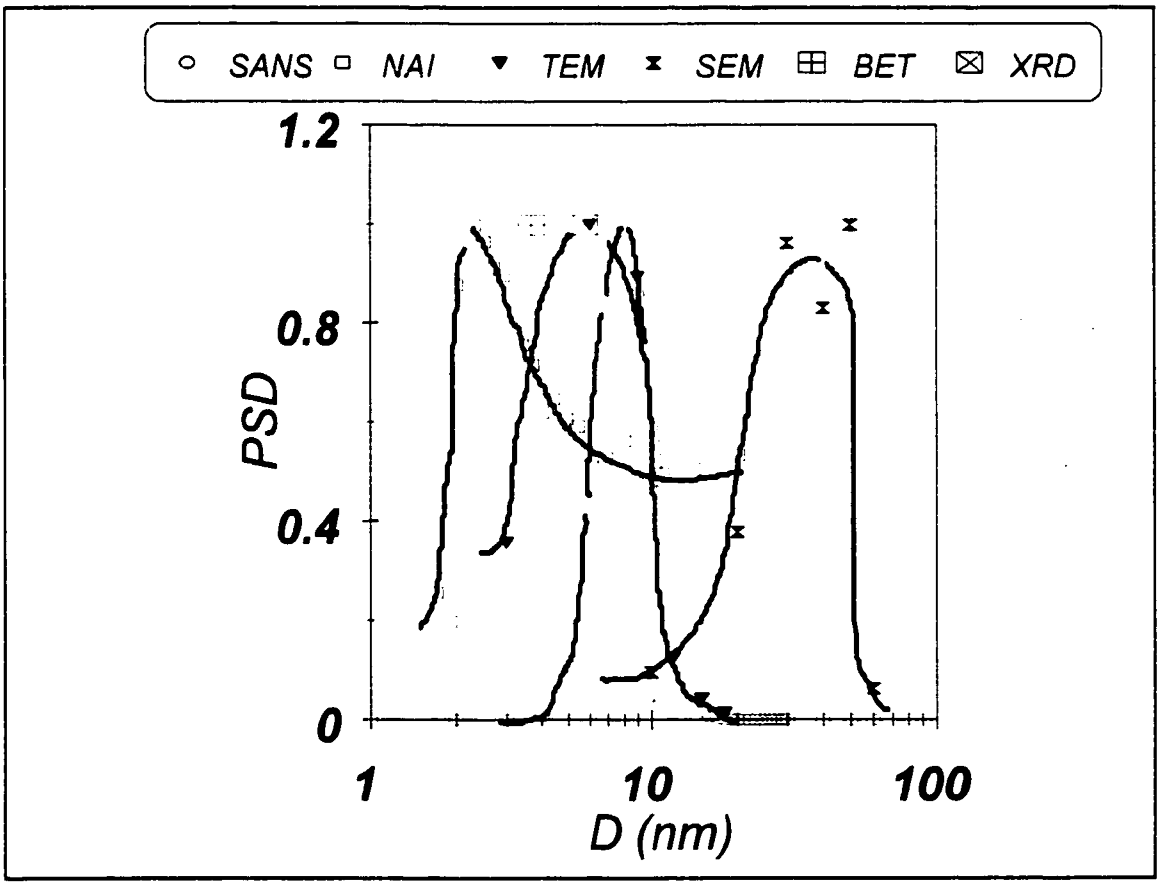

Figure 2-11 Through various techniques, the structure of the aerogel is determined to have two scales. The 5nm crystallites are organized into mesospheres of about 50nm in size.

Monitoring gel formation

The process of making an aerogel is still rather lengthy and when aging of the gel is taken into account, the process can take from several weeks to several months. In order to fully understand how various modifications in the recipe and subsequent treatment affect aerogel morphology, it would be helpful if there were a single measurement technique that could measure the evolution of the solution through the formation of the aerogel. Raman scattering (RS) and Extended X-ray Absorption Fine Structure (EXAFS) were both used to monitor the evolution of the sol-gel and Raman spectroscopy was also used to monitor the evolution of the aerogel after drying. Each of the techniques probes the sol structure in a non-destructive and non-invasive way. Both techniques have been used with great success for the monitoring of structural evolution in both liquids and solids. The Raman scattering technique utilizes laser light for excitation of vibration modes in the solution/solid. In a solution these vibrational modes are molecular vibrations (only nearest neighbor interaction), and in crystalline solids they are collective interactions of the entire crystal, and are called phonons.

For the sol-gel, there is some difficulty in measuring the changes in the structure of the solution. This is primarily because the strongest part of the spectrum actually comes from the ethanol solvent. In order to determine the spectra of the underlying condensate, it was necessary to subtract a very large background signal. Subtraction of two large signals is inherently a difficult technique for determining with any precision what is going on in the sol. It is much easier to monitor changes in the spectra, and from these "differences" to determine what is happening in the sol.

Objective

The goal of the present work is to control the aerogel morphology (surface area, degree and phase of crystallinity, porosity) by controlling the various synthetic parameters (reactant ratios, washing, annealing) to optimize the aerogel's photcatalytic ability. The aerogel can be modified at several stages in it's synthesis and a non-destructive, non-invasive technique for monitoring the evolution of the sol-gel then aerogel is critical to understand the aerogel morphology. Raman spectroscopy and Extended X-ray Absorption Fine Structure are both used to monitor the evolution of sol-gel and aerogel. The various morphological characteristics have competitive effects on the photocatalytic ability, indicating the presence of an "optimal" morphology. In addition this work might lead to creating a novel class of self-assembling titanium dioxide aerogels which optimize themselves based on the environmental conditions in which they will be used.

Chapter 3 - Synthesis of TiO_2 Aerogels

Chemical Synthesis

All aerogels begin as gelatinous materials(gels) which are created by sol-gel chemistry. In order to make an aerogel from titanium dioxide, it is necessary to begin with a material which contains titanium. This starting material, or precursor, is titanium isopropoxide (TIP) $Ti(OC_3H_7)_4$. The TIP is mixed in a solvent of ethanol (EtOH) and then a mixture of EtOH, water and nitric acid is slowly added to the solvent, making a solution (sol).

At this stage the precursor material begins to polymerize by hydrolysis or alcolysis reactions. The hydrolysis reaction involves the removal of an alcoxy group from the TIP which is replaced by an OH group (Eq. 3-1). Alcolysis is an alternative process whereby the alcoxy group is replaced with another alcoxy group from the solvent (Eq 3-2)

$$Ti(O\mathrm{Pr}^i)_4 + H_2O \Leftrightarrow Ti(O\mathrm{Pr}^i)_3 - OH + \mathrm{Pr}' OH \qquad \textbf{(3-1)}$$

$$Ti(O\mathrm{Pr}^i)_4 + EtOH \Leftrightarrow Ti(O\mathrm{Pr}')_3 - OEt + \mathrm{Pr}^i OH \qquad \textbf{(3-2)}$$

Once the hydrolysis or alcolysis has partially taken place on the TIP, the cross-linking and condensation begins(Eq. 3-3, 3-4).

$$Ti(O\mathrm{Pr}^i)_3 - OEt + Ti(O\mathrm{Pr}^i)_3 - OH \Leftrightarrow Ti(O\mathrm{Pr}^i)_3 - O - Ti(O\mathrm{Pr}^i)_3 + EtOH \qquad \textbf{(3-3)}$$

$$Ti(O\mathrm{Pr}^i)_3 - OH + Ti(O\mathrm{Pr}^i)_3 - OH \Leftrightarrow Ti(O\mathrm{Pr}^i)_3 - O - Ti(O\mathrm{Pr}^i)_3 + H_2O \quad \textbf{(3-4)}$$

The titanium atom has a valency of four which means that it may bond with up to four neighboring atoms/molecules. In order to create a stable structure it is necessary to have a good fraction of the branches with a functionality greater than 2. The functionality must be between 2 and 4.

The acid in the recipe for the sol-gel has the effect of catalyzing the reverse reaction. The lower the pH, it becomes easier to reverse the condensation reaction. Jeffrey Brinker et al. have shown that a side effect of the lower pH is to increase the density of the condensed particles in the sol-gel[31]. If the pH is too low, the gel will never form. The ratio of initial reactants is given as a molar ratio to the amount of TIP in the recipe (Eg. 1:20:3.5:0.08), where for 1 mole TIP, there are 20 moles of ethanol, 3.5 moles of water and 0.08 mole of HNO_3. The composition of the initial sol can be adjusted and will affect the eventual aerogel morphology in different ways.

If we begin with a given reactant ratio, $1{:}R_{H2O}{:}R_{EtOH}{:}R_{HNO3}$, and also the volume of TIP, V_{TIP}, we can compute all of the other volumes for the solution. The number of moles of TIP is easily determined from V_{TIP}, and is N_{TIP}., equation 3-5

$$\begin{aligned} V_{TIP} &= V_{TIP} \\ N_{TIP} &= \frac{V_{TIP} * \rho_{TIP}}{M_{TIP}} \\ V_{EtOH} &= \frac{R_{EtOH} * N_{TIP} * M_{EtOH}}{\rho_{EtOH}} \\ V_{HNO3}(70\%) &= \frac{R_{HNO3} * N_{TIP} * M_{HNO3}}{0.7 * \rho_{HNO3}} \\ V_{H2O} &= \frac{R_{H2O} * N_{TIP} * M_{H2O}}{\rho_{H2O}} - 0.3 * V_{HNO3} \end{aligned} \tag{3-5}$$

Material	**Density (g/cm^2)**	**Molar Mass (g)**
Titanium Isopropoxide (TIP)	0.955	284.26
Ethanol (EtOH)	0.789	46.07
Water (H_2O) (23°C)	0.997	18.016
Nitric Acid (70%) HNO_3	1.4134	63.02

Table 3-1 Densities and molar masses for the reactants used in making TiO_2 aerogels.

For example a reactant ratio of 1:3.5:20:0.08 and a volume of 5 mL. In this case, the volumes of the other reactants are shown in Table 3-2. Using two small flasks, the ethanol is divided equally between the flasks. To one of the flasks, all of the water and nitric acid are added. Placing a magnetic stir-bar in the solution, the flask is placed on a stir plate for a few minutes to mix thoroughly.

Reagent	Titanium Isopropoxide	Ethanol	Water	Nitric Acid (70%)
Volume (mL)	5.00	19.62	0.974	0.086

Table 3-2 Volume of reactants for a ratio of 1:20:3.5:0.08.

Then the other flask is placed on the stir plate with a magnetic stir-bar, mixing the flask as the TIP is added to it. Drop by drop, the solution of ethanol, water and nitric acid is added to the solution of ethanol and TIP. At some point during this process, a white condensate may appear. The white condensate is possibly a powder of monomeric TiO_2 which forms from fast hydrolysis, but continuing to add the ethanol, water and nitric acid solution will cause the solution to clarify. In most cases, the success of the recipe is indicated by yielding a translucent, nearly transparent or a transparent solution. The resulting solution is placed in an air-tight container where the solution will eventually stiffen and gel.

The formation of the gel is essentially a two stage process. There is evidence to support the idea that nanocrystallites (~5nm) of TiO_2 form very quickly in the sol-gel process[32], then aggregate very quickly to form close-packed mesospheres(~50nm). The mesospheres themselves aggregate relatively slowly, in a loose network to form the gel itself. When the container is completely filled with clusters, either cross-linked or otherwise, the material is said to have gelled.

Gelation time is the first indicator that the gel structure is being affected. If we are affecting the mechanism for condensation and subsequent gelation, then we should expect the gelation time to be affected. Gels are characterized as weak or strong depending on their ability to deform and return to their original shape. There are some clear correlations between gelation time and the strength of the gel. The standard gel in its closed container exhibits a resonance when struck lightly. Think of the words to the jingle for Jell-O™ brand gelatin; "Watch it wiggle, see it jiggle". The gelatin will "wiggle and jiggle" if it is strong but will not support this deformation oscillation if it is weak. The gelation time can be dramatically altered by changes in the reactant ratios. For example increasing the water ratio will cause gelation to occur faster. Increasing the water ratio will also make the gel cloudier, or less homogeneous. If the water ratio is very high, then the condensation process occurs very quickly, effectively trapping un-reacted precursor in the gel. This un-reacted precursor causes problems later as it creates a lot of stress on the gel structure during washing, or even on the aerogel structure after super-critical drying. The un-reacted precursor will react strongly with water in an aqueous environment, causing the aerogel to fragment into a powder.

Increasing the Ethanol ratio will cause gelation time to shorten, and the resultant gels tend to be weaker. They do not support any oscillation and for very high ethanol ratios will even flow if the container is held on its edge. Increasing the acid ratio will cause the gelation time to lengthen, however for very high acid ratios the gel will never form. The acid enables the dissolution of condensed material, and without some acid, the material formed will always be amorphous. It has been shown that the acid ratio (or pH) can change the nanocrystallite size[33] For the case of very high acid ratio and the gel does form, the gel structure is very weak. This means that there is very little cross-linking between clusters and subsequently will not be held together as a whole very well.

The gel is allowed to sit in a dark environment for several weeks, and even months. In this time, most gels will undergo a small shrinkage, noticeably pulling away from the walls of the container. In addition, ethanol will appear in the container which is not incorporated in the gel structure. As the gel ages, un-reacted material slowly incorporates itself in the gel structure. Images of the aerogel material show that the mesospheres are joined by neck structures. These neck structures are a product of the aging process[32]. In addition there is undoubtably some consolidation and networking taking place which serves to strengthen the gel. The neck material and other condensation serves to expel ethanol from the pores, which explains the existence of free ethanol in the air-tight containers[34]. This process of expelling ethanol from the gel is called syneresis, and it is always accompanied by the shrinkage of the gel. Evidence of syneresis is also a good indicator of cross-linking in the gel structure.

At this stage, the gels are washed. The wash consists of ethanol with a varying concentration of water. The gel can be washed with pure ethanol a number of times by bathing the gel in pure ethanol then draining off the ethanol and repeating. The material that is drained off consists of fine particles which are not attached to the gel. If washing is not done, then a fine powder of TiO_2 will be present when the gel is dried in the critical point dryer. By washing with ethanol laced with water, any un-reacted precursor will be hydrolyzed and this should make the gel more stable, as well as provide better cross-linking. If the gel is introduced directly to pure water, a very energetic reaction ensues, which is attributable to the presence of un-reacted precursor, TIP. The reaction of TIP with water is explosive and as a result the gel will crack and crumble apart in this situation. By gradually increasing the amount of water in an ethanol wash, the rate of hydrolysis can be controlled and it is possible to eventually wash the gels in water without destroying them. Gels which have been washed in water become cloudy, perhaps an indicator of larger crystallites forming in the gel.

Critical Point Drying

To form the aerogel it is necessary to remove the ethanol from the pores of the gel. If the gel is allowed to dry in air at room temperature, the ethanol will evaporate, and in the process, the capillary force of the shrinking ethanol volume will pull on the gel pore walls, collapsing them. A gel dried in this way is called a xerogel and is typically a slightly porous, but dense cousin of the aerogel. The ethanol can be removed without collapsing the gel by utilizing the super-critical drying method invented by Kistler. Examining the phase diagram for ethanol, it is evident that at the critical point, T = 243C and P = 926psi[35], ethanol gas and liquid are essentially the same. This means that there will be no boundary layer between gas and liquid, e.g. no surface tension. Above the critical point it is possible to slowly remove the ethanol gas/liquid without pulling on the pore walls and without collapsing the structure. The modification to this technique created by Teichner and his student was to make the process even easier to achieve, by first replacing the ethanol in the pores with liquid carbon dioxide. By pressurizing an autoclave chamber to at least 800psi and cooling it to near 0C, carbon dioxide will remain in a liquid form and can slowly wash out ethanol in the pores of the gel. When all of the ethanol has been washed out of the pores, the chamber is heated and pressurized to the super-critical region of carbon dioxide, which occurs at the substantially lower values of T = 31.3C and P = 1072psi[35]. This procedure is the most commonly used one for the drying of aerogels today.

The gels were dried using a Tousimis Auto SAMDRI-814 critical-point dryer. The path that the critical point dryer takes in P-V space is shown in Figure 3-1. This was the technique invented by Stanislas J. Teichner and his graduate student in the 1960s.

BET Surface Area and X-ray Characterization

Once the aerogel has been made, it is characterized by a two important techniques: BET Nitrogen absorption and X-ray diffraction. The BET Nitrogen absorption measurement will determine the porosity, surface area, and the pore size distribution. The X-ray diffraction peaks will indicate the type of crystallite present as well as the mean crystallite size. Powder x-ray diffraction spectra are measured and the peaks are fit to Gaussian functions. The peak location and FWHM are then used in the Scherrer formula (Eq. 2-2).

The x-ray spectra for an aerogel sample before heating can be seen in Figure 3-2, with

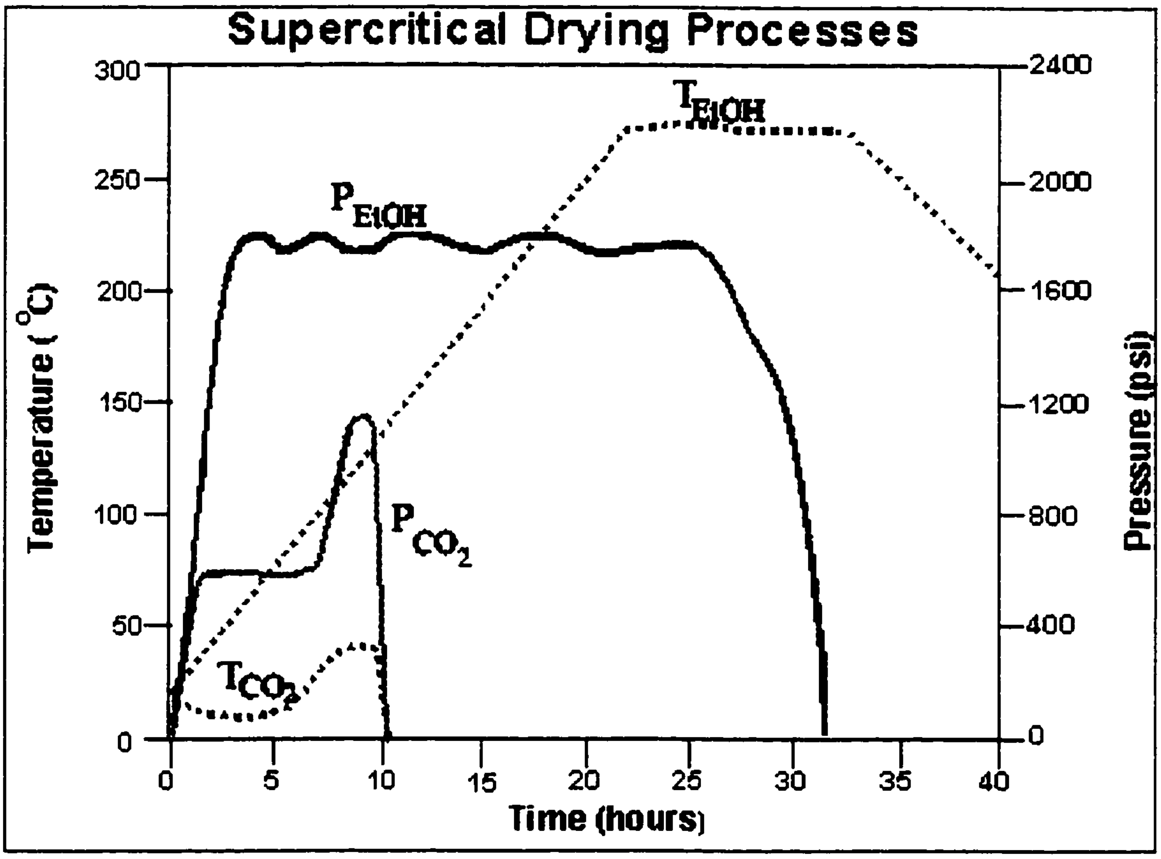

Figure 3-1 The path the critical point dryer takes in drying TiO_2 gel.

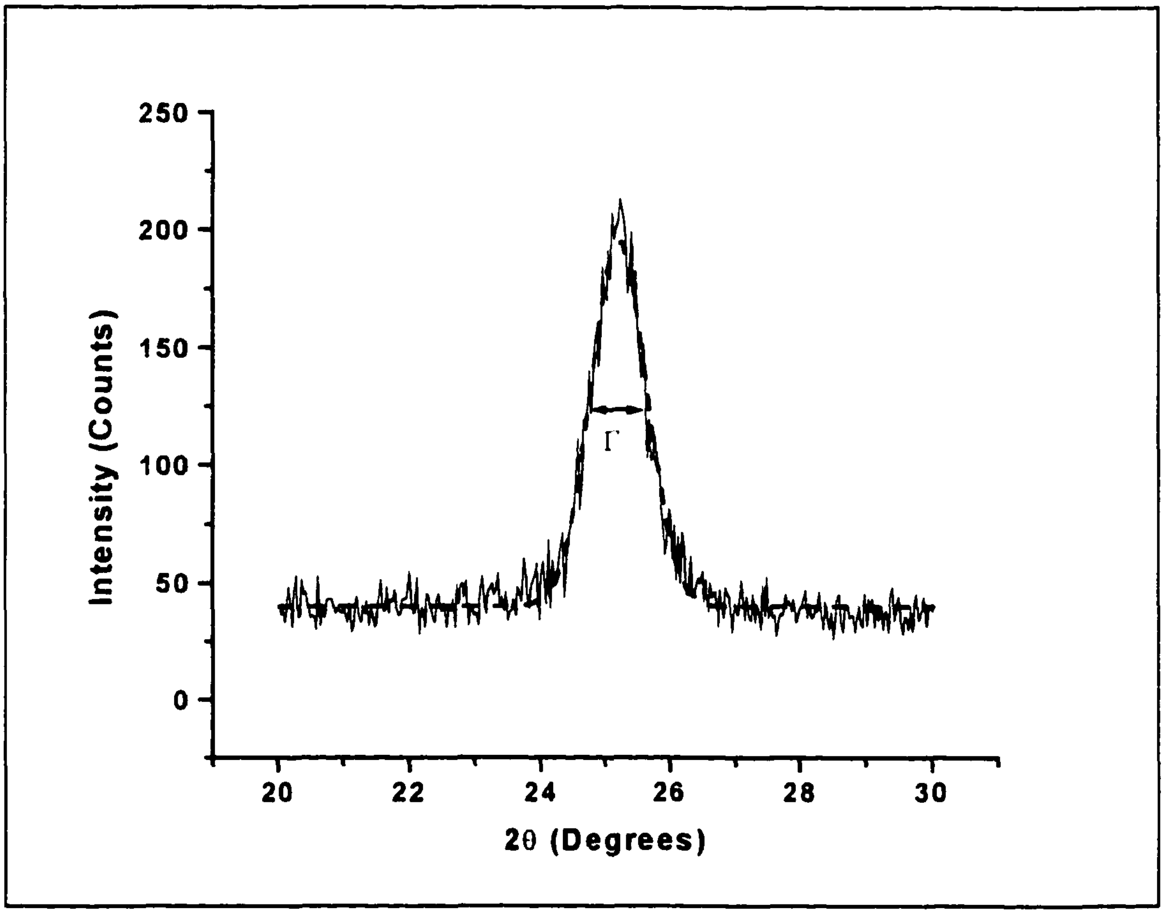

Figure 3-2 The x-ray spectrum for unheated TiO_2 aerogel has a primary peak at 25.2 degrees which corresponds to anatase. The FWHM is determined by a Gaussian fit(dashed line) of the peak. In this case the crystallite size is about 6.5nm.

the primary anatase peak at about 25.2°. The crystallite size is about 6.5nm. As the aerogel is heated the crystallites begin to grow. Heating at 500C produces crystallites of about 8.6nm (Figure 3-3). When they are heated above 700C the anatase begins to change its phase to rutile (Figure 3-4) and the x-ray spectra shows both the anatase and rutile peaks. The rutile peak is much clearer and from this peak the crystallite size is 24.9nm. All TiO_2 aerogels are made up of anatase when they are first made. A small number of aerogel samples, their surface area, crystallite size, and calculated surface area are listed in Table 3-3.

Sample	BET Surface Area (m^2/g)	Crystallite Size (nm)	Preparation Variable	Calculated Surface Area (m^2/g)
A	735	1.7	$H_2O:Ti(OPr^i)_4$	464
B	472	2.0	$H_2O:Ti(OPr^i)_4$	395
C	449	2.2	$H_2O:Ti(OPr^i)_4$	359
D	362	4.3	200^{0}C - 2Hrs.	184
E	134	9.7	500^{0}C - 2Hrs.	81
Degussa P25	54	≥20		39

Table 3-3 Several aerogel samples, and Degussa P25, prepared by various preparation

The theoretical surface area can be calculated by assuming that the mass of the aerogel is entirely composed of crystallites with crystal size derived from the x-ray diffraction data. The number of crystallites, multiplied by a single crystallites surface area is the theoretical surface area. In all of the cases, the calculated surface area is smaller than the measured surface area, in some cases, dramatically smaller. This may be explained by

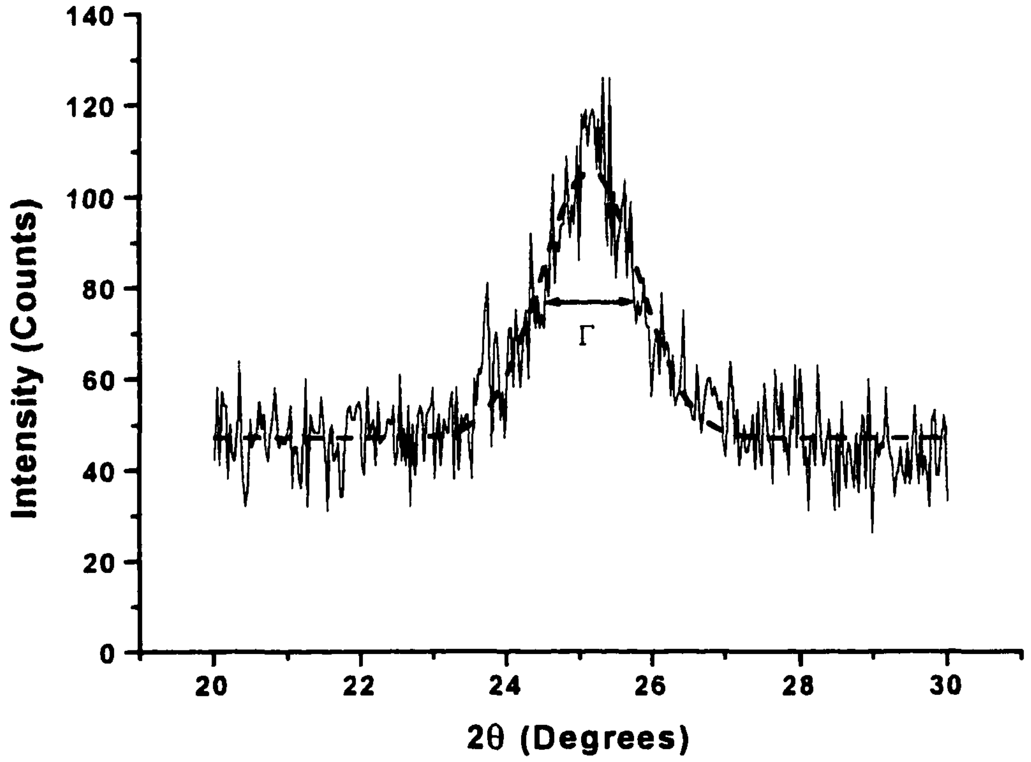

Figure 3-3 The X-ray diffraction spectra for an aerogel heated at 500C for one hour, shows the primary peak of the anatase spectra. The peak is fit with a Gaussian curve to determine the FWHM. Using the Scherrer formula, the crystallite size is found to be about 8.6nm.

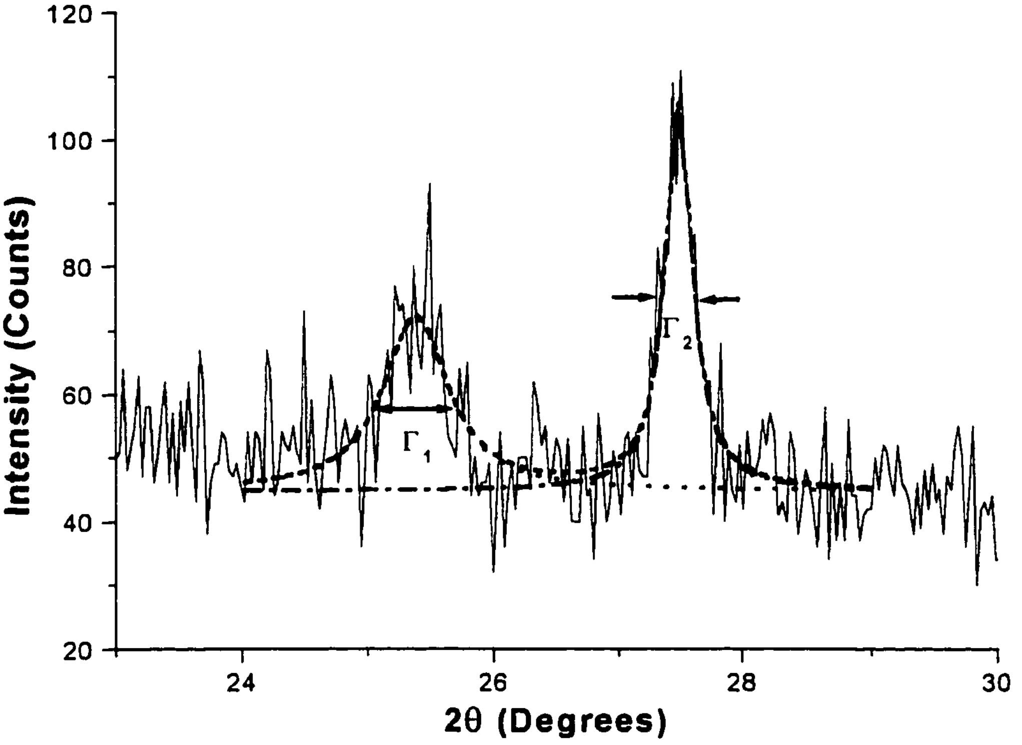

Figure 3-4 The X-ray powder diffraction spectra for an aerogel heated at 700C for a half hour, shows peaks which are a mix of both the anatase(Γ_1 peak) and rutile(Γ_2 peak) spectra.

the fact that x-ray diffraction is directly proportional to the scattering volume, so will be sensitive to the presence of large particles and essentially insensitive to the presence of small particles. The very small particles which are undoubtably present will not affect the x-ray spectra, but will actively participate in the absorption of Nitrogen, meaning the BET surface area measurement will be much larger than would be estimated from the X-ray crystallite size alone.

Aerogel Cleaning

After the aerogel has been made, but before it can be used in photcatalysis, the aerogel is washed to remove residual organic compounds from the synthesis process. Washing is done by placing the aerogel in the photocatalysis vessel and washing repeatedly with de-ionized water. The water is tested for leached organics by UV/Vis absorption. In Figure 3-5, the waste water shows a much smaller absorption than when the aerogel is first made. This organic material is primarily alcohol groups (ethanol or isopropanol) from the synthesis, either physically absorbed into the aerogel pores or chemically bound to the surface. To verify that the alcohol groups are removed by the washing, Thermal Gravimetric Analysis (TGA) and Scanning Differential Calorimetry (DSC) were performed on the aerogels. A TA Instruments SDT2960 performed simultaneous TGA and DSC measurement of aerogel samples in the range 50-900C. Before the sample is washed, the aerogel shows a very large mass loss, 38.3% and 35.7%, when heated in air and nitrogen respectively (Figure 3-6). Although the water evaporation plays a significant part of the mass loss (about 14% from 50C-190C), a larger portion comes

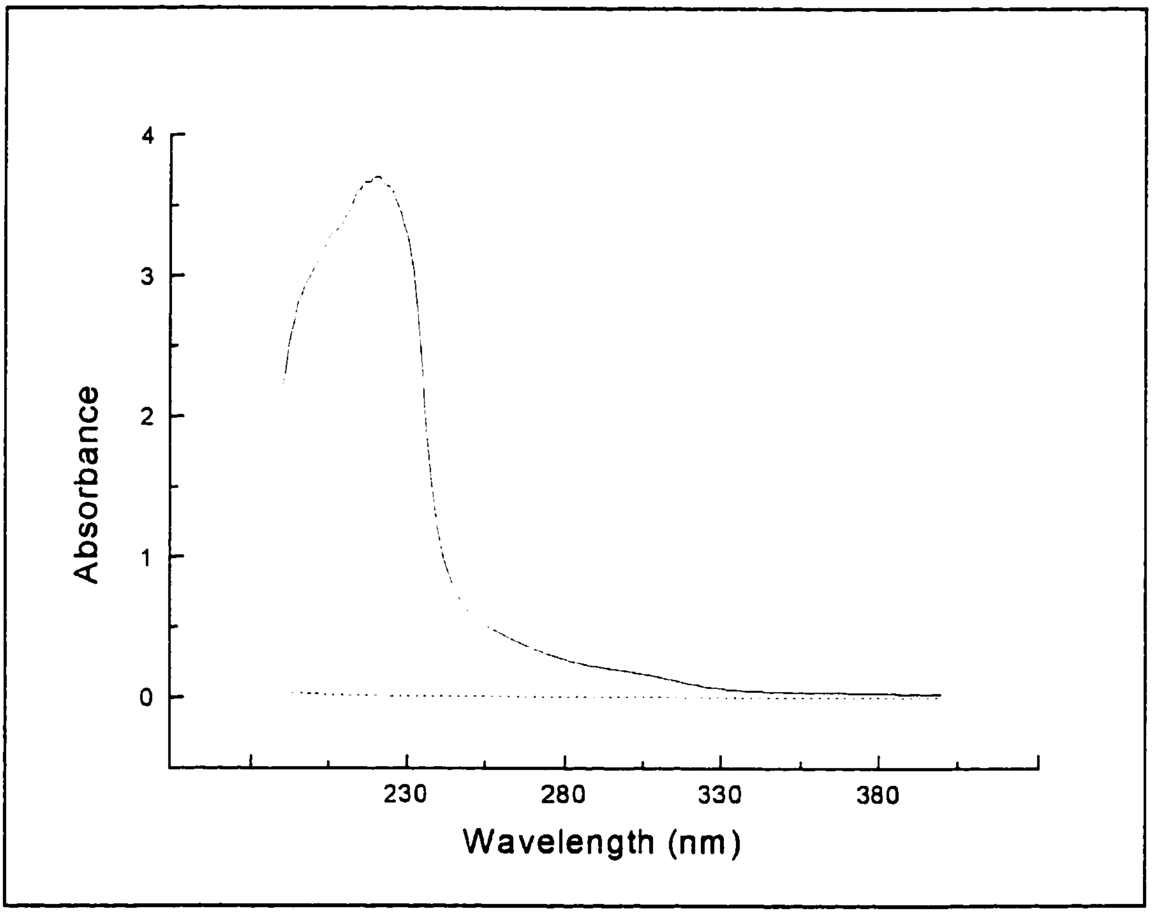

Figure 3-5 The UV absorbance of the aerogel wash water after one wash (solid line) and after several washes (dotted line).

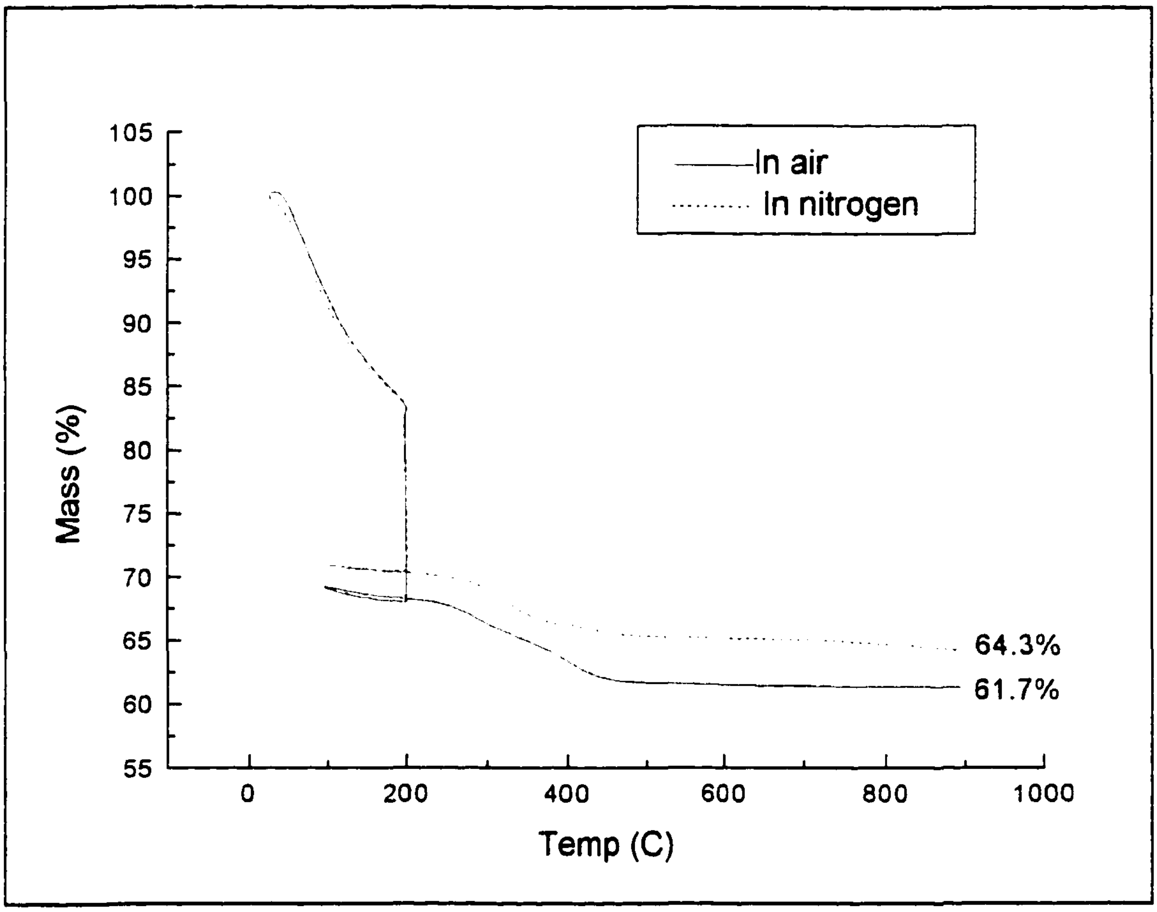

Figure 3-6 TGA of titanium dioxide aerogel in air and in a pure nitrogen atmosphere show a total mass loss of 35.7% and 38.3% respectively.

from the desorption and decomposition/oxidation of residual alcohol (Figure 3-7). After washing the bulk of the mass loss is due to water desorption (Figure 3-8). The mass loss is better understood when examined in conjunction with the SDT data. The SDT are interpreted by noting that a valley is an endothermic process, and a peak is an exothermic process. The SDT signal for the unwashed aerogel in air and nitrogen (Figure 3-9) both show a deep valley around 100C, and a large peak at 200C. When the aerogel is heated in air, there are also prominent peaks at 278C, 395C and 449C. When the same sample is heated in nitrogen, the peak at 278C disappears, there is a slight peak and it is shifted to 381C, and there is a much larger peak at 464C. In any case as the SDT data shows, when the aerogel has been cleaned, the SDT data are much simpler (Figure 3-10). Most of the features have disappeared, leaving only the water evaporation at 100C, a very small peak at 257C, a peak at 428C and a small peak at 709C. Clearly the missing peaks can be associated with the residual alcohol, and show that the aerogel is indeed cleaned by washing.

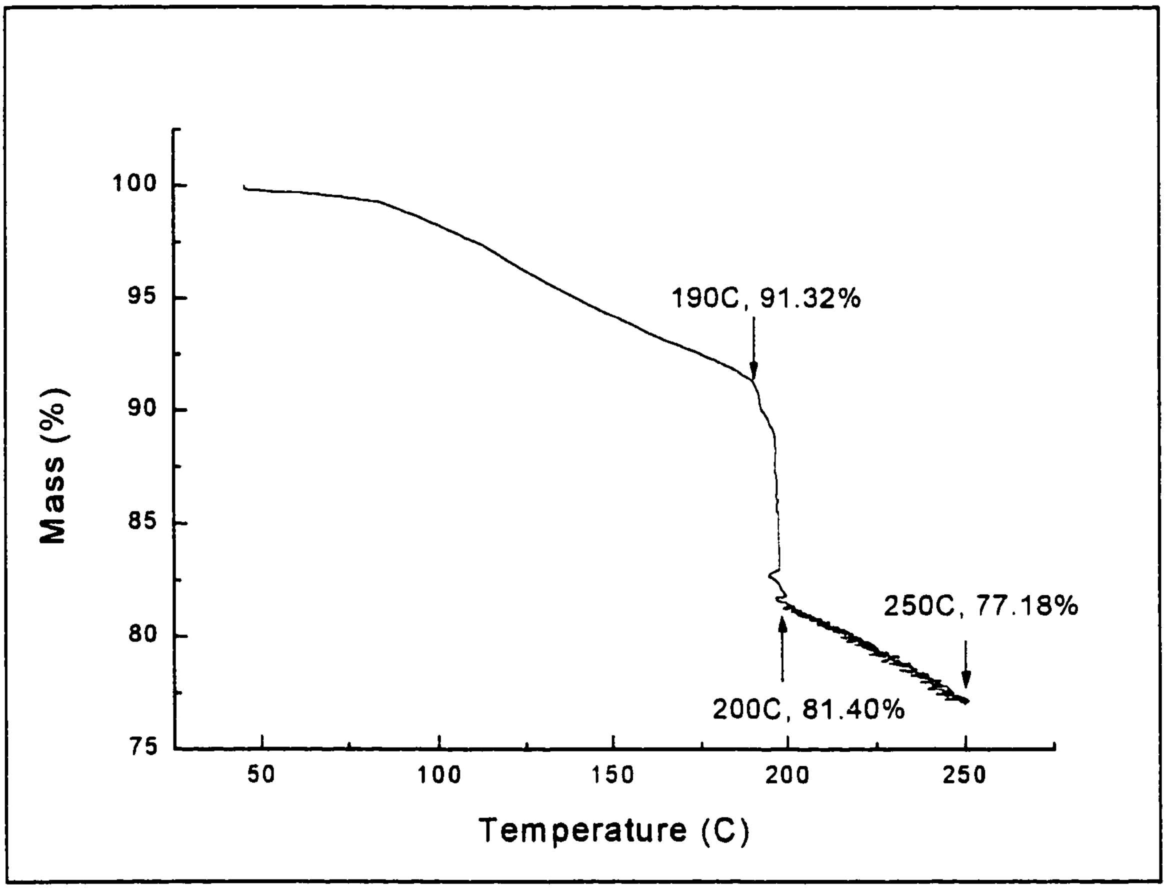

Figure 3-7 A large mass loss occurs in the titanium dioxide aerogel at about 190C when the residual alcohol is desorbed/decomposed.

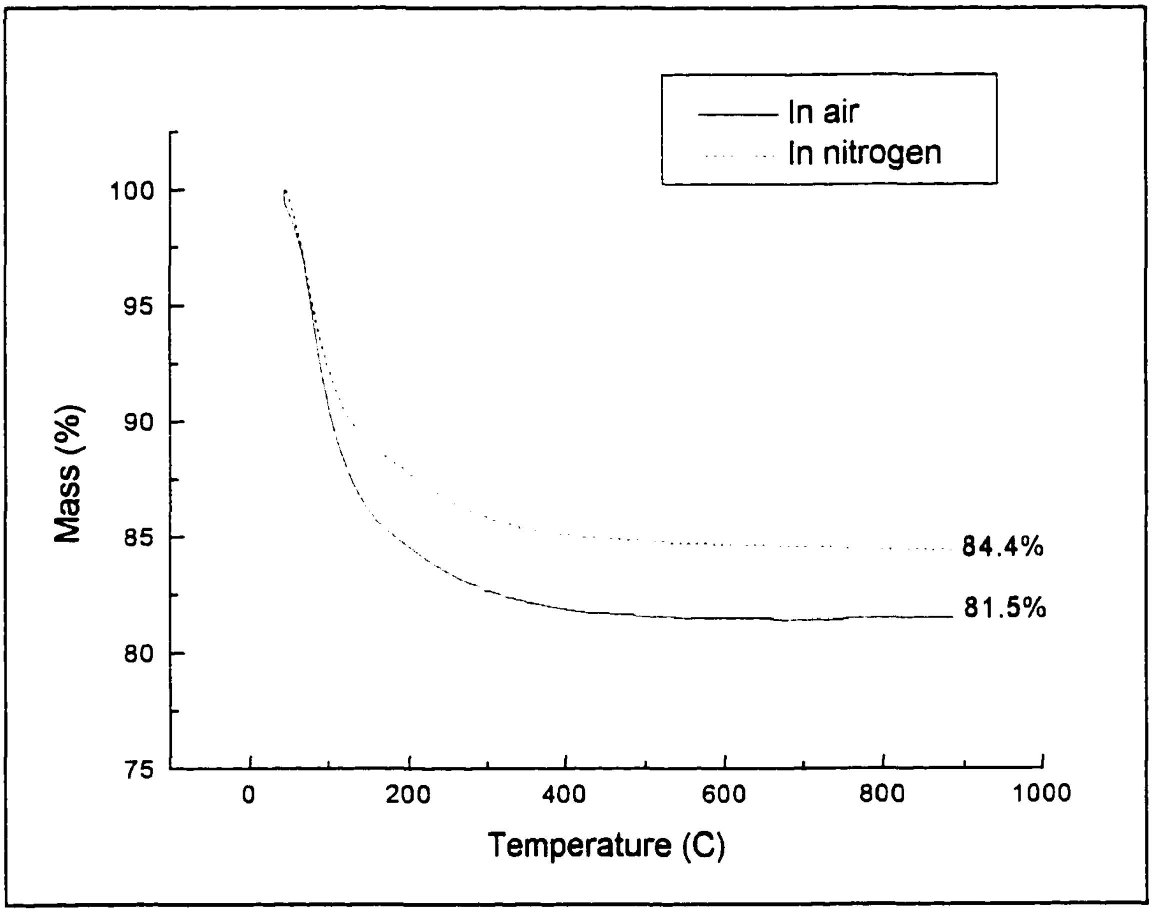

Figure 3-8 TGA of titanium dioxide aerogel in air and in a pure nitrogen atmosphere show a total mass loss of 18.5% and 15.6% respectively after washing.

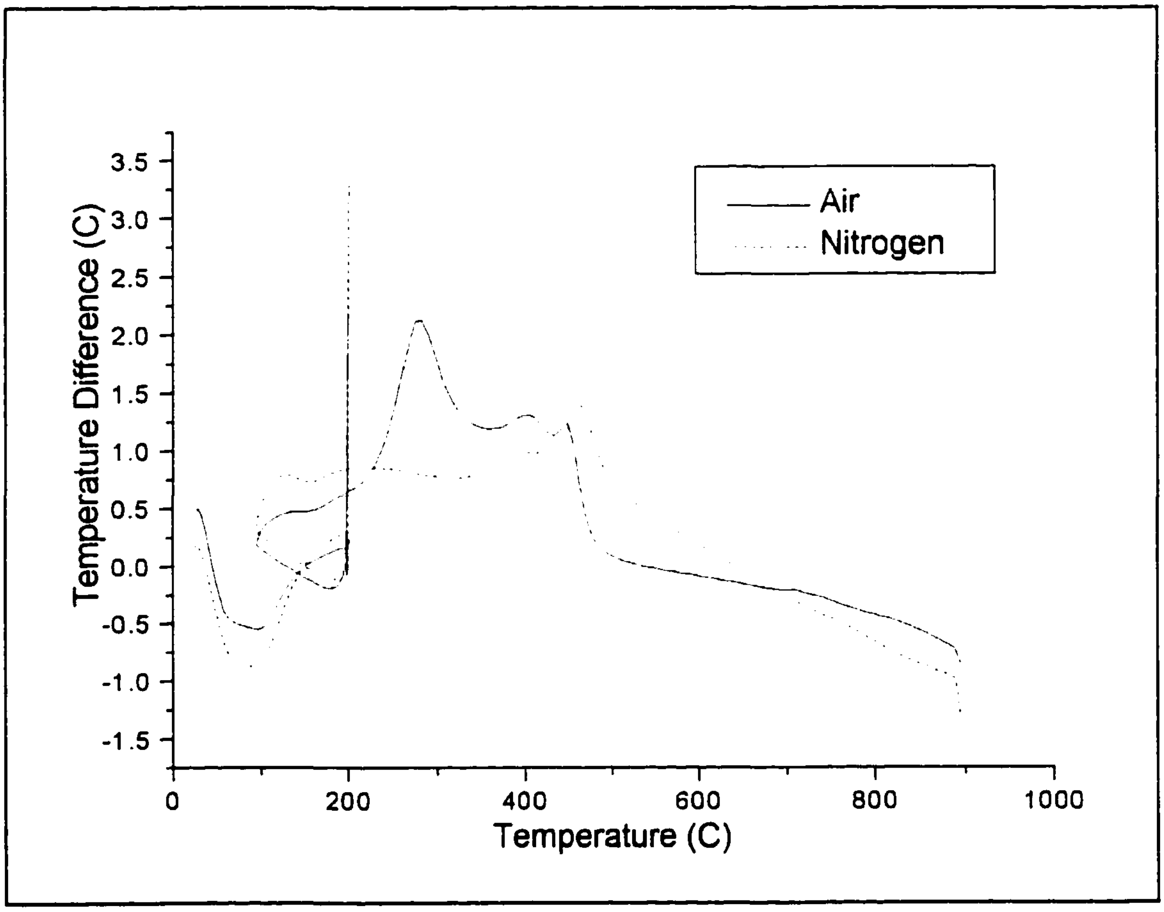

Figure 3-9 SDT of titanium dioxide aerogel in air and in a pure nitrogen atmosphere.

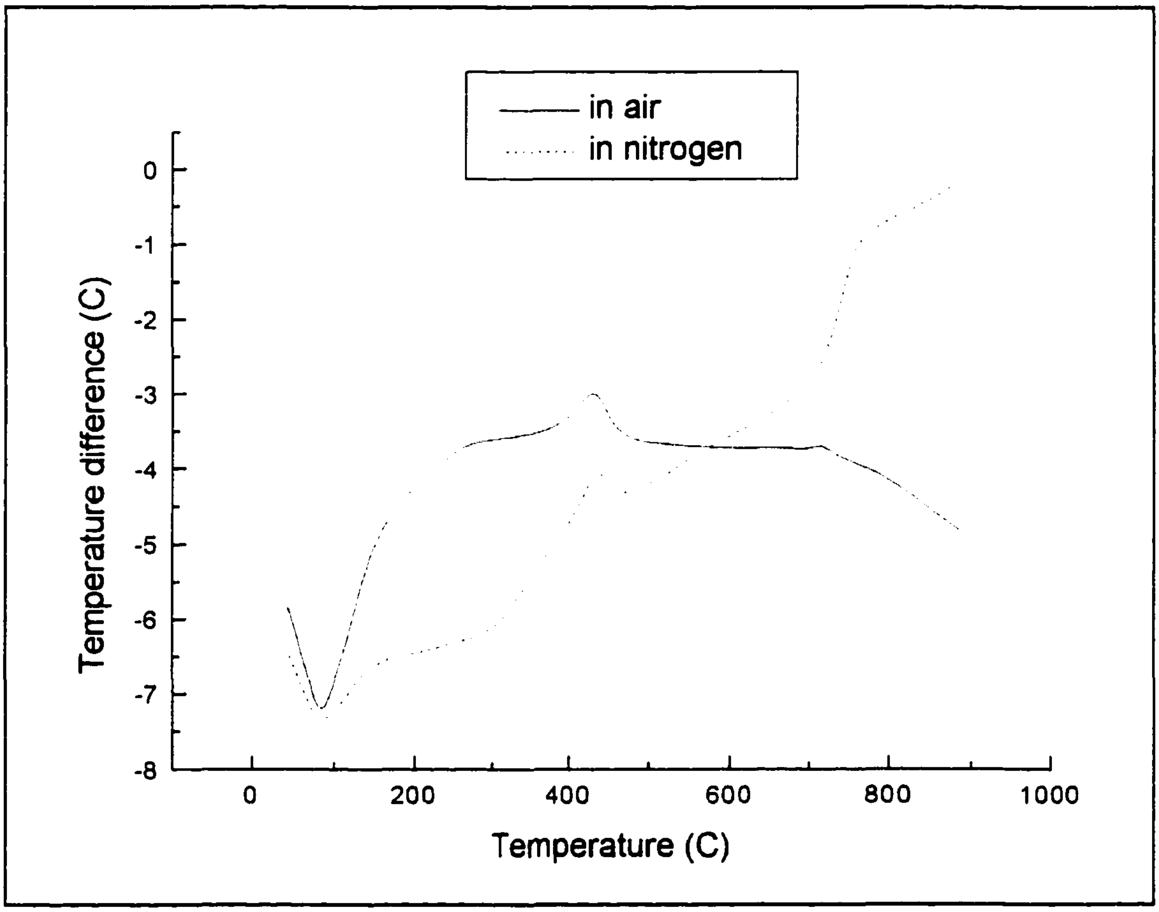

Figure 3-10 SDT of titanium dioxide aerogel after washing in air and in a pure nitrogen atmosphere.

Chapter 4 - SEM and TGA\SDT

SEM

The TiO_2 aerogel structure consists of two length scales: the nanocrystals and the mesospheres which are aggregates of nanocrystals[29]. Beautiful pictures of the morphology of the aerogel surface can be taken with a Scanning Electron Microscope which can magnify objects by a factor of as much as 500,000X.

The SEM used to examine the aerogel was a JEOL-6701F with a field emission tip. The field emission tip is much more efficient at extracting beam current than a typical hot cathode tip and as a result can be operated at much lower accelerating voltages. The field emission SEM is typically operated at only 2-5kV accelerating voltage. This low energy beam of electrons is less damaging than a high energy (25-30kV) beam of electrons which can actually cause a phase change of the aerogel sample from the influx of energy. Titanium dioxide aerogels are susceptible to another problem from this, a buildup of charge on the surface. With sufficient charge buildup on the surface, the fragile aerogel is literally ripped apart. It is possible to watch the aerogel fragmentation taking place during illumination by the electron beam. This is the primary reason for coating the samples with a gold film. The gold film conducts the electrons away from the sample so that charge buildup does not occur. It is important that the gold film be at least 50Å in thickness so that it is capable of carrying current. One drawback of using a small accelerating voltage is that the maximum magnification is only about 90,000X. If it is necessary to magnify more than this, a higher accelerating voltage must be used. At 30kV accelerating voltage, a maximum magnification of about 500,000X can be theoretically achieved. In practice, it is extremely difficult to achieve more than about 300,000X magnification since at this magnification, even subtle noises can disturb the image.

Samples are mounted using conductive graphite paint on aluminum stubs then coated with a conductive gold layer. Before coating with gold, the samples were baked for one hour at 150C to remove any moisture. Using an accelerating voltage of 10kV and a 5nm gold coating, it is possible to see the aerogel surface(Figure 4-1). From the SEM image the average mesosphere size of the untreated aerogel mesospheres is about 50nm. As stated earlier the size of the nanocrystallites increases with heating. As can be seen from the SEM image, the mesosphere size also increases(Figure 4-2). From the image, the average mesosphere size is about 70nm.

Attached to the SEM is an Energy Dispersive Spectroscopy (EDS) detector which can be used to analyze the elemental composition of the aerogel. Mostly this is uninteresting. The EDS works from the detection of X-ray photons which are emitted by Auger electrons falling into core levels of the atom. The energy signature of each atom is unique providing an easy means of identification of the atoms present. As can be expected the aerogel shows lots of Titanium and Oxygen as well as Carbon. This makes

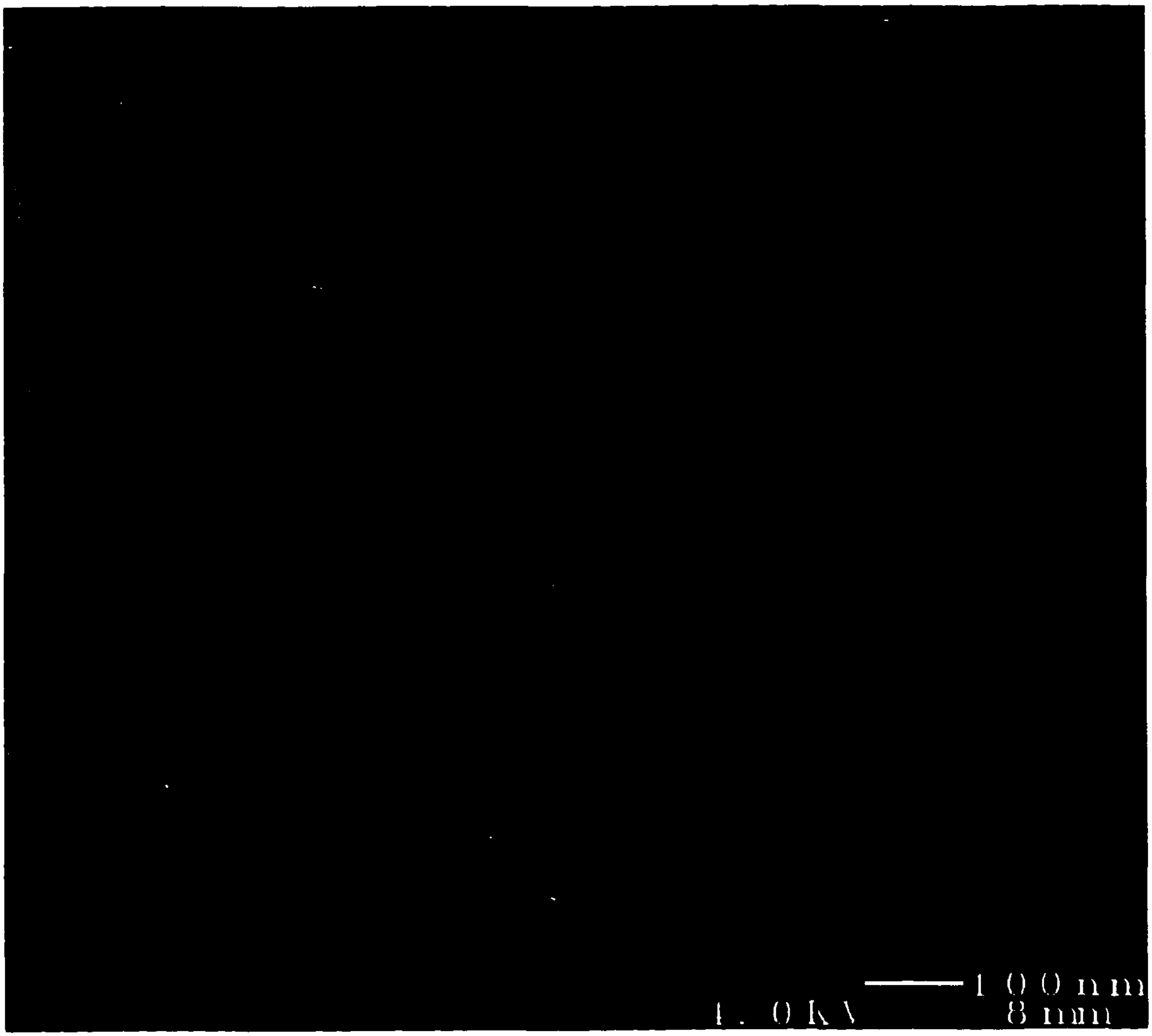

Figure 4-1 SEM of the aerogel structure before any heat treatment. Note the mesospheres are about 30nm in diameter.

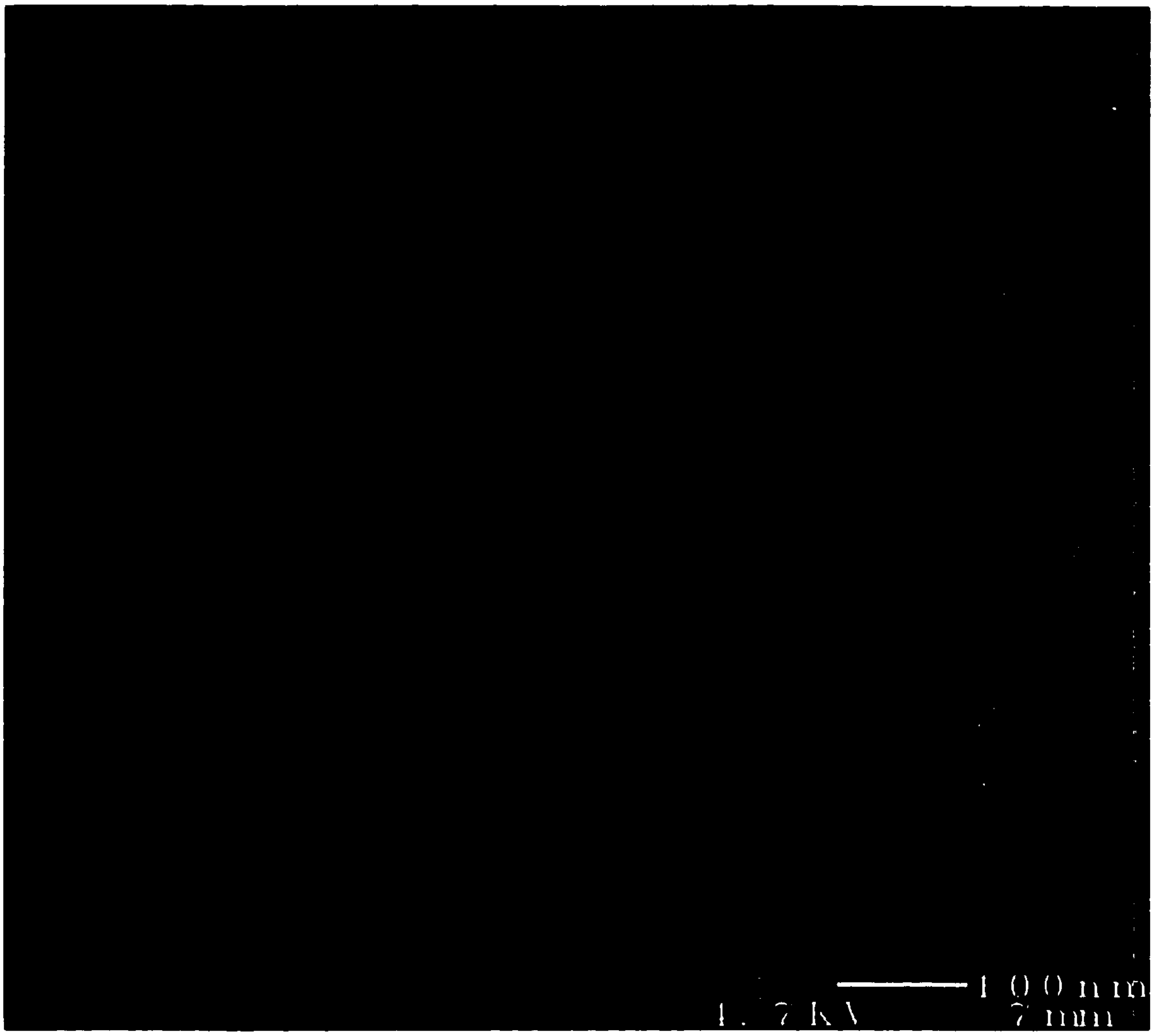

Figure 4-2 SEM of the aerogel structure after heat treatment at 900C. Note the mesospheres are about 70nm in diameter.

sense of course since the aerogel is being made through sol-gel synthesis in an Ethanol solvent. It might be more helpful in the studies of composite aerogels which have other materials embedded in them, either through doping or through inclusion of material during the sol-gel synthesis.

SEM pictures are good at showing the detail of the aerogel aggregation, particularly with regard to the mesospheres. It does not allow imaging of the nanocrystallites themselves. To image the nanocrystallites, it is necessary to use a Transmission Electron Microscope. TEM images have been used to verify the model of the aerogel that we use currently[29]. The size of the nanocrystallites may be measured from the TEM image or by X-ray powder diffraction.

TGA\ SDT

Thermal gravimetric analysis involves heating a sample from 30C - 900C at a constant temperature ramp of 10C/min and monitoring the mass change of the sample with a precise analytical balance. The aerogel samples are compared with (what is the comparison material again) which does not undergo any phase transitions in the temperature range being considered. Samples were heated in both an air and pure nitrogen environment to determine the effect of oxygen on mass changes. Mass loss/gain can occur for a number of reasons including: physical desorption, adsorption, oxidation liberating gaseous products, and thermal decomposition.

Experimental Setup and Results

Samples were weighed and placed in platinum cups inside the furnace of a TA Instruments model 2960 TGA/DTA. The samples were allowed to equilibrate and the scale to settle before beginning the experiment. The 2960 TGA/DTA was attached to an IBM PC which controlled the 2960 and provided data acquisition. The 2960 does simultaneous TGA and DTA, but these signals have been separated for clarity. The rate of heating is an important parameter in the TGA experiments because it determines the rate of change of mass. For very slow temperature ramp rates, the data is difficult to interpret as there are no sharp features in the curve. Typically the ramp rate is 10C/min or 15C/min. As discussed earlier, the washed aerogel sample shows only those peaks of interest, connected with the titanium dioxide itself.

Scanning Differential Thermometry

As the samples are heated, heat flows into the samples from the oven. Reactions taking place in the sample as a result of heating will mean that extra heat is absorbed or released in endothermic and exothermic processes. Used in conjunction with the TGA, it is possible to differentiate oxidation processes(mostly exothermic) from desorption processes(endothermic) and phase changes (endo- or exothermic).

Of real interest is the data for the washed aerogel (Figure 4-3) . There is a large endothermic process in the temperature range of 30C to 200C, which is accompanied by a large mass loss. This is reasonably interpreted to be due to the desorption of water. The

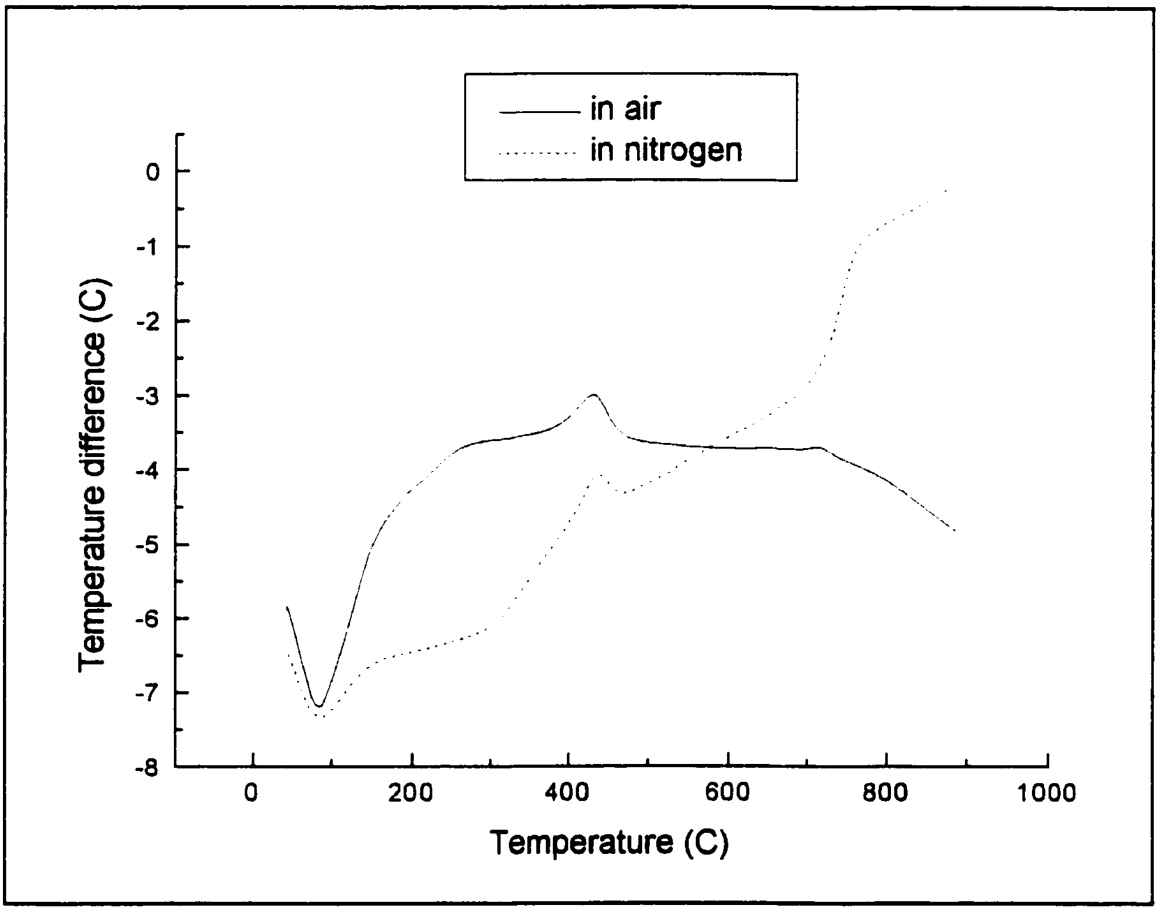

Figure 4-3 The SDT signal for the washed aerogel in air and nitrogen is much simpler than the unwashed aerogel indicating that it has been cleaned of organic residues.

washed aerogel spectra shows three peaks: a very small peak at 257C, a peak at 428C and a small peak at 709C. Other authors have attributed the peak at 257 with the oxidation of Ti dangling bonds at the surface. Although there is no mass gain which should accompany oxidation, this may be because there still a net decrease of mass from loss of bound alcohol groups. The peak at 450C has been identified as the transition between amorphous and anatase crystalline form[36]. The peak at 709C appears to be the transition of anatase to rutile (Figure 4-4). From X-ray spectra of the aerogel, it is clear that the transition does take place for heating above 700C. Calibration of the SDT spectra is done by measuring two known materials with transition temperatures near the peak of interest. In the case of the peak at 709C, aluminum is measured with a phase transition at 660.325C and potassium bromide is measured with a phase transition at 734C. In this way the transition at 709C is interpolated and determined to have a heat of fusion, $\Delta H_f =$ 4.13kcal/mole. This is the same order of magnitude, but a factor of about three larger than the heat of fusion for the transition of anatase to rutile $\Delta H_f = 1.16$kcal/mole.

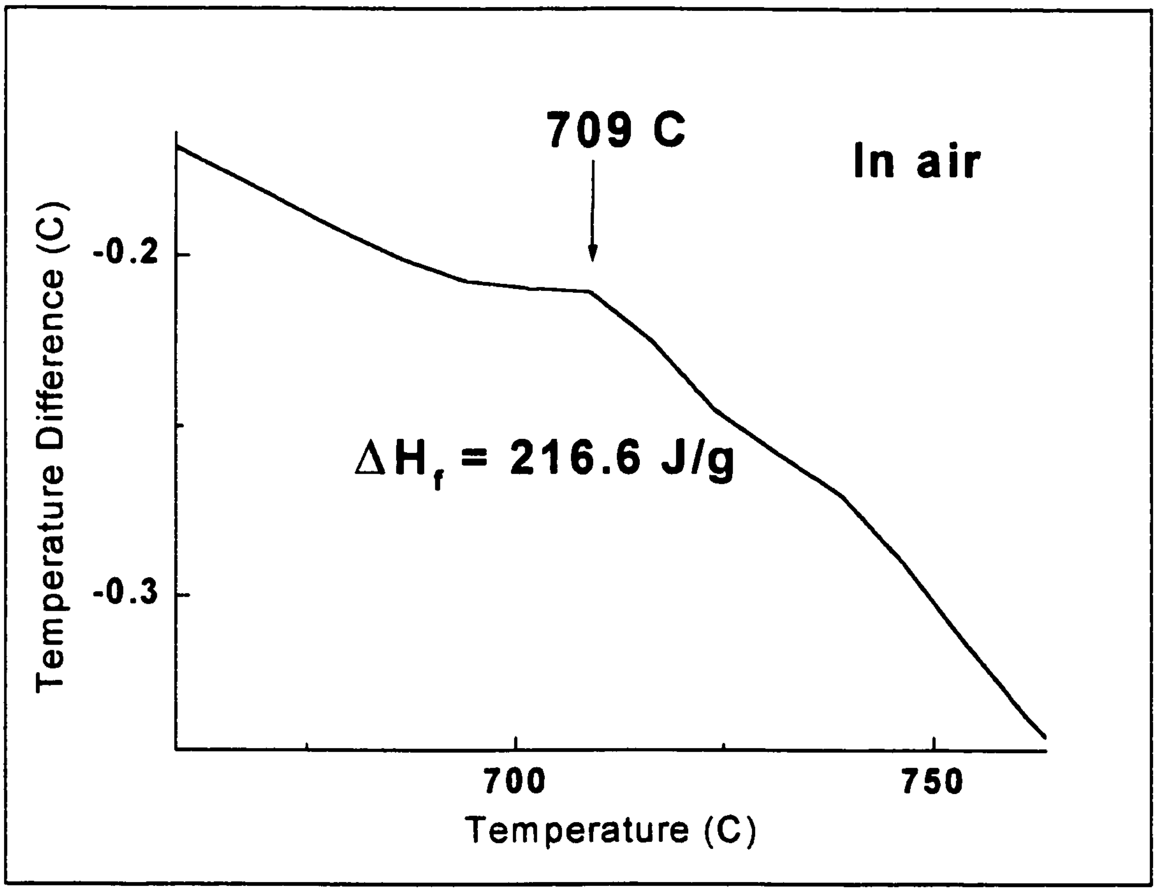

Figure 4-4 The peak at 709C corresponds to the phase change of anatase to rutile.

Chapter 5 - Raman Spectroscopy

Theory of Raman Scattering in Crystals

Inelastic Raman Scattering occurs when light interacts with molecules or lattices of atoms in a crystal arrangement. The scattering of light by Raman scattering in a crystal refers to the creation or annihilation of a phonon. First-order Raman effect refers to the creation or destruction of a single phonon. The frequency and momentum of the incident radiation will be shifted by an amount (Equation 5-1):

$$\begin{aligned} \omega_f &= \omega_i \pm \omega \\ q_f &= q_i \pm q_{phonon} \end{aligned} \qquad \textbf{(5-1)}$$

Where ω_f (q_f) refers to the final frequency (momentum) of the radiation, ω_i (q_i) refers to the incident frequency(momentum), and ω_{phonon}(q_{phonon}) is the frequency(momentum) of the created or destroyed phonon. When a phonon is created(-), the final frequency will be smaller than the incident frequency and this is known as the Stokes component of the spectra. When a phonon is destroyed(+), the final frequency will be higher than the incident frequency and this is known as the anti-Stokes component. Not all lattice vibrations can be stimulated purely by interaction with light. Those lattice modes which have the correct symmetry can be stimulated by interaction with light and those modes are said to be Raman active. Of course, multiple phonon events can occur as well, and these are called second order, third order, etc scatterings. In the following discussion, all of the Raman peaks discussed are single phonon scatterings.

In general phonons can have a wave-vector which is as large as the Brillouin zone, about $\vec{q} \approx \pi/L$ where L is the dimension of the lattice constant. Typically then, phonons can have wave-vectors as large as $\vec{q} \approx 3 \cdot 10^{8}$ cm^{-1} (since typical crystal dimensions are $\sim 10^{-8}$cm). Light on the other hand has a wave-vector inside the crystal of only $\vec{q} \approx 2 \cdot 10^{5}$ cm^{-1}. If we collect the back-scattered light at an angle of about 180°(Figure 5-1), then by wave-vector conservation (momentum) the phonon can only have a wave-vector of $2 \cdot 2 \cdot 10^{5}$ cm^{-1}. This means that optic phonons with a wave-vector near the center of the Brillouin zone ($\vec{q} \approx 0$) can take part in RS. In addition to this consideration, it is also important to recognize that the phonon frequency is dependent on the direction of propagation as well as momentum, $\omega(\vec{q})$, i.e. a phonon dispersion curve. Phonon dispersion curves are typically measured by neutron scattering.

Although the phonon dispersion curves can be quite complex functions of the phonon wave-vector, it is fairly simple to show that a given branch of the phonon dispersion curve can be parametrized by two numbers. These numbers depend only on the total size of the dispersion and also how quickly the dispersion changes. Using a linear chain model of a one dimensional crystal, the phonon dispersion is derived as follows. In order to have optic phonons, it is necessary to have two or more atoms per unit cell. The linear chain model of a crystal consists of a chain of pairs of atoms with mass M_1 and M_2 (Figure 5-2). The atoms are connected by "springs" of spring constant k.

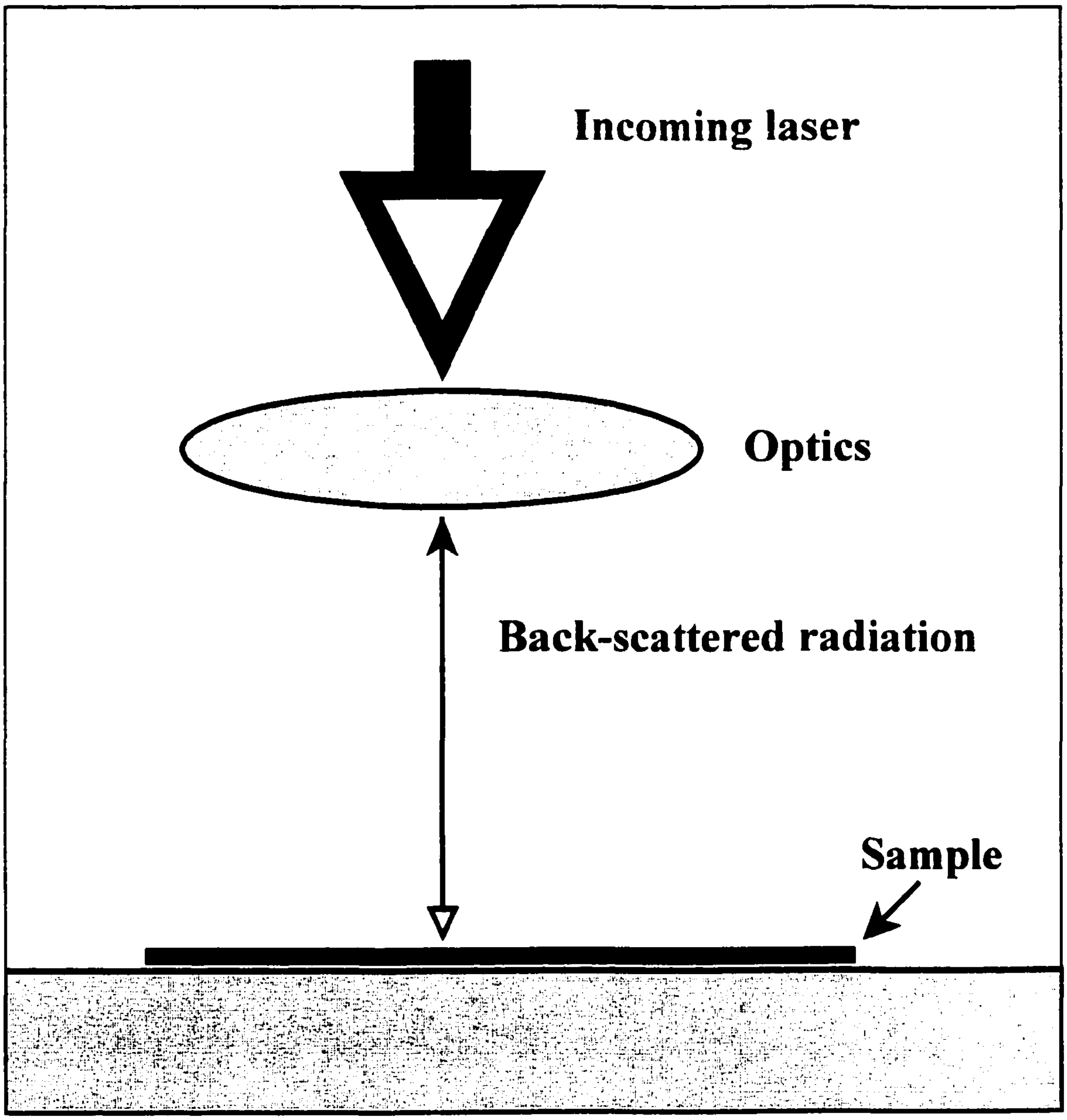

Figure 5-1 Raman scattered light in the back-scattering configuration, can impart a maximum $\Delta q = 2k$ to created phonons. Where k is the wave-vector of the incoming light.

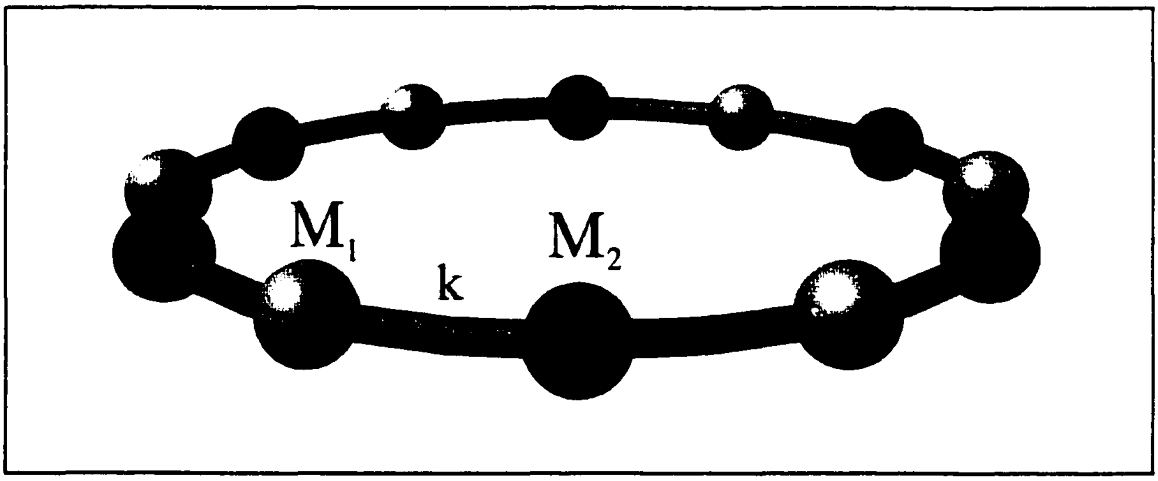

Figure 5-2 A ring of atoms, with masses M_1 and M_2, and spring constant k between them. This model can be used to derive a simple phonon dispersion relation.

The pairs of atoms are separated by a distance of **a** at equilibrium. In order to reproduce the translational symmetry of a real crystal the ends of the chain are joined together to create a ring. Also we assume that there are N of these pairs of atoms. If u_i and v_i represent the positions of the atoms in each pair then the harmonic potential energy is:

$$U^{harm} = \frac{k}{2}\sum_N [u_i - v_i]^2 + \frac{k}{2}\sum_N [v_i - u_{i+1}]^2 \qquad \textbf{(5-2)}$$

The 1-dimensional equation of motion for the nth set of masses is:

$$\begin{aligned} M_1\ddot{u}_n &= -\frac{\partial U}{\partial u_n} = k(v_n + v_{n-1} - 2u_n) \\ M_2\ddot{u}_n &= -\frac{\partial U}{\partial v_n} = k(u_{n+1} + u_n - 2v_n) \end{aligned} \qquad \textbf{(5-3)}$$

By imposing the Born-von Karman periodic boundary conditions and assuming a

$$\begin{aligned} u_i([N+1]a) &= u_i(a) \\ v_i([N+1]a) &= v_i(a) \\ u_i(0) &= u_i(Na) \\ v_i(0) &= v_i(Na) \\ u_n &= \varepsilon_1 e^{i(\omega t + qna)} \\ v_n &= \varepsilon_2 e^{i(\omega t + qna)} \end{aligned} \qquad \textbf{(5-4)}$$

traveling wave solution, with ε_1 and ε_2 being amplitudes for the traveling waves

Substituting 5-4 into 5-3 the equations of motion become:

$$\begin{aligned} -\omega^2 M_1\varepsilon_1 &= k\varepsilon_2(1+e^{-iqa}) - 2k\varepsilon_1 \\ -\omega^2 M_2\varepsilon_2 &= k\varepsilon_1(1+e^{iqa}) - 2k\varepsilon_2 \end{aligned} \qquad \textbf{(5-5)}$$

The non-trivial solution is found by setting the determinant of the coefficients equal to zero.

$$\begin{vmatrix} 2k - M_1\omega^2 & -k(1+e^{-iqa}) \\ -k(1+e^{iqa}) & 2k - M_2\omega^2 \end{vmatrix} \equiv 0 \qquad \textbf{(5-6)}$$

Which leads to the following formula for ω:

$$M_1 M_2\omega^4 - 2k(M_1 + M_2)\omega^2 + 2k^2(1 - \cos qa) \equiv 0 \qquad \textbf{(5-7)}$$

Finally the phonon dispersion looks as follows:

$$\frac{\omega(q)^2}{\omega_0^2} = A + [A^2 - B(1-\cos(qa))]^{1/2} \qquad \textbf{(5-8)}$$

Using a negative (positive) value for parameter B makes the dispersion positive (Figure 5-3) (negative (Figure 5-4)). For a positive dispersion of 80%, A=0.5 and B=-3.6288 would give a value of $\omega = \omega_0$ at the center of the BZ and $\omega = 1.8\omega_0$ at eh edge of the BZ. For interactions between neighboring atoms, the dispersion is typically negative, while it can be either positive or negative for long-range interactions. Obviously this model will not fully mirror an actual phonon dispersion. This simple model is spherically symmetric and assumes no directional dependence for ω. In reality, phonon dispersion curves are a

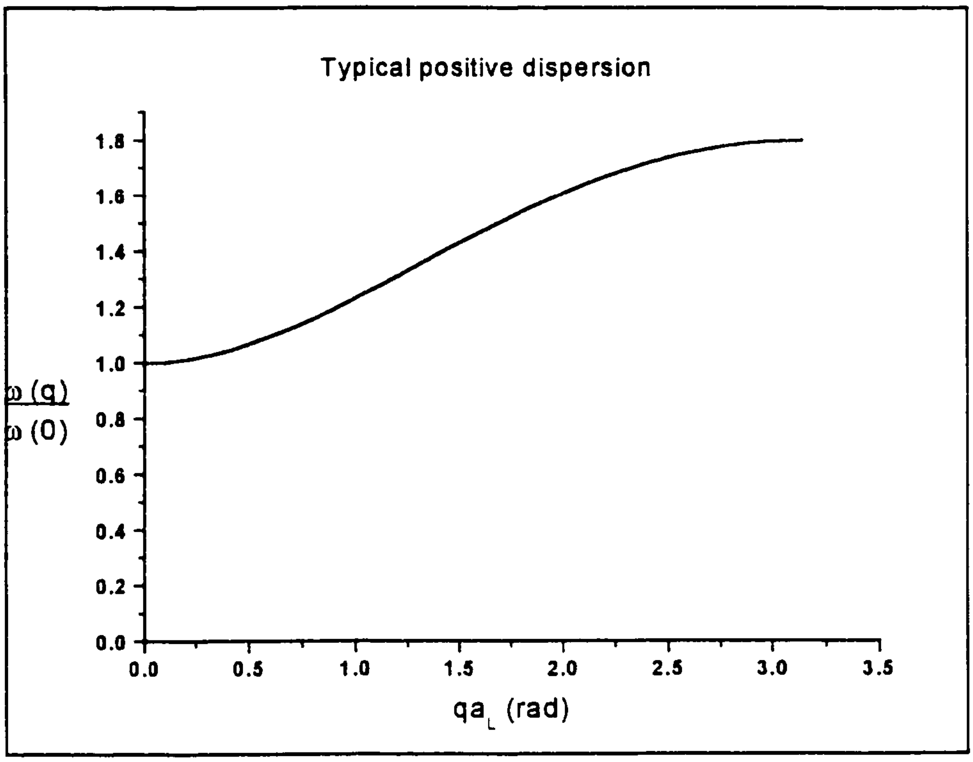

Figure 5-3 Typical positive phonon dispersion, with a total dispersion of 80%.

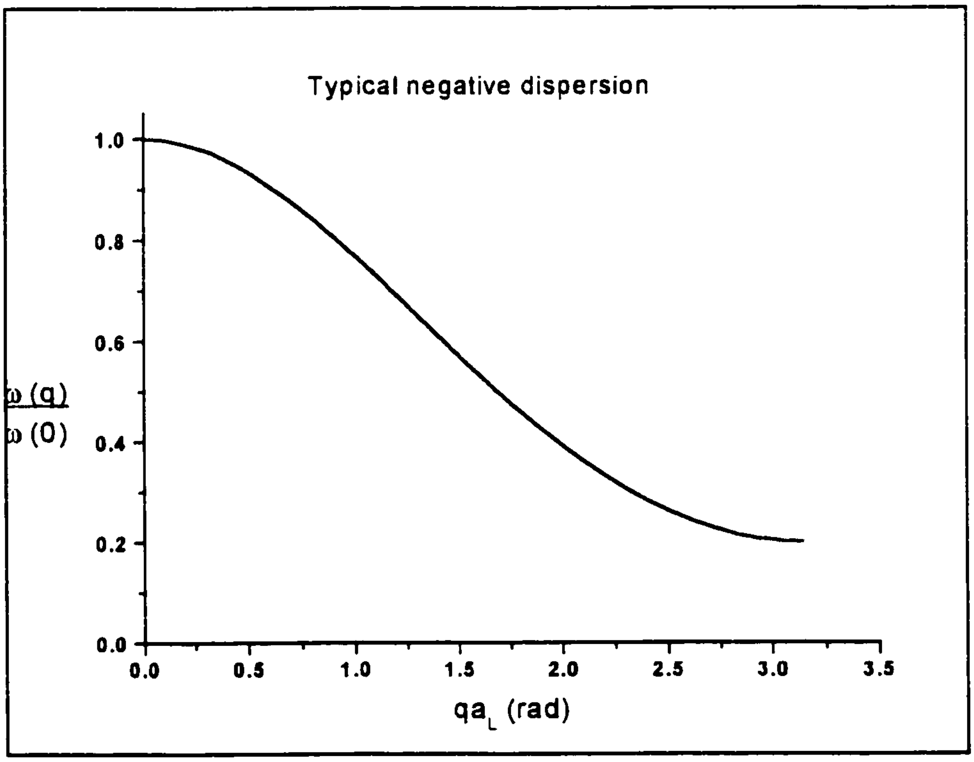

Figure 5-4 Typical negative phonon dispersion, with a total dispersion of 80%.

function of wave-vector, $\vec{q}$, i.e. $\omega(\vec{q})$. The functional relation (Equation 5-8) can be used to fit certain branches of the phonon dispersion. Although this model is wrong for a number of reasons, it can be shown to fit reasonably well with real-world phonon dispersions. In particular it can be used to fit the optic phonon branch (E_g) for rutile which is $144 cm^{-1}$ at the center of the BZ.

In a single crystal then, the phonon excitation will have a frequency as determined by $\omega(\vec{q} \approx 0)$. The photon typically will have a very small momentum which it can impart to a phonon. For materials with no long range order, such as amorphous or glass materials, the phonons do not necessarily have $\vec{q} \approx 0$, because there is no phonon localization. The Raman spectra for amorphous materials is quite diffuse and actually represents the phonon density of states in the medium[37]. For materials with micro or nano-crystallinity, we have an intermediate case. The phonons are localized to the crystallites so that $\Delta x \sim L$, the size of the crystallite. In this case, the uncertainty relation ($\Delta x \cdot \Delta q \sim 2\pi$) requires that the uncertainty in phonon wave vector, $\Delta\vec{q} \geq 2\pi/L$.[38] The implication of this is that the phonons excited in a nano-crystalline material will not have a single frequency, but will be a distribution of frequencies from the phonon dispersion relation.

For a single crystal, the RS consists of sharp Lorentzian peaks which are convoluted with instrumental broadening. The peaks represent the Raman active phonon modes in the material. The full-width at half maximum (FWHM) for each peak is called the intrinsic half-width, and it is different for each peak. With micro or nano-crystalline material the phonons are no longer confined to $\vec{q} \approx 0$, but can exist at any wave-vector up to 2π/L. As a result of the frequency distribution, the RS peaks are broadened asymmetrically. This situation has been investigated by Pollak and for a spherically symmetric phonon dispersion, the expression for the intensity of the Raman peak will be given by:

$$I(\omega) \propto \int dL\rho(L) \int_{BZ} \exp(\frac{-q^2 L^2}{8}) \frac{d^3 q}{[\omega - \omega(\vec{q})]^2 + [\frac{\Gamma_0}{2}]^2} \tag{5-9}$$

Where ρ(L) is the particle size distribution and Γ_0 is the intrinsic line width and q is in units of π/a_L with a_L being the average crystal lattice size. In the case of a positive(negative) dispersion, the QVRM predicts that a peak will be asymmetrically broadened on the high(low) frequency side and a blue-shift(red-shift) of the peak location for decreasing crystallite size. Although other mechanisms, e.g. strain[39], can predict a peak shift, the QVRM is the only known model which can simultaneously account for changes in the peak broadening, the peak shift and the peak asymmetry. For a mono-disperse particle size distribution, the first integral containing ρ(L) will be a constant, namely the number of particles. For a non-uniform particle size distribution, the broadening of the peak and the peak distribution due to particle size will overlap and result in a rather complex expression. In the past a purely empirical has been used to show a linear relationship between crystallite size and the intensity of Raman peaks[40].

Raman spectroscopy has been used for years as a qualitative tool for the identification of materials and contaminant or dopants. Some work has been done on the evolution of solution structure the work of Doss and Zallen[41] with sol-gel synthesis of alumina and the work of this author[42]. Doss and Zallen used a variety of techniques to qualitatively interpret Raman data in terms of the known morphology. They see a shift in the Raman peak location as well as a broadening as a function of particle size, and mention finite-size as a mechanism for the changes. Pollak[43] has shown that the QVRM can explain observed asymmetry, broadening and peak shift in the Raman spectra of porous silicon. Another study by Bersani et al.[44] invoked the QVRM to qualitatively explain observed shift and broadening, but they failed to fully use the model to it's potential.

Raman spectroscopy was performed with the 514.5nm line of a multi-mode Ar^+-ion laser as an excitation source. The laser power was about 500mW, and no changes in the line shape of the Raman spectra were noticed with variation in the laser intensity. Light was collected in the back-scattered geometry, and passed through a Jobin-Yvon T 64000, triple mono-chromator with 1200 lines/cm crystal gratings. The instrumental resolution was about 0.4cm^{-1}, and the light was collected with a CCD (0.6cm^{-1} resolution).

Single crystal spectra are generally quite sharp (i.e. FWHM of ~10 cm^{-1}), and are broadened by thermal broadening[45]. The Raman spectra of single crystal anatase was measured by Berger, Tang and Levy and the Raman optical modes are shown in Table 5-1[8], with assignment of the symmetry mode designations[13]. Berger et al. describe the peak at 145.0cm^{-1} as "an E_g mode related to a O-Ti-O bending mode characterized by a soft force constant"[11]. The peak at 145.0 is the most prominent feature in the spectra of anatase(Figure 5-5) and for that reason we followed the evolution of this peak in the aerogel samples.

$Y(P_1P_2)Y$ $\vec{q} \parallel [010]$	$Z(P_1P_2)X$ $\vec{q} \parallel [101]$	Symmetry Mode Designation
638.7	637.8	E_g
515.3	513.9	B_{1g}
515.3	513.9	A_{1g}
397.0	398.0	B_{1g}
197.5	198.2	E_g
143.7	145.0	E_g

Table 5-1 The Raman spectra peaks for anatase single crystal for the [010] and [101] excitation directions, as well as their symmetry designation.

Similarly the Raman spectra for rutile (Figure 5-6) is also well known, as it was first measured by Porto et al in 1972[46]. The aerogel consists entirely of anatase when it is first made, and it is only after heating >700C that the transformation to rutile begins to occur. For comparison, we have measured the Raman spectra of Degussa P25(Figure 5-7), and it shows a combination of the spectra for anatase and rutile. In fact Degussa P25 powder is a mixture (75%/25%) of anatase and rutile. The aerogel begins with only anatase peaks(Figure 5-8). As the aerogel is heated to about 500C, the size of the crystallites grows and the Raman peaks become sharper(Figure 5-9). Heating to a temperature of about 700C causes the anatase to begin changing phases to rutile(Figure 5-10). Finally

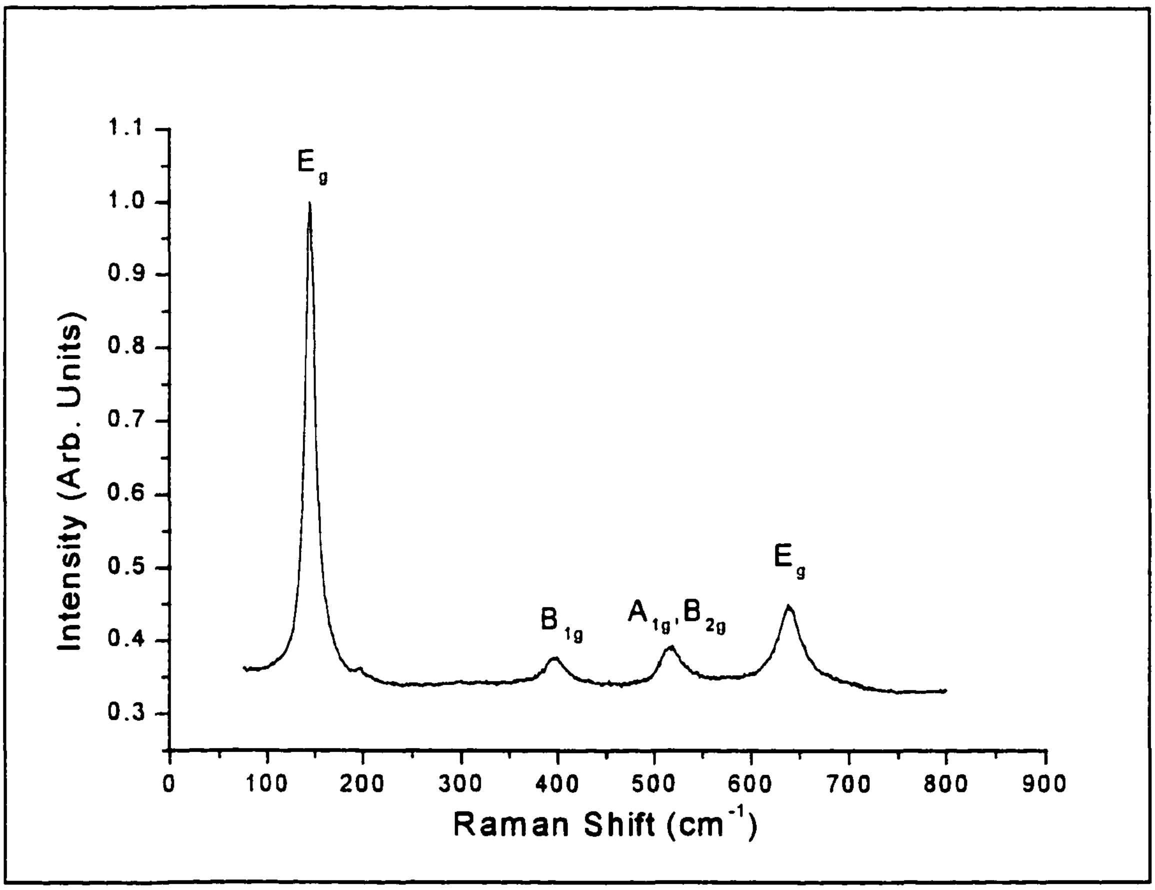

Figure 5-5 Raman spectra of single crystal anatase (randomly oriented with respect to incoming light)

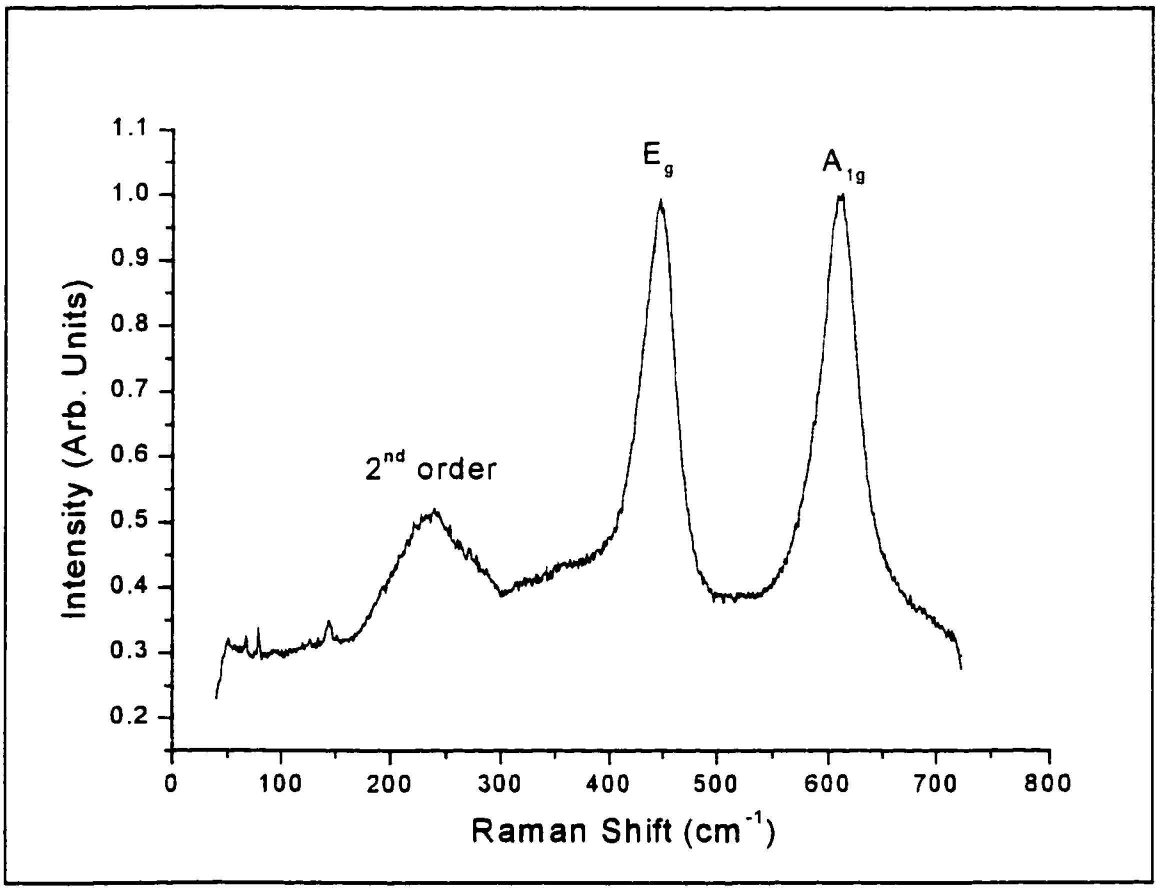

Figure 5-6 Raman spectra of single crystal rutile (randomly oriented with respect to incoming light). The symmetry designations for the phonon modes are noted, including a second order peak at225cm^{-1}.

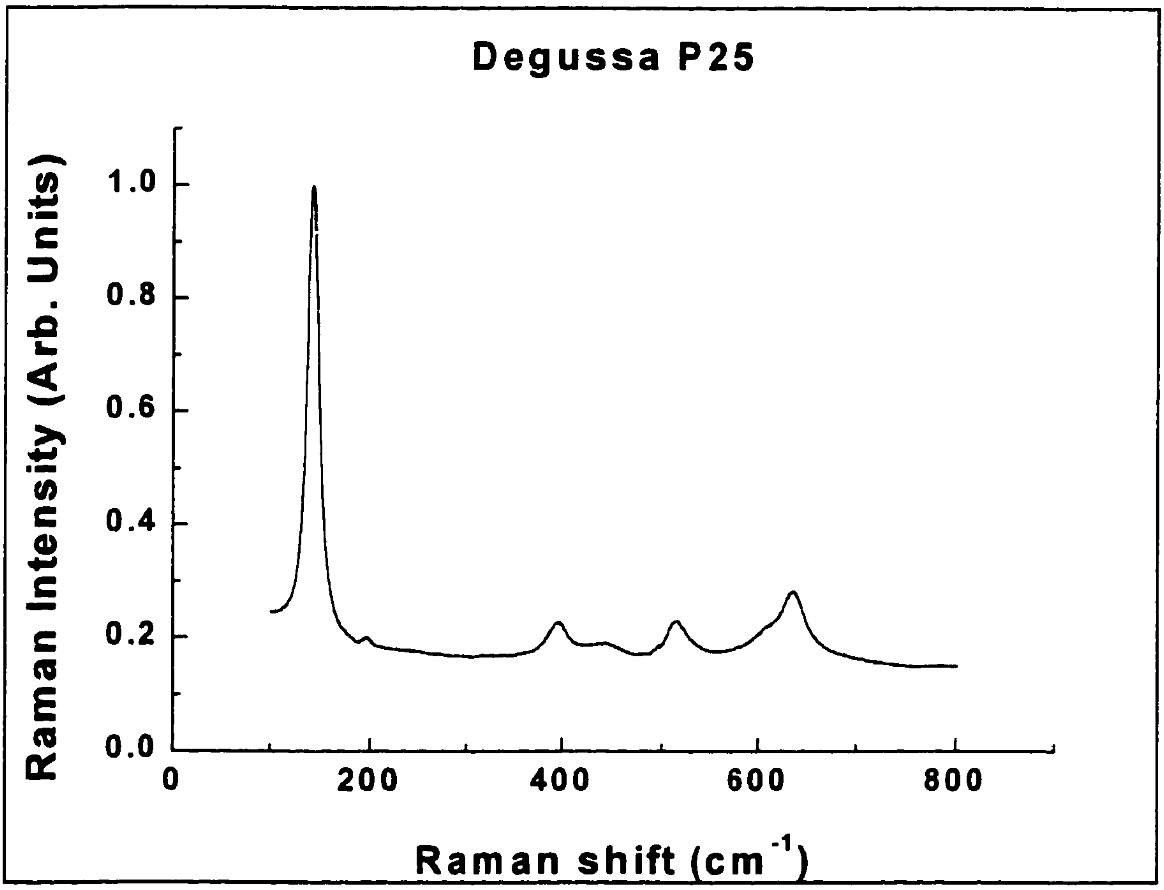

Figure 5-7 Raman spectra of Degussa P25 powder shows a combination of peaks from the anatase and rutile spectra.

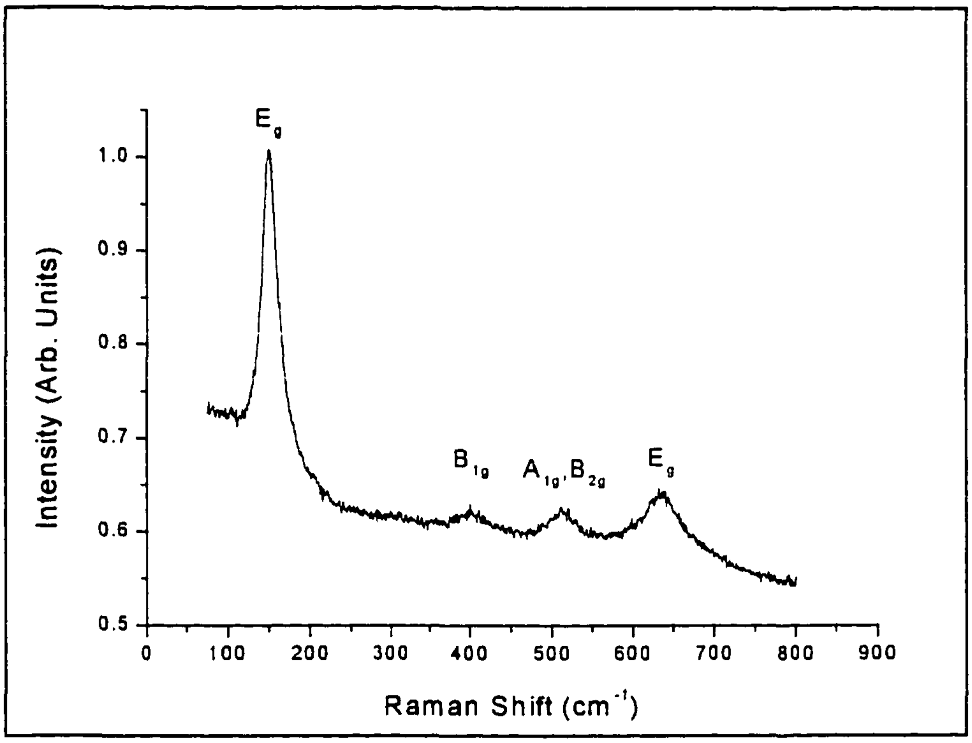

Figure 5-8 The unheated titanium dioxide aerogel is the same spectra as anatase, with much broader line widths than the single crystal.

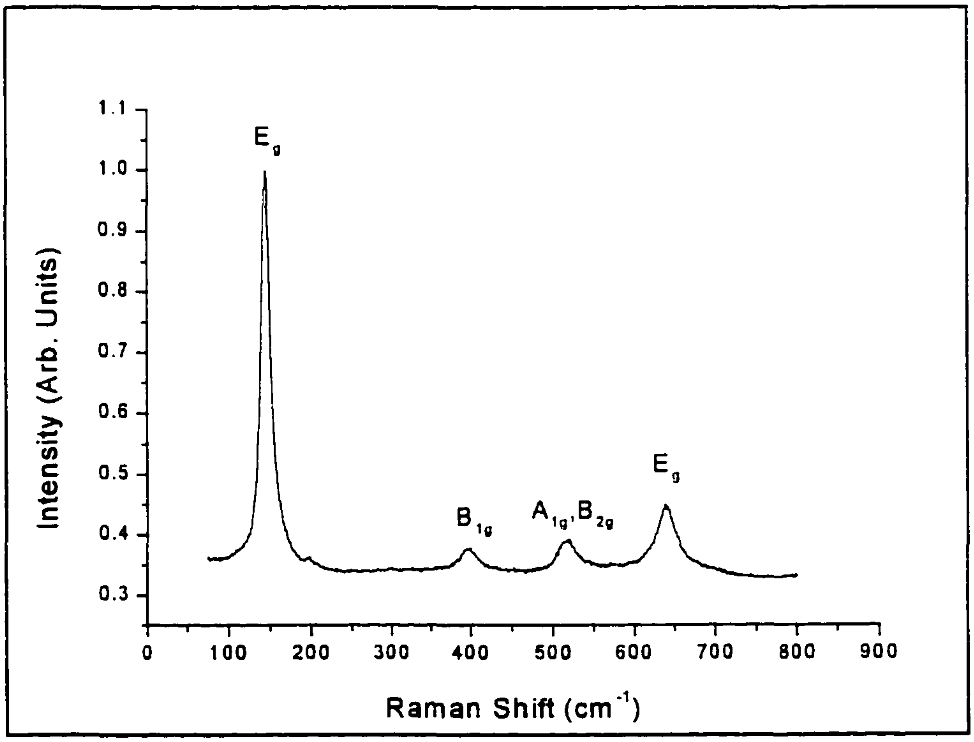

Figure 5-9 The titanium dioxide aerogel baked at a temperature of 500C shows a Raman spectra of anatase, with smaller line widths than the unheated aerogel.

after heating to a temperature of 900C, all of the anatase has transformed to rutile(Figure 5-11).

Results

The most intense peak in the anatase spectra is the E_g peak located at $145.0cm^{-1}$ for the single crystal. As the size of the average crystallite decreases, the shape of the Eg peak changes: the location of the peak is blue-shifted to higher energy (higher wave-vector), the peak broadens asymmetrically on the high energy side. In Figure 5-12 the effect of changing crystallite size is seen by comparing the smallest and largest crystallites $145.0cm^{-1}$ peak.

In relating the various Raman peaks the Raman Shift and FWHM are defined relative to the single crystal values of $145.0cm^{-1}$ for the peak location, and $9cm^{-1}$ for the FWHM[47]. Then the fractional peak shift is defined to be the change in the E_g peak location from $145.0cm^{-1}$ divided by $145.0cm^{-1}$. The fractional FWHM is defined to be the FWHM divided by $9cm^{-1}$. In Figure 5-13, the fractional Raman shift for the E_g peak versus crystallite size shows a rapid decline with increasing crystallite size. The FWHM also shows a rapid decline with increasing crystallite size(Figure 5-14). The fractional FWHM and fractional Raman Shift have a roughly linear relationship(Figure 5-15).

In order to test the validity of the QVRM, it was necessary to generate theoretical spectra

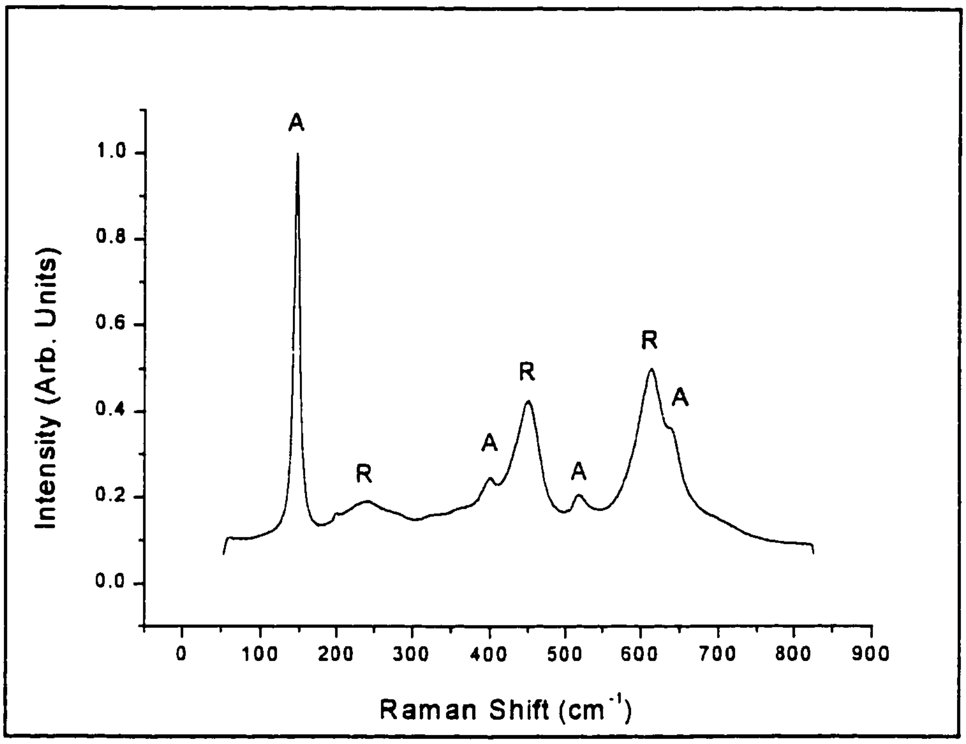

Figure 5-10 The titanium dioxide aerogel baked at a temperature of 700C shows that the anatase is partially converted to rutile. The Raman spectra resembles a mixture of anatase and rutile, similar to the Degussa powder.

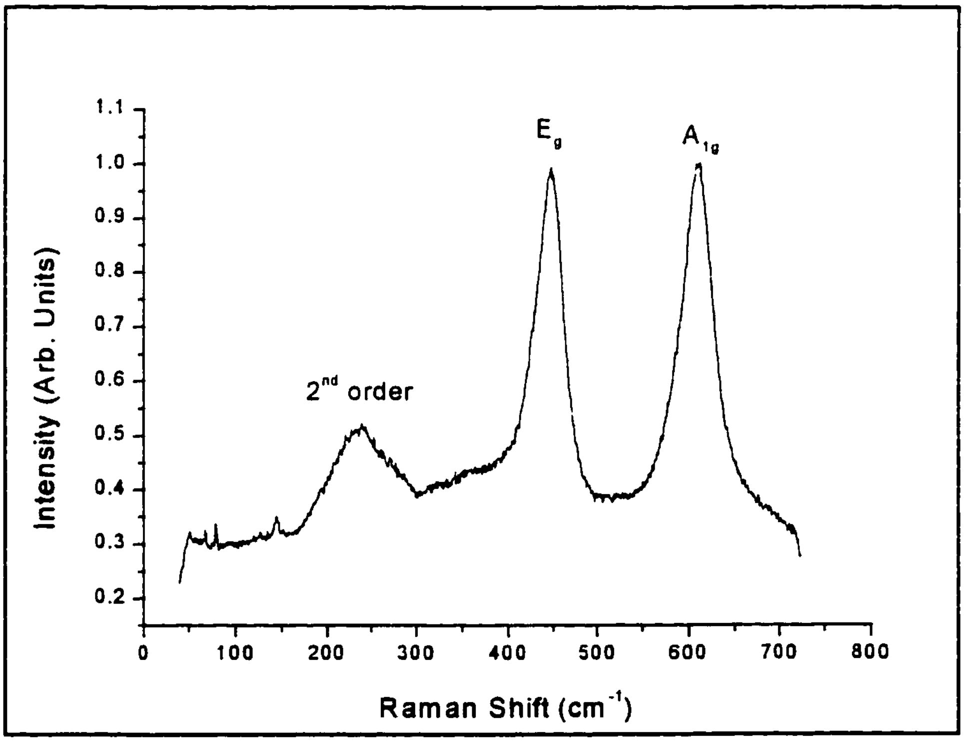

Figure 5-11 The titanium dioxide aerogel baked at a temperature of 900C shows a Raman spectra of rutile. All of the anatase has been converted to rutile at this point.

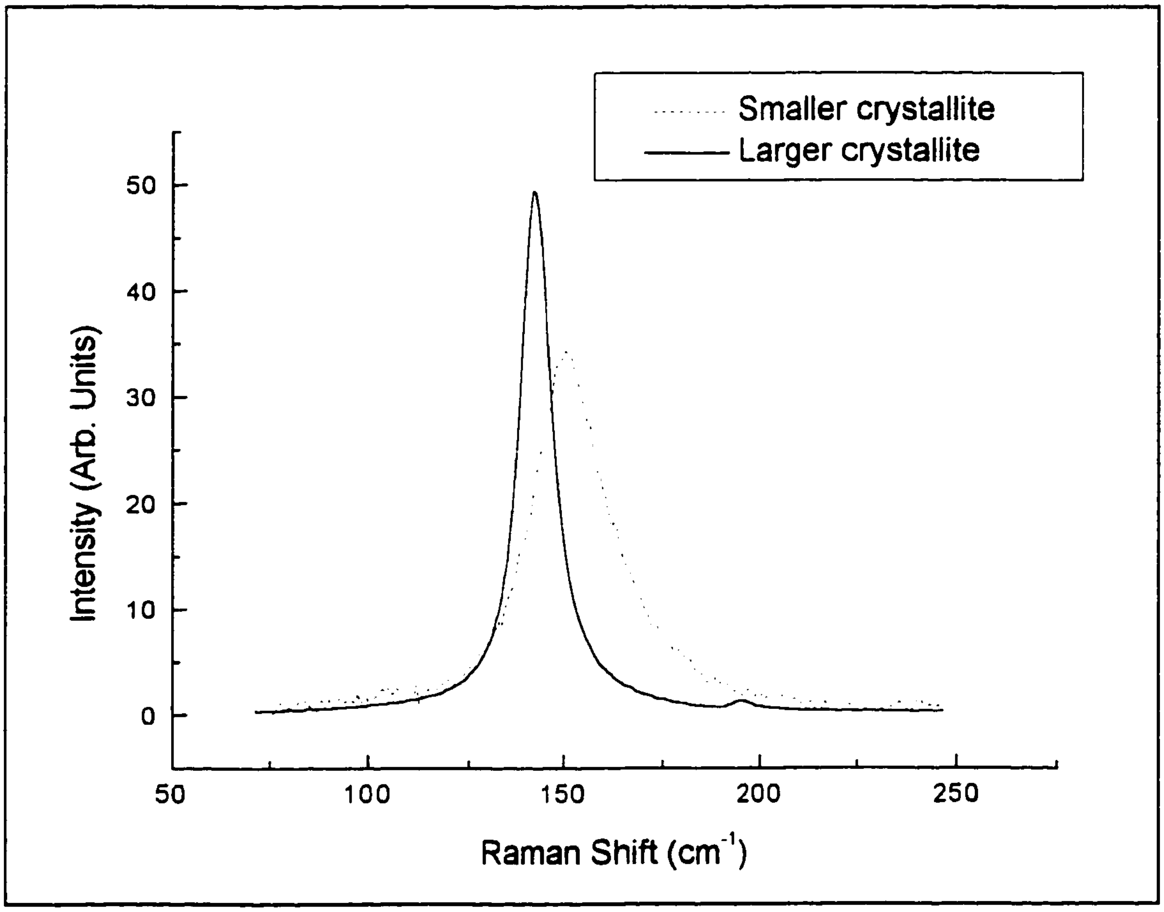

Figure 5-12 The E_g mode Raman peak located near 145.0cm^{-1} for the smallest (dotted line) and the largest (solid line) crystallites.

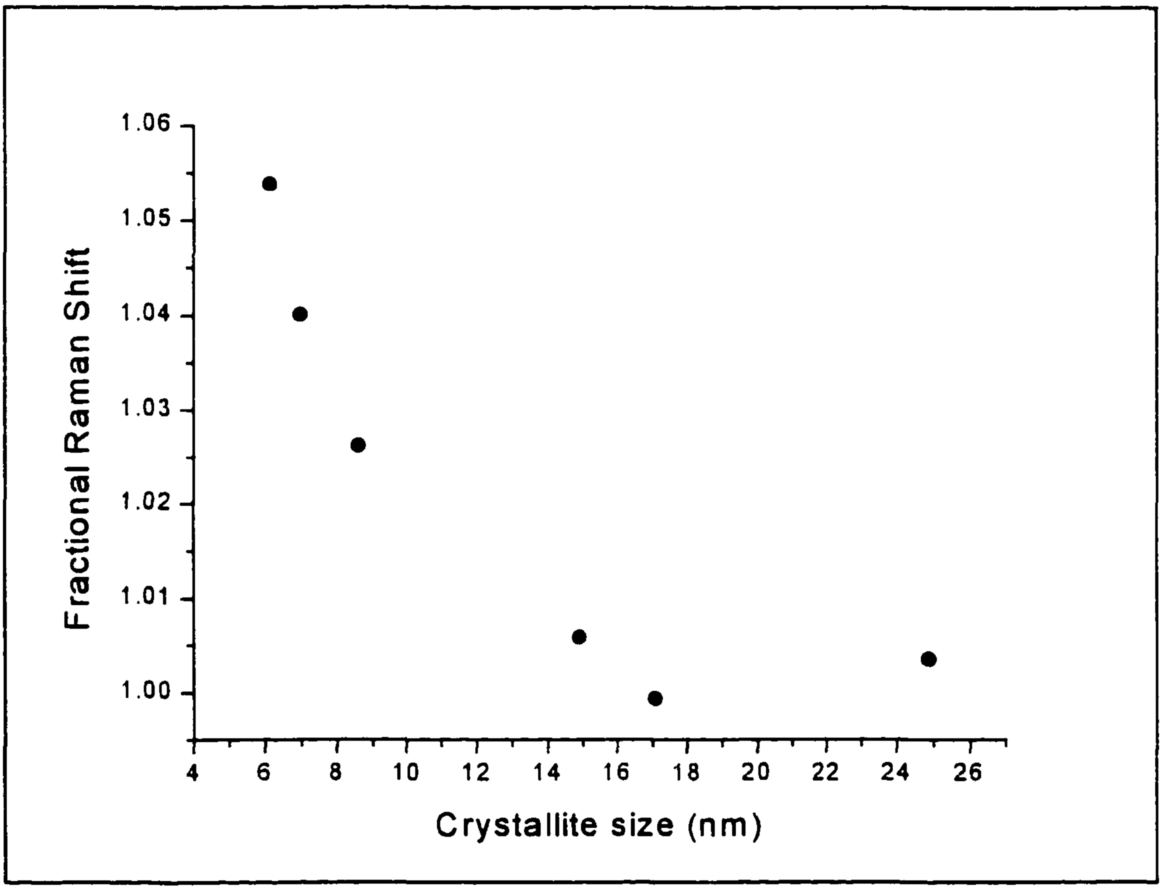

Figure 5-13 The fractional Raman shift versus crystallite size shows a blue-shift with increasing crystallite size.

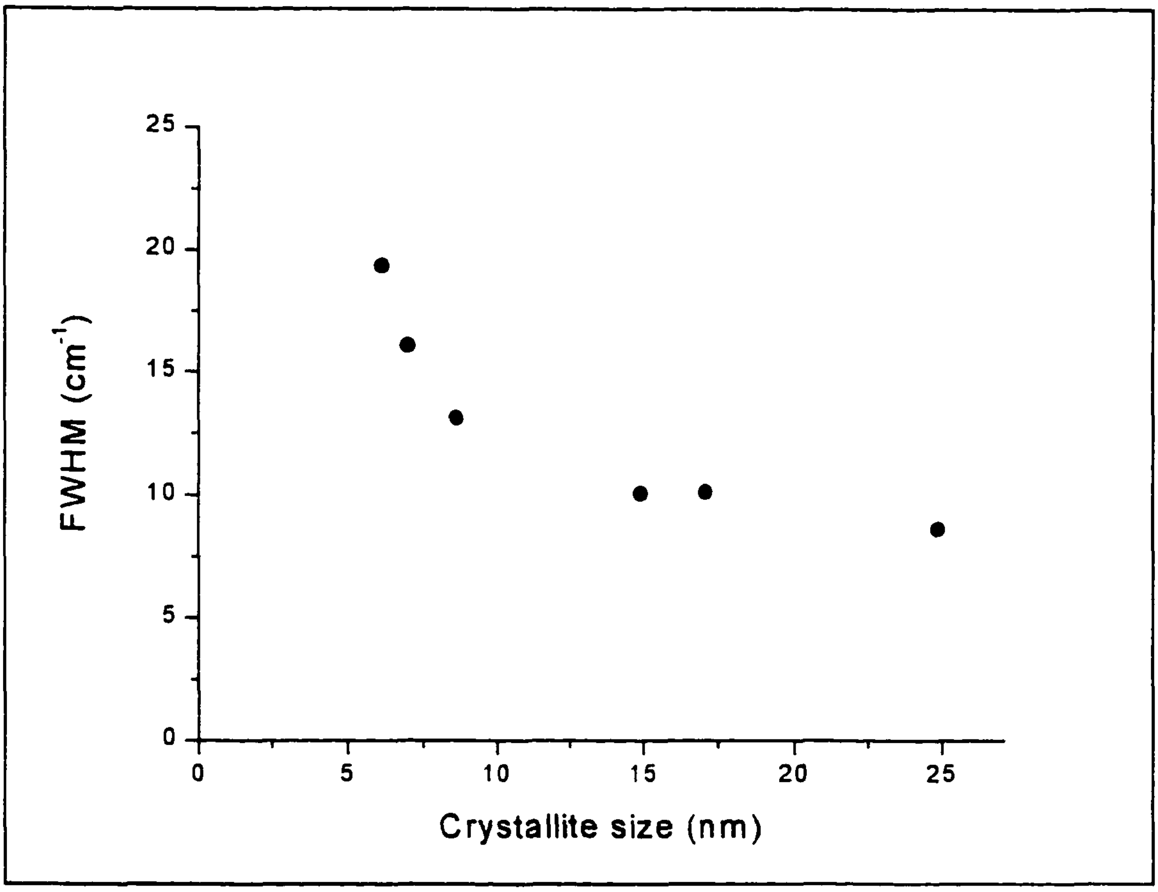

Figure 5-14 FWHM versus crystallite size for the E_g mode near 145.0cm^{-1}.

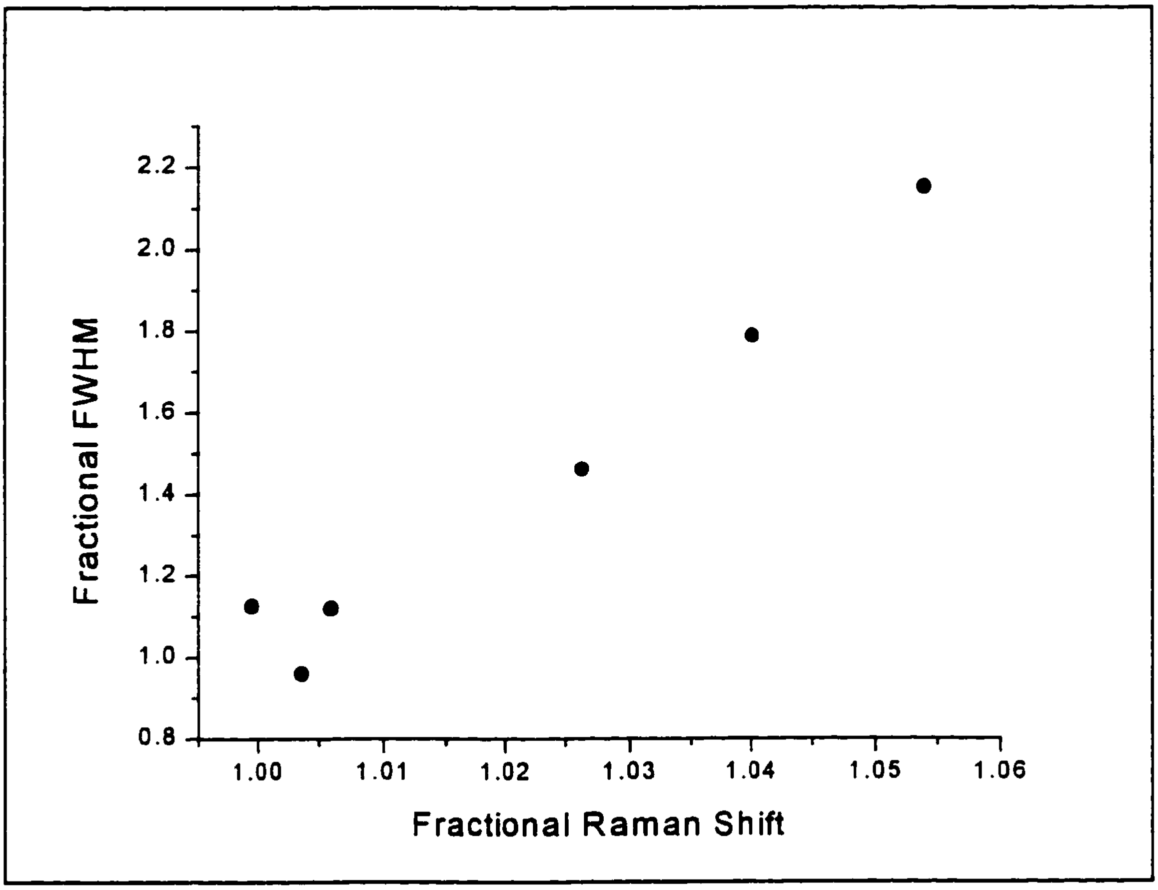

Figure 5-15 Fractional FWHM versus fractional Raman shift shows a roughly linear relationship

from the model. Spectra were simulated using the QVRM and an average unit cell of dimension a_L. Crystallite sizes from $1a_L$ to $1000a_L$ were considered in generating theoretical spectra. For each crystallite size, 600 points were calculated to generate a spectral peak and the results were imported into a graphical presentation program. The Raman shift was measured for the calculated spectra and compared with the theoretical single crystal value(Note: $1000a_L$ was considered to be a single crystal, in fact using anything larger than this produced identical results), and the FWHM of the peak were measured. For all theoretical calculations, a value of $9cm^{-1}$ was used as the value for Γ_0, the single crystal FWHM. The phonon dispersion curve also figures prominently in the calculation of Raman line shape. Some ab initio calculations have been done to estimate the anatase phonon dispersion and for the 145 cm^{-1} E_g peak the phonon mode is similar to that of the rutile mode Γ_{3+}[48]. Examining the phonon dispersion curve originating at 142 cm^{-1} for rutile, we see that it has a positive dispersion of about 80%.

In Figure 5-16, we compare the curve generated by a crystallite of size $6a_L$ and one of size $10a_L$. The peak for the larger crystallite is much sharper(smaller FWHM) and is offset toward lower energy. This is precisely as observed for the spectra of two different size crystallites(Figure 5-12). It is important to note that the unit cell size, a_L, has not been fixed in the calculations but since the actual anatase crystal unit cell is 3.78Åx3.78Åx9.50Å, we might expect that a_L would be an "effective" unit cell size between 3.78Å and 9.50Å.

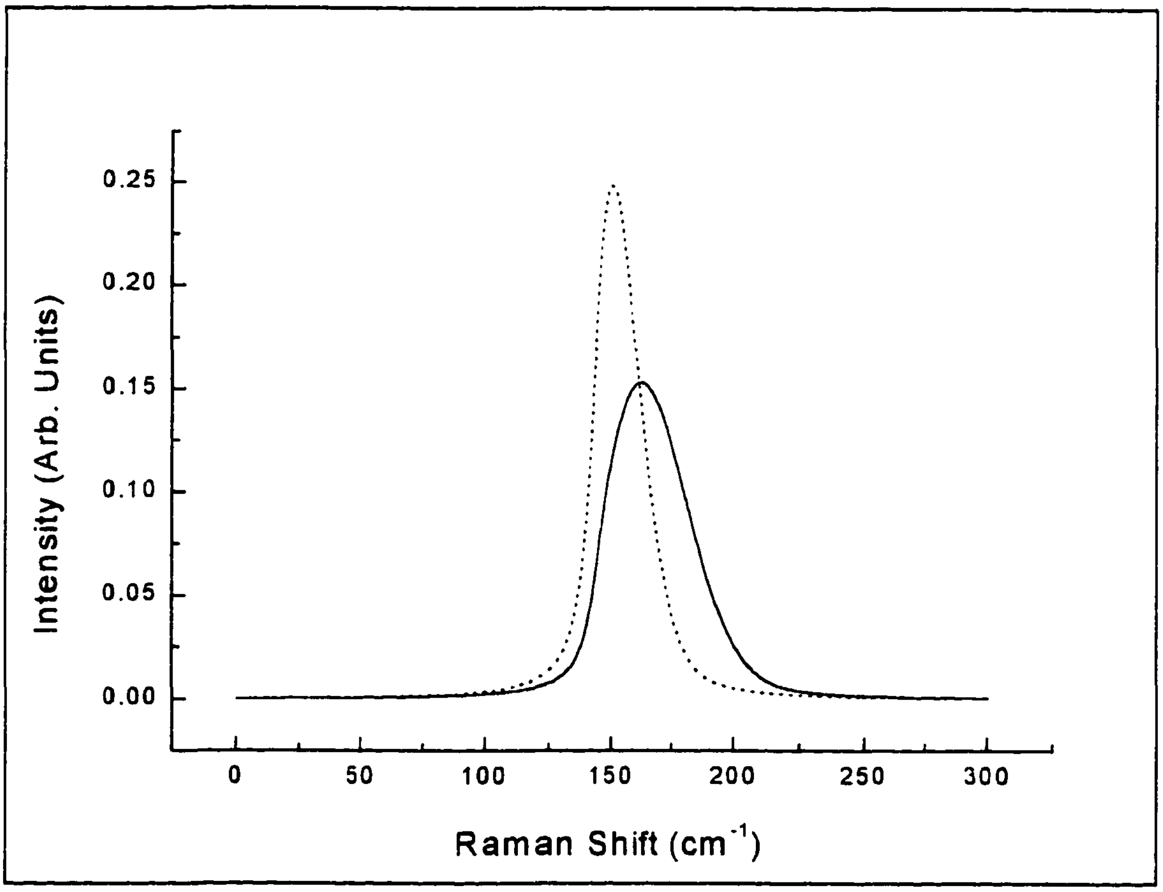

Figure 5-16 Comparison of the calculated Raman 145.0cm^{-1} E_g peak for a 6a_L (solid line) crystallite and 10a_L (dotted line) crystallite shows a blue-shift of the peak and a high energy asymmetric broadening exactly as seen experimentally.

The intensity and broadening follow the experimental results. The peak shift and broadening are interrelated through the particle size distribution[49]. The particle distribution of the TiO_2 aerogels was previously described[30]. The nano-crystallites size distribution is approximately a narrow gaussian. Figures 5-17 shows that for a mean crystallite size of only $2a_L$ there is a noticeable shift in peak position as well as broadening with increasing width of the gaussian distribution, σ. Figure 5-18 shows that for a mean crystallite size of $5a_L$, the effect of the size distribution is also a slight red-shift and broadening of the peak as well. These curves were simulated with the same positive dispersion as the one described previously.

There is a clear shift toward the red with widening of the particle distribution. Similar to the conclusion in Doss and Zallen[41], the widening of the distribution and the q relaxation mechanism shift the spectra in opposite direction. However, the shift due to the widening of the distribution is considerably smaller compared to that of the q relaxation mechanism. This difference was used by Doss and Zallen to suggest that the small shift in the sol-gel phase corresponds to a wide particle size distribution while the corresponding changes in the solid correspond mainly to the q-relaxation mechanism. It is obvious that both mechanisms contribute throughout, however, the uncertainty with the dispersion precludes the deconvolution of the two effects. Figures 5-19 and 5-20 summarize the results: Figure 5-19 shows the theoretical FWHM and position of the 142 peak superimposed with the experimental data, as a function (crystallite size)$^{-1}$. While the experimental crystallite size was determined from X-ray crystallography, the theoretical

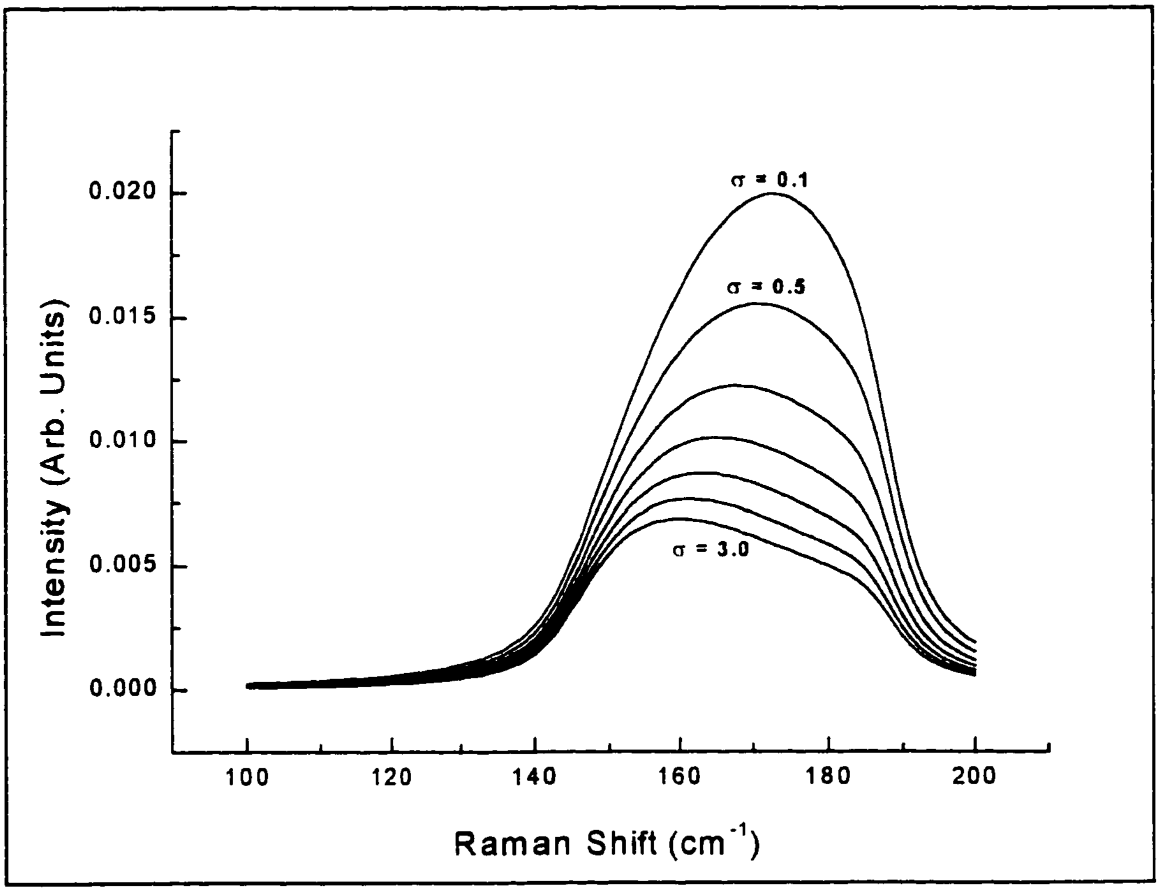

Figure 5-17 The effect of size distribution is a red-shift in the peak position and a broadening of the peak, with increasing width of the distribution. The mean crystallite size is $2a_L$, and σ is also expressed in terms of a_L.

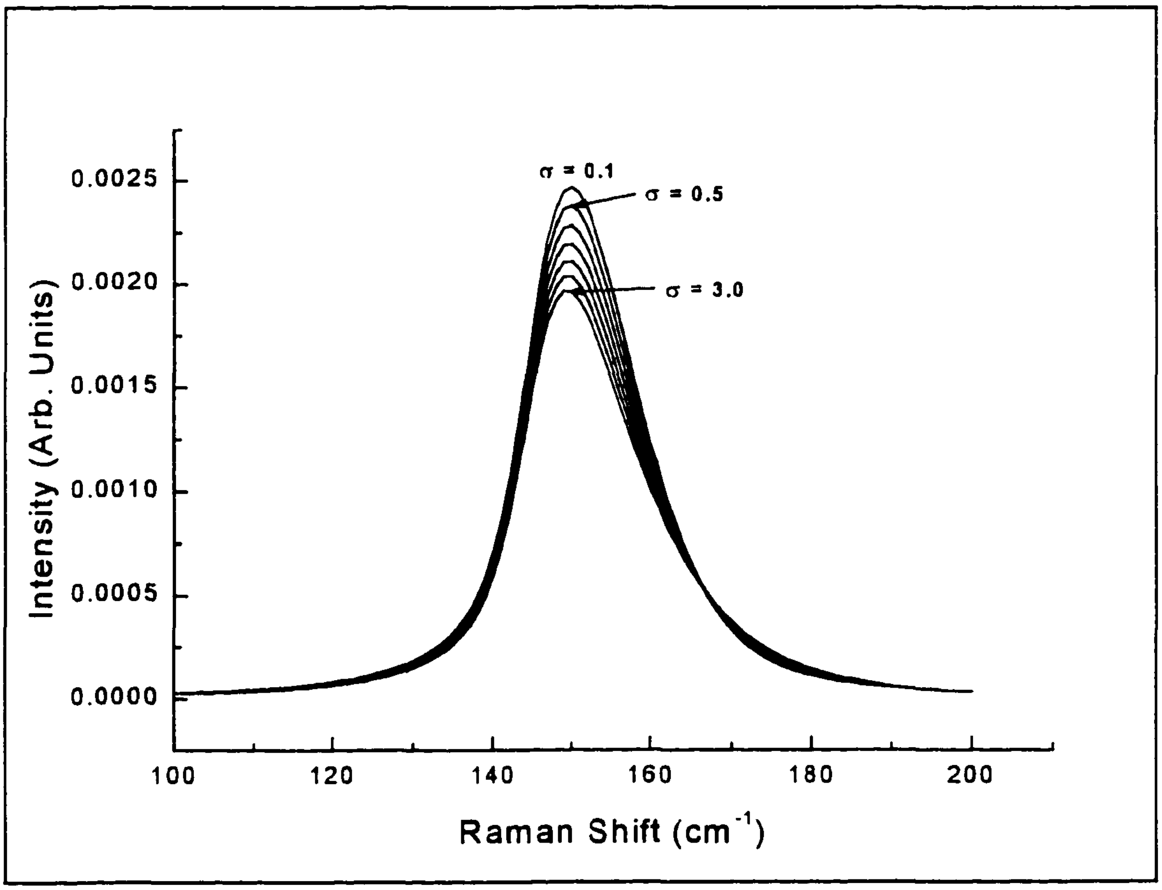

Figure 5-18 There is a small red-shift and broadening for increasing σ with a mean crystallite size of $5a_L$. Note that σ is in units of a_L.

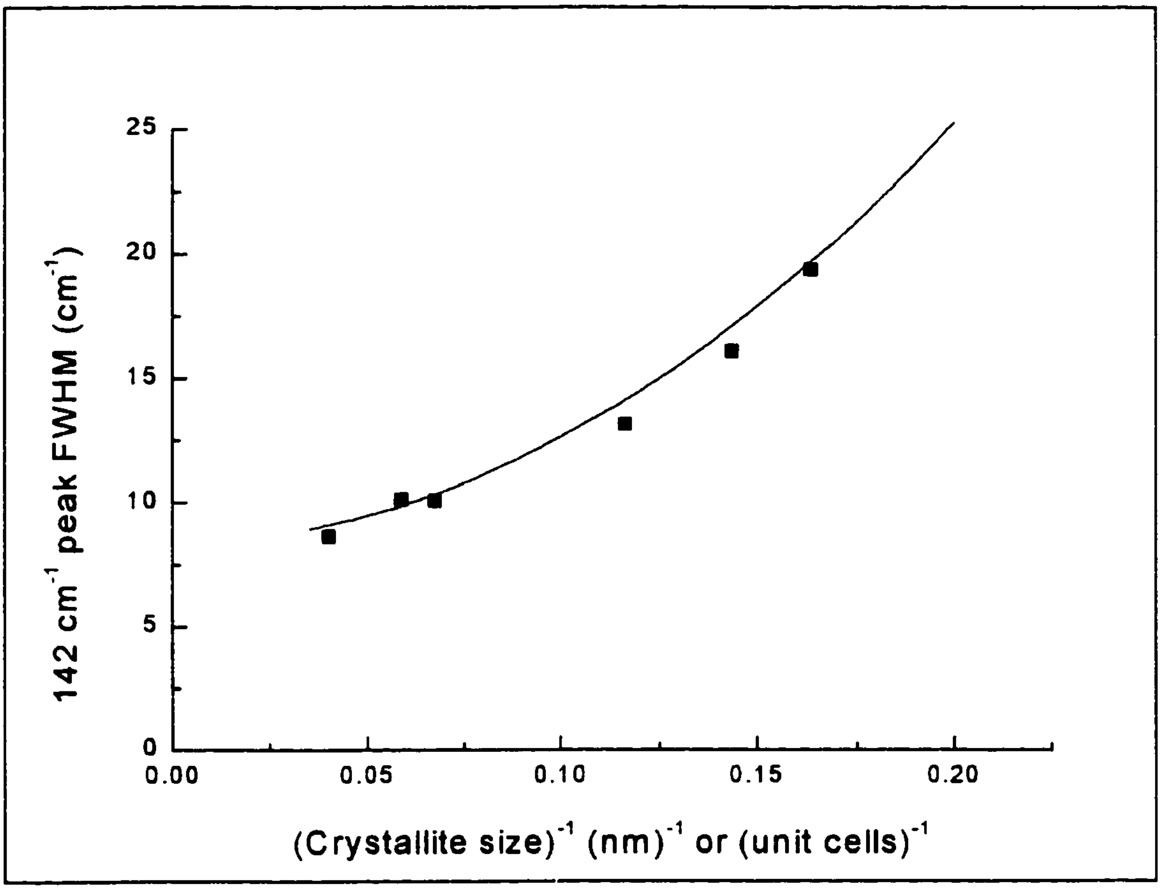

Figure 5-19 The FWHM follows a scaling law when compared to the (crystallite size)$^{-1}$. Fitting (solid line) to the experiment data(■) fixed the value of a_L at 5.55Å.

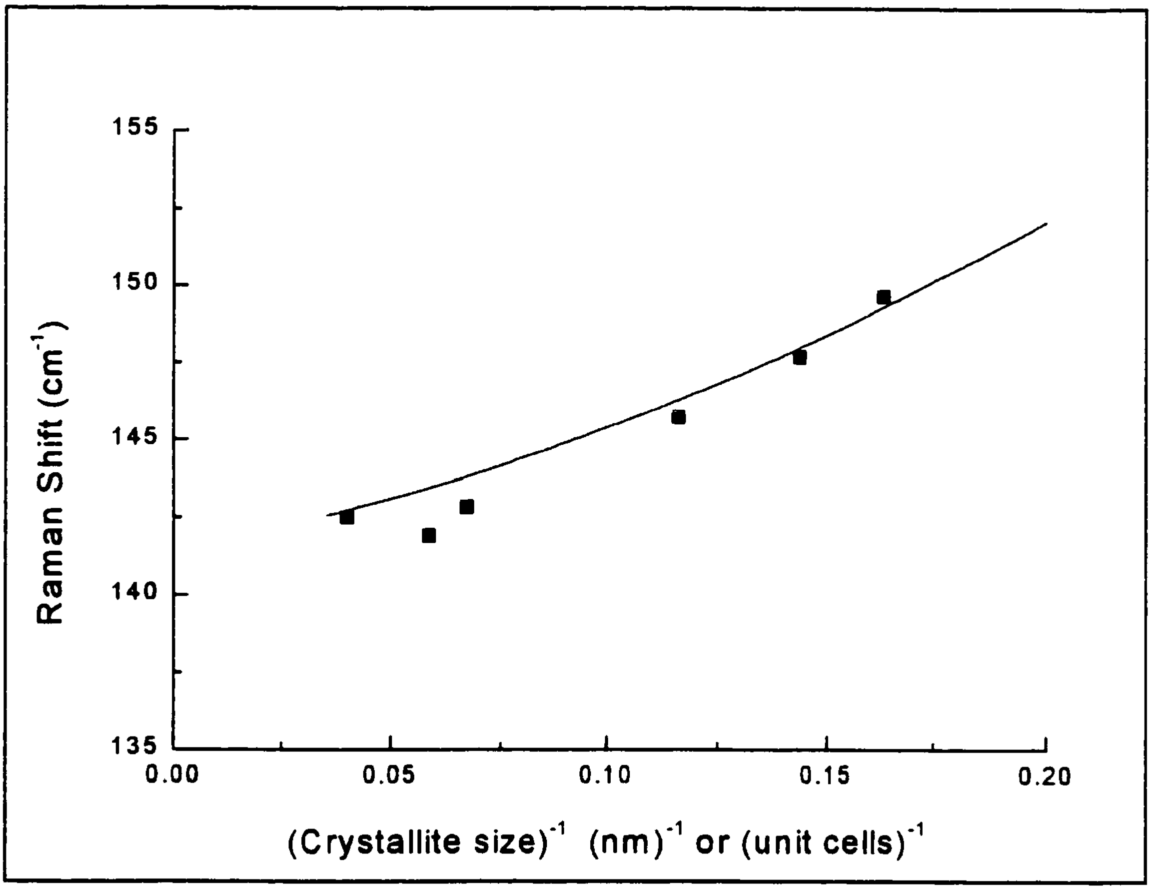

Figure 5-20 The Raman Shift also follows a scaling law when compared to the (crystallite size)$^{-1}$. There are no adjustable parameters in the fit(solid line).

fits were calculated in terms of multiples of unit cell size. By fitting the theoretical curve with the experimental data, the "effective" unit cell size, a_L, is fixed. The data in Figure 5-20 are drawn with the value of a_L obtained from the first fit and no other adjustable parameters. As can be seen, the fit is remarkably good. The "effective" unit cell size produced in this manner yielded a value of 5.55Å for the 81% positive dispersion. This fits remarkably well with our prediction of an average value for the crystal unit cell somewhere between 3.78Å and 9.50Å. The results from Figure 5-19 also were fit to a scaling law (Equation 5-10):

$$\Gamma = k_2\left(\frac{1}{L^{\alpha}}\right) + \Gamma_0 \qquad \textbf{(5-10)}$$

Where Γ is the linewidth, and Γ_0 is the line width of a single crystal. The line width

$$\Delta\upsilon = k_1\left(\frac{1}{L^{\alpha}}\right) \qquad \textbf{(5-11)}$$

(Figure 5-20) also seems to follow a scaling law(Equation 5-11). Where $\Delta\nu$ is the peak shift from the single crystal location, and L is the crystallite size. The parameter α is a scaling parameter that has been related to the network structure[50]. Materials with a layered structure such as graphite and boehmite have been shown to have ($\alpha \approx 1$)[51], while for covalently bonded semiconductors such as Si and GaAs ($\alpha \approx 1.5$)[41]. From Figure 5-19, α is calculated to be 1.55. This seems to agree with known semiconductor values.

Raman Scattering in liquids

In the case of a liquid, or non single crystals, Raman scattering occurs when the polarization of the molecules is non-zero. The polarization vector can be expanded in a Taylor series about the equilibrium value:

$$\vec{p} = \vec{p}_0 + (\vec{r} - \vec{r}_0)\vec{\nabla} \cdot \vec{p} + \ldots \tag{5-12}$$

Then the Raman scattering strength will depend on the change in polarization between some initial and final state (since $\langle f | \vec{p}_0 | i \rangle = 0$), i.e.

$$\langle f | (\vec{r} - \vec{r}_0)\vec{\nabla} \cdot \vec{p} | i \rangle \tag{5-13}$$

The difference between molecular scattering and single crystal scattering being that long range order is no longer necessary since periodicity is not invoked. The Ar$^+$-ion laser was used as an excitation source, but the scattered light was taken at 90° to the incoming laser light (Figure 5-21). In this configuration, a single instead of triple monochromator is used, which means that the spectra background is significantly larger. The sol was prepared as described in Chapter 3, then within 5 minutes of complete mixing, it was placed in a quartz cuvette for measurement. Raman spectra were recorded at approximately 5min intervals. The sol spectra is dominated by the Ethanol component, which has several prominent peaks in the range of interest (Figure 5-22). Subtraction of the Ethanol spectra was done to obtain Raman spectra for the structure in the sol at 5 minutes (Figure 5-23). The spectra can be seen to change during the sol evolution, until gelation, where the spectra are nearly constant. Gelation occurred after about 60 minutes (Figure 5-24). Because we believe the changes in the sol to be the growth of the titanium

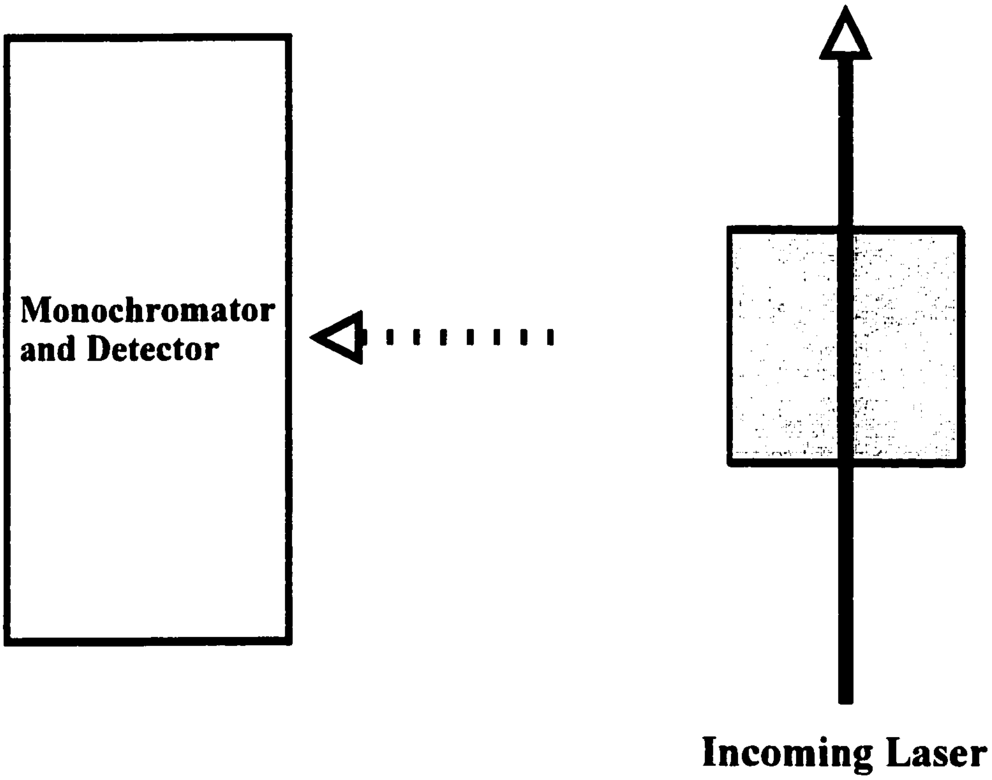

Figure 5-21 The experimental setup for sol and gel samples collects light at 90° to the incident laser light.

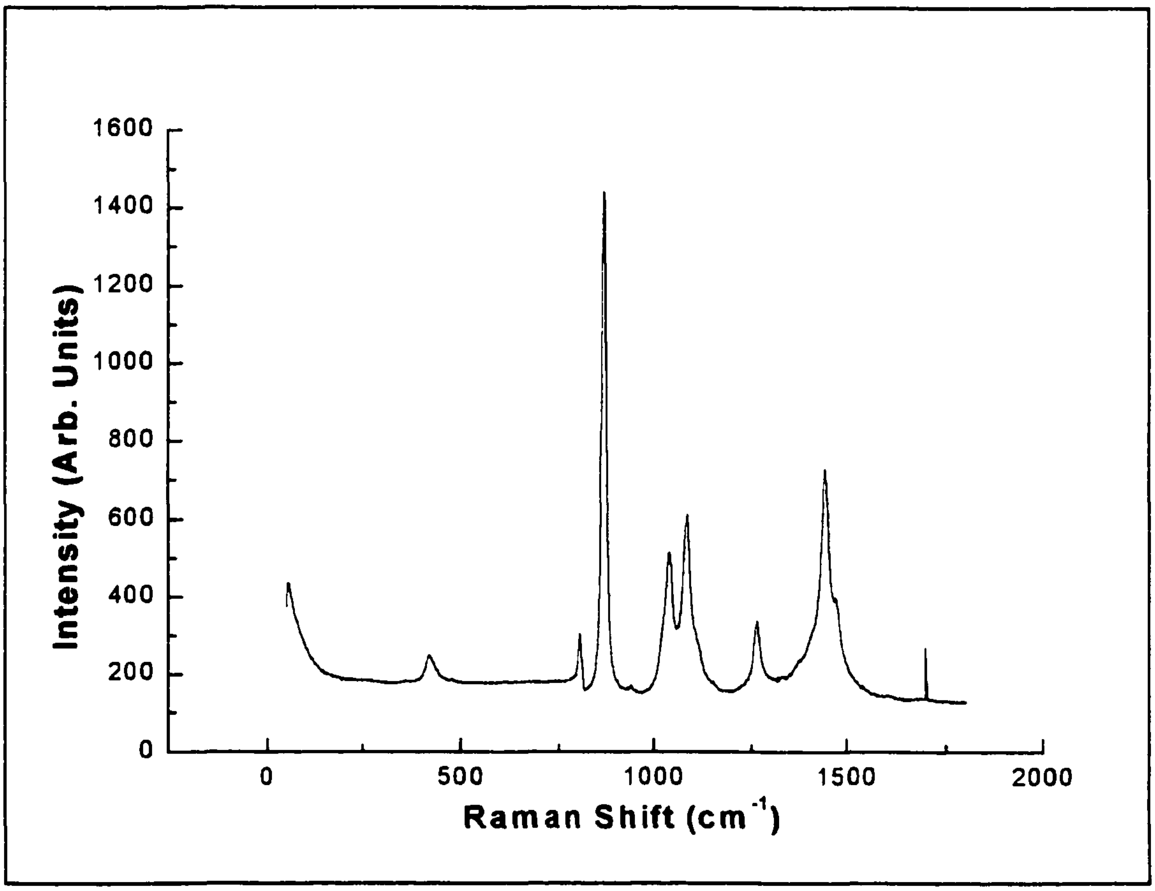

Figure 5-22 The Raman spectra for ethanol has significant peaks overlapping the spectra of anatase in the range 100cm^{-1} to 900cm^{-1}.

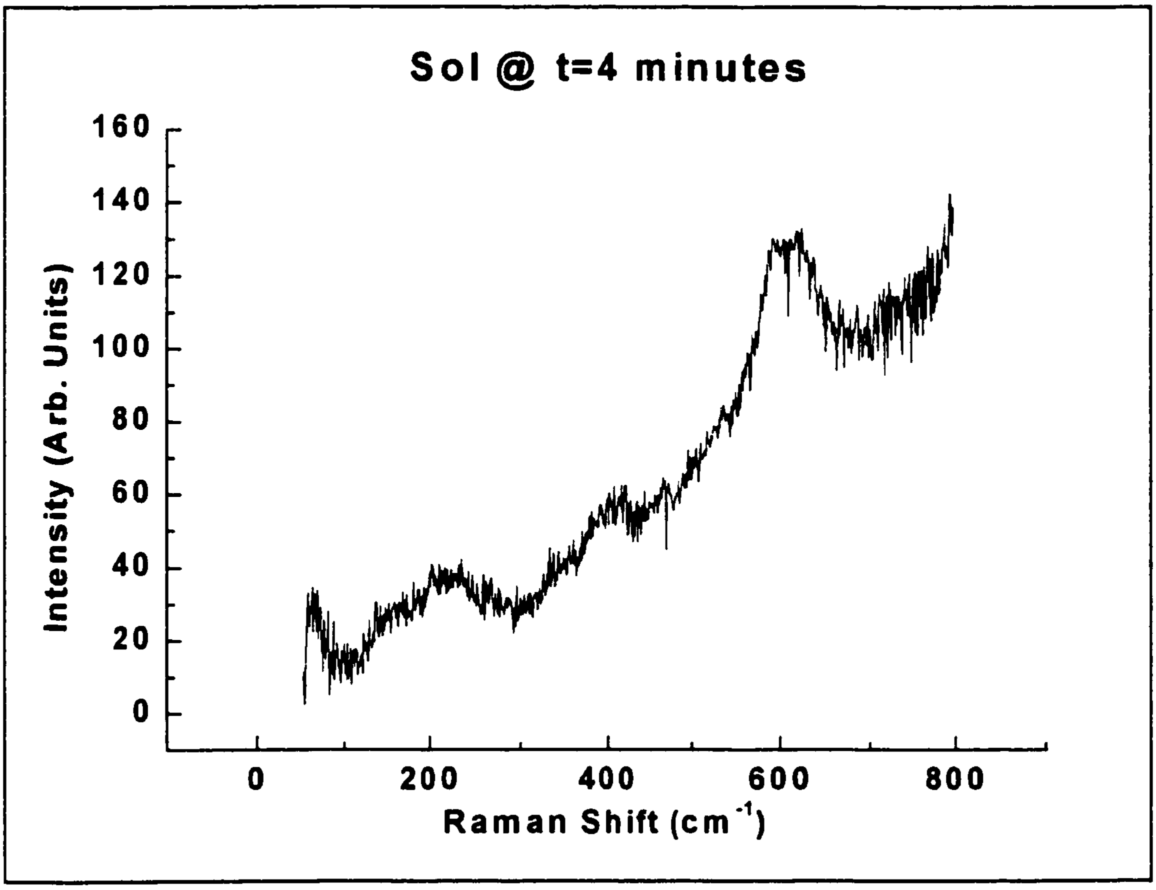

Figure 5-23 The Raman spectra for the sol at four minutes shows a noticeable peak at about 600cm^{-1} but has a very large background incline. This spectra was obtained by first subtracting the spectra of ethanol from the raw sol spectra.

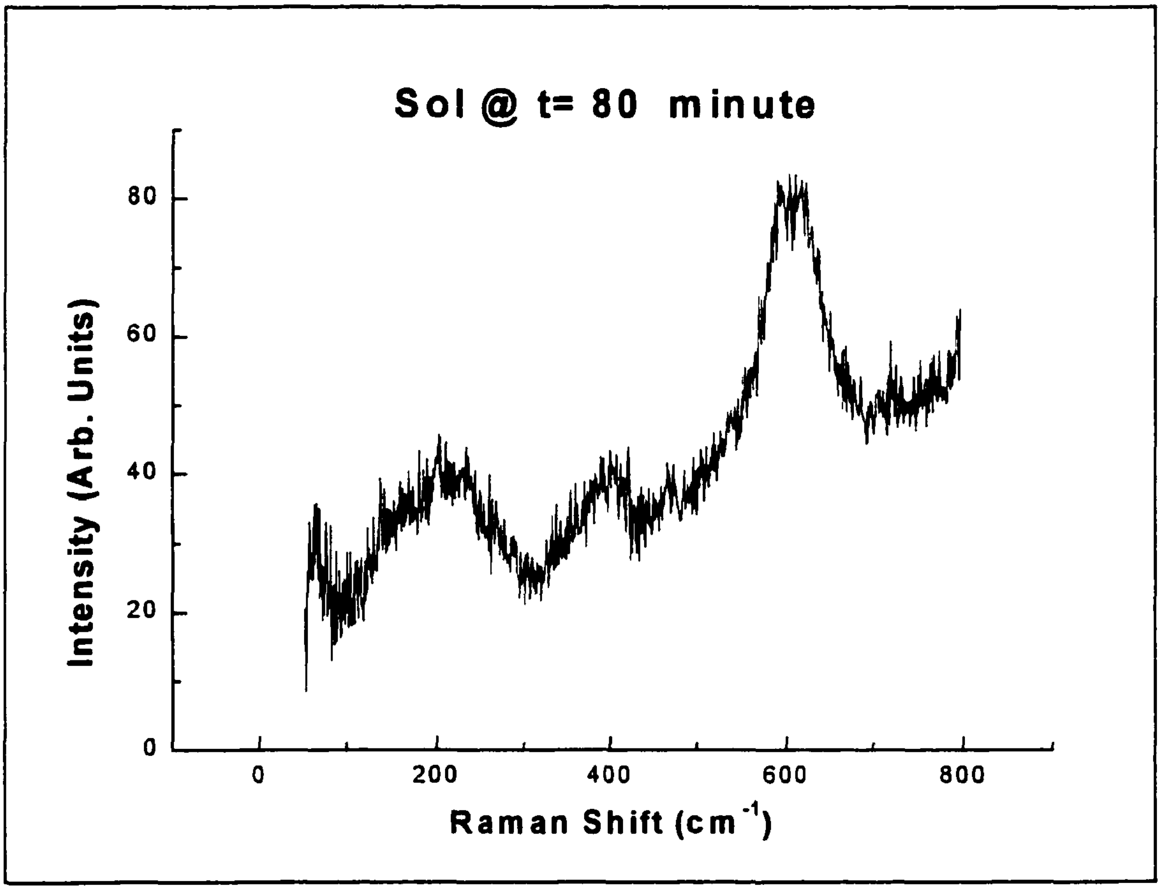

Figure 5-24 The Raman spectra for the sol at 80 minutes has gelled. There are visible peaks at 200cm^{-1} and 600cm^{-1}. Again this spectra was obtained after subtracting the ethanol spectra.

dioxide structure, it seems reasonable to compare the Raman spectra for the new sol and the gel as first formed. The spectra at 5 minutes was subtracted from the spectra at 60 minutes and it is possible to see the original strong peak at 600cm^{-1} as well as a weak but perceptible peak at around 200cm^{-1} (Figure 5-25). Comparing the spectra of the gel at 80 minutes with the gel at 275 minutes, there are slight changes in the spectra but a slight enhancement of the 200cm^{-1} peak (Figure 5-26). In experiments with SiO_2-TiO_2 sol-gel, Condone et al associated the peak at 600cm^{-1} with sixfold coordination Ti-O bonding[52]. They do not mention the 200cm^{-1} peak. Using a simplistic interpretation that the 200cm^{-1} is the Raman shifted 145.0cm^{-1} peak and using the scaling law for Raman shift (Equation 5-10) for the peak location, the gel appears to have an average anatase crystallite size of about 1.5Å. The crystallite size as determined by the width of the peak would set the size to be about the same. Future work could certainly focus on clarifying the identity and interpretation of the sol-gel spectra.

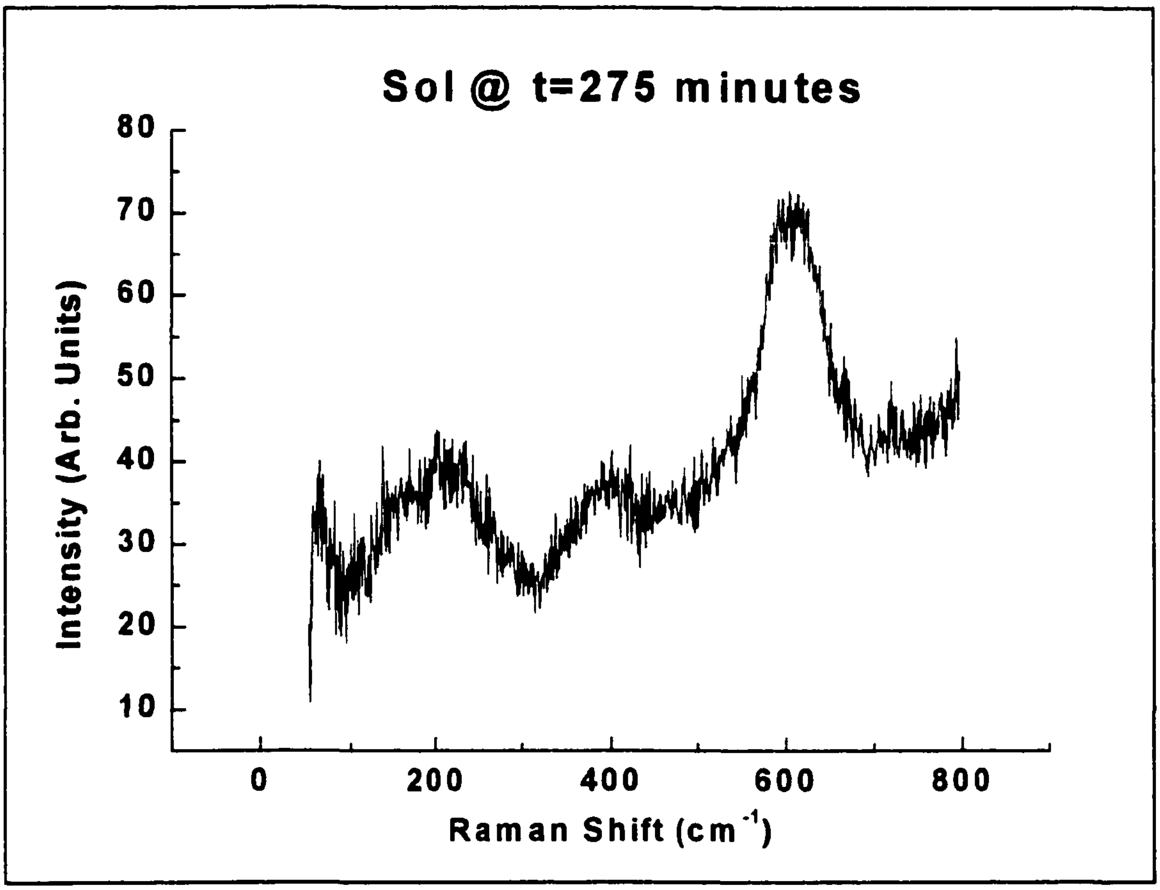

Figure 5-25 The Raman spectra for the sol at 275 minutes has gelled. There are visible peaks at 200cm^{-1} and 600cm^{-1}. Again this spectra was obtained after subtracting the ethanol spectra.

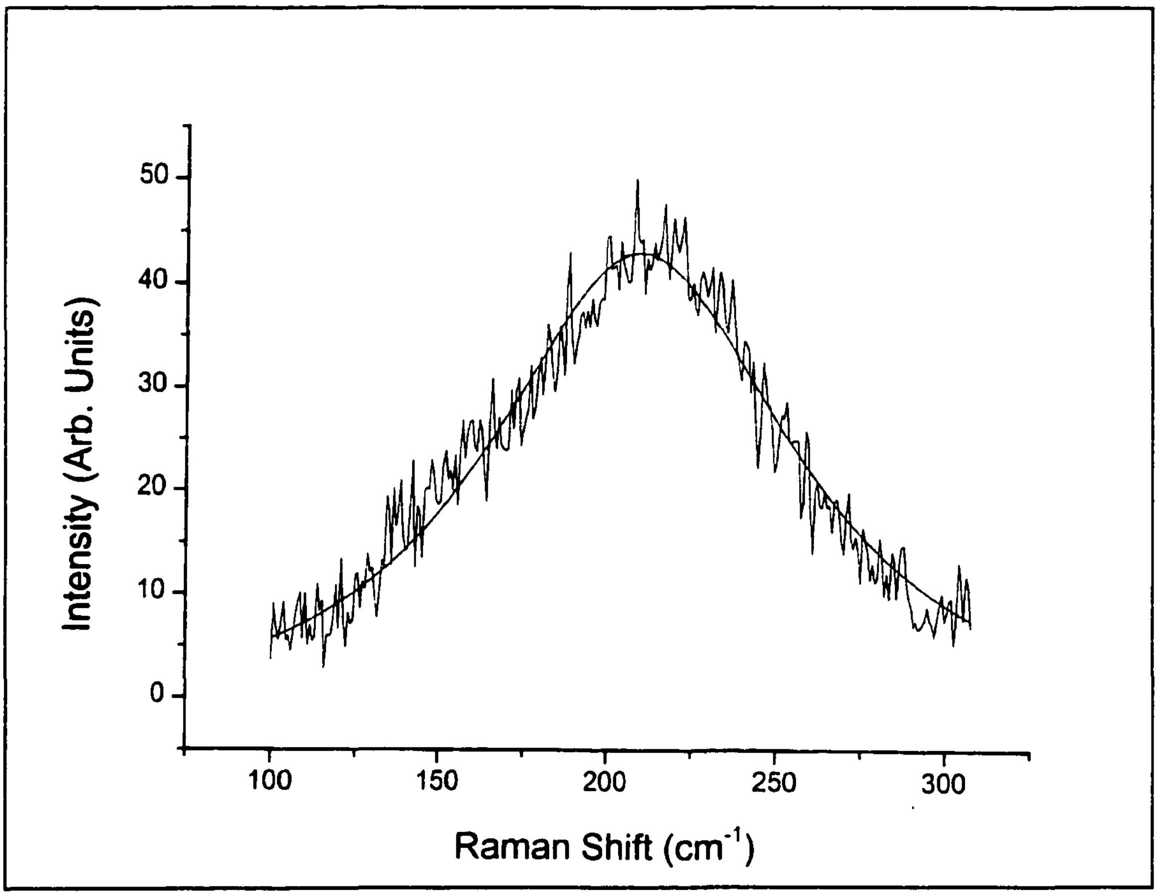

Figure 5-26 Careful measurement of the 200cm^{-1} peak of the gel at 275 minutes indicates a crystallite size of about 1.5nm.

Chapter 6 - Extended X-ray Absorption Fine Structure

EXAFS Background

All atomic elements can be identified by the absorption and emission of radiation. In particular, the onset of absorption of x-ray radiation by core electrons is described in quantum physics by the initial level of the ionized electron, i.e. the "K-edge", "L-Edge", "M-Edge" etc. The edge nomenclature stems from the names for the core shells as given by Sommerfeld (Figure 6-1). The absorption lines correspond to the energy necessary to lift an electron from it's core state to a continuum state. The emission lines have been named K radiation if they result from an electron making a transition from a continuum state to the K energy level. In a mono-atomic system, the absorption edge is sharply defined and it drops off as the atomic cross-section; there are essentially no oscillations in the absorption curve. As soon as the system becomes more complex, and the excited atom has nearest neighbors (Figure 6-2), oscillations begin to appear in the high energy side of the absorption peak. Analysis of the EXAFS spectra can yield the nearest neighbor distance, as well as the number and type of nearest neighbors. This non-invasive technique was already been used to look at "fine" particles of anatase (~35nm)[53] and sol-gel derived xerogels. Kozlowski et al. examined the EXAFS spectra for single crystal and particulate anatase and found remarkable similarities in the spectra with a few detectable differences (Figure 6-3).

In Figure 6-3, χ is the modulation of the absorption which sits on top of the K-edge

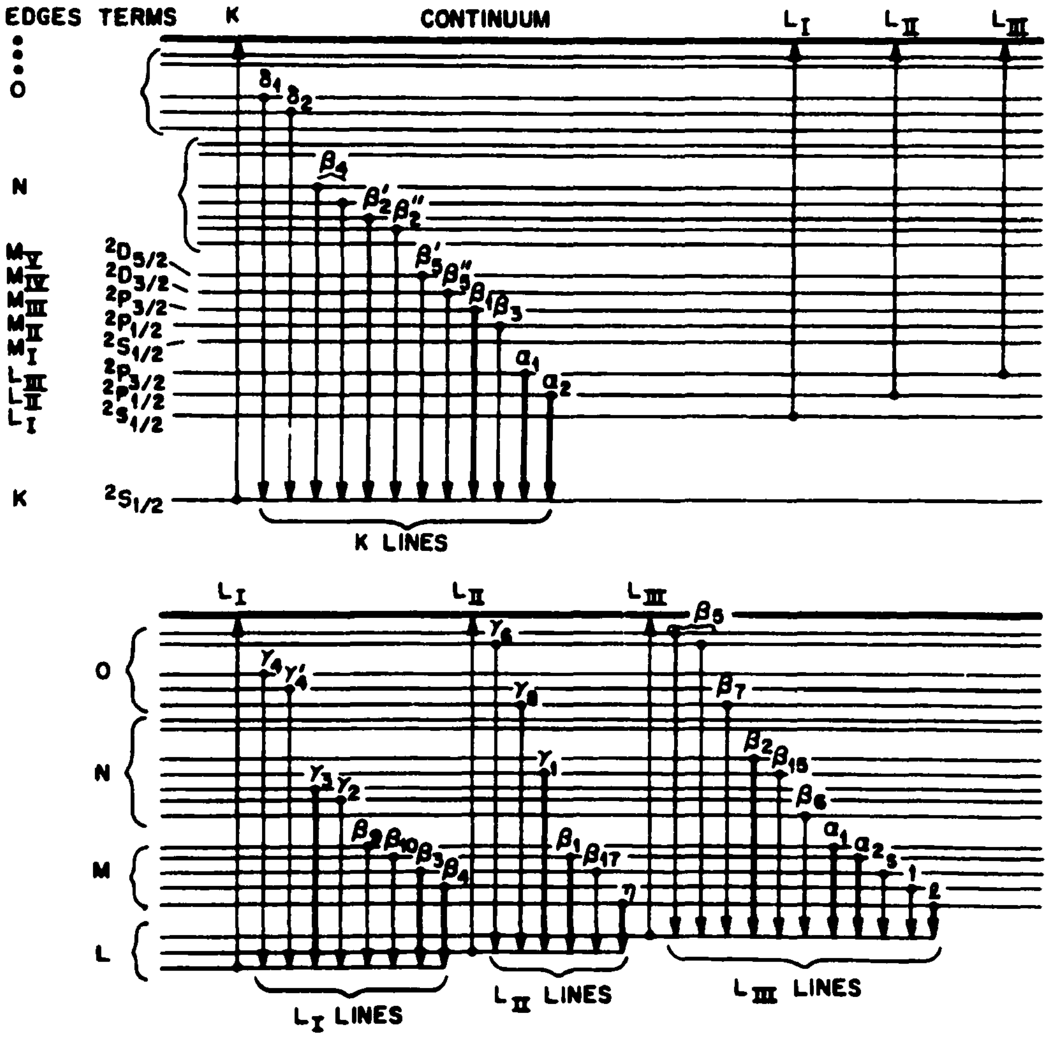

Fig. 1.5. Some of the X-ray absorption edges and the corresponding characteristic emission lines. The notation for the shells is that of Sommerfeld (K, L_I, L_{II}, L_{III}, etc.) and that for the transitions is that of Siegbahn (K_{α_1}, K_{α_2}, K_{β_1}, etc.).

Figure 6-1 X-ray emission and absorption lines as defined by Sommerfeld correspond to transitions between core electron energy levels and the continuum state (Taken from reference 54).

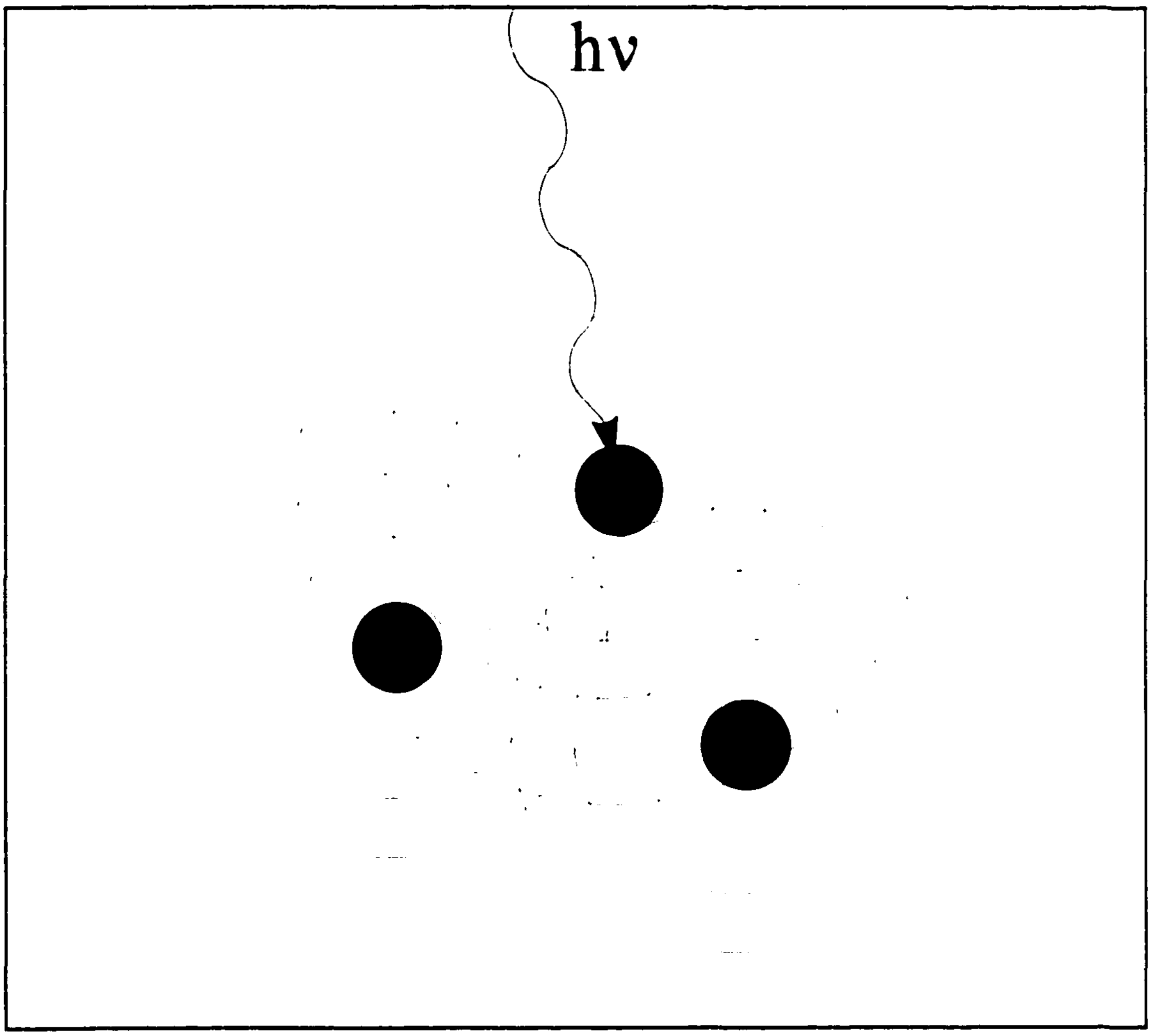

Figure 6-2 The incoming photon excites a core electron, and the photoelectron will interfere with neighboring atoms.

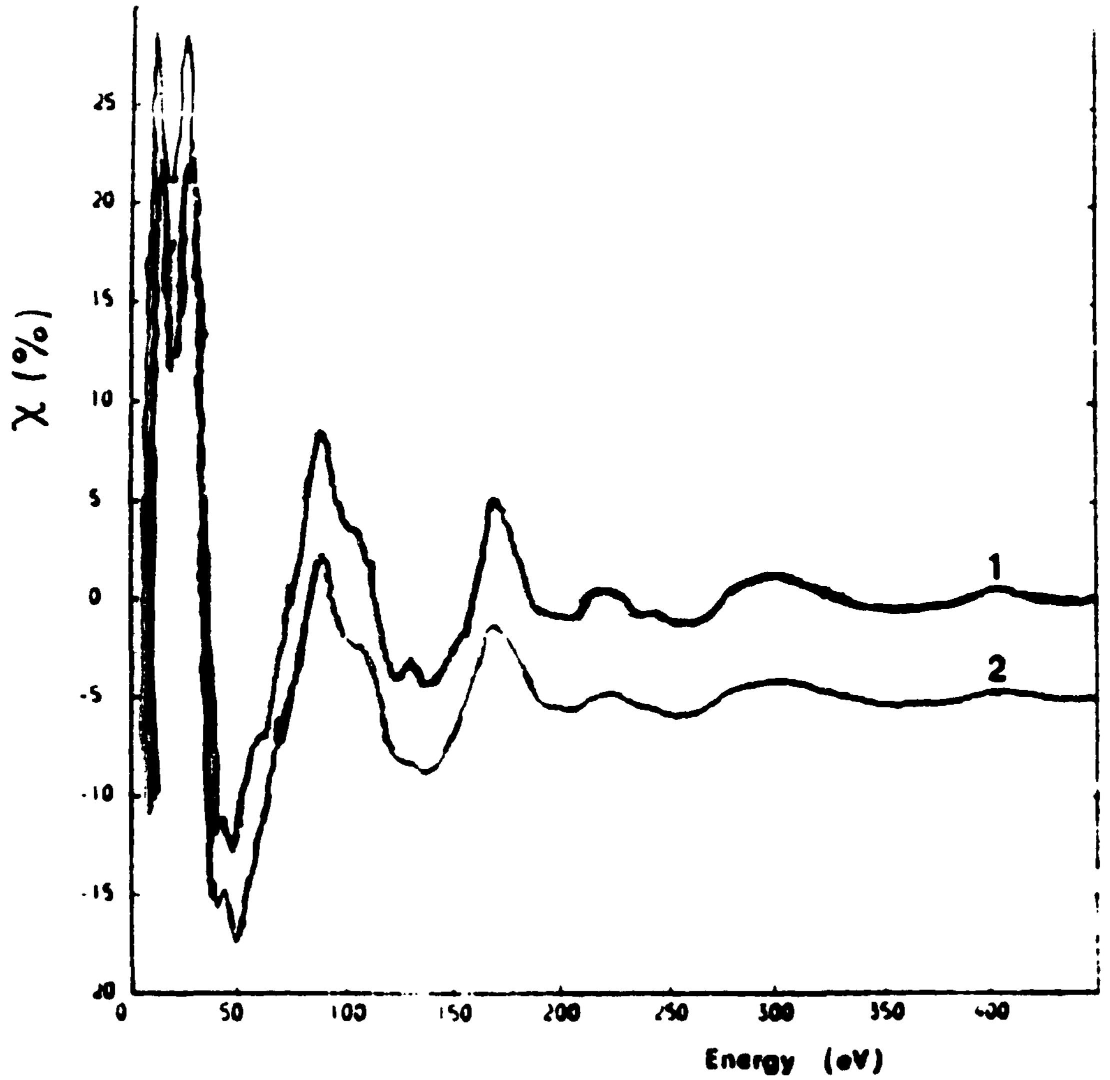

Figure 1. EXAFS structure, χ(*k*), vs. the X-ray photon energy (eV) for crystalline (1) and fine-size (2) anatase.

Figure 6-3 EXAFS spectra for single crystal (1) and "fine-size" particulate anatase (2) (Taken from reference 53).

step for titanium.The K-edge of titanium, E_0, has been measured in anatase, rutile and titanium metal as 4983.1eV, 4983.8eV, and 4964.5eV[54]. With energy greater than E_0, the ionized electron has excess momentum (Equation 6-1) which causes it to scatter from neighboring atoms, resulting in an enhanced coupling between the incoming radiation and the electron (Equation 6-2).

$$\begin{gathered}\frac{\hbar^2 k^2}{2m} = h\nu - E_0 \\ k = \frac{2\pi}{\lambda} = \frac{1}{\hbar}\sqrt{2m(h\nu - E_0)}\end{gathered} \tag{6-1}$$

$$\left(\langle f_0| + \langle f'| + \langle f''|\right)\vec{\varepsilon} \cdot \vec{x}|i\rangle \tag{6-2}$$

In equation 6-2, $|i\rangle$ refers to the initial state, while $\langle f_0|$ is the free state and $\langle f'|$ and $\langle f''|$ are two scattering terms. The final state of the electron will be the spherically symmetric scattered state, as well as reflection terms from nearby atoms. The reflection terms mean that there will be some interference of the outgoing wave and so the absorption which is proportional to the transition strength (Equation 6-2) will oscillate. The shape of the EXAFS spectrum is dependent on the number of nearest neighbors, as well as the distance from nearest neighbor atoms. Figure 6-4[55] shows the general effect of changing either the bond length or the number of nearest neighbors. By increasing the distance to nearest neighbor atoms, the number of oscillations increases, because the phase difference between the outgoing

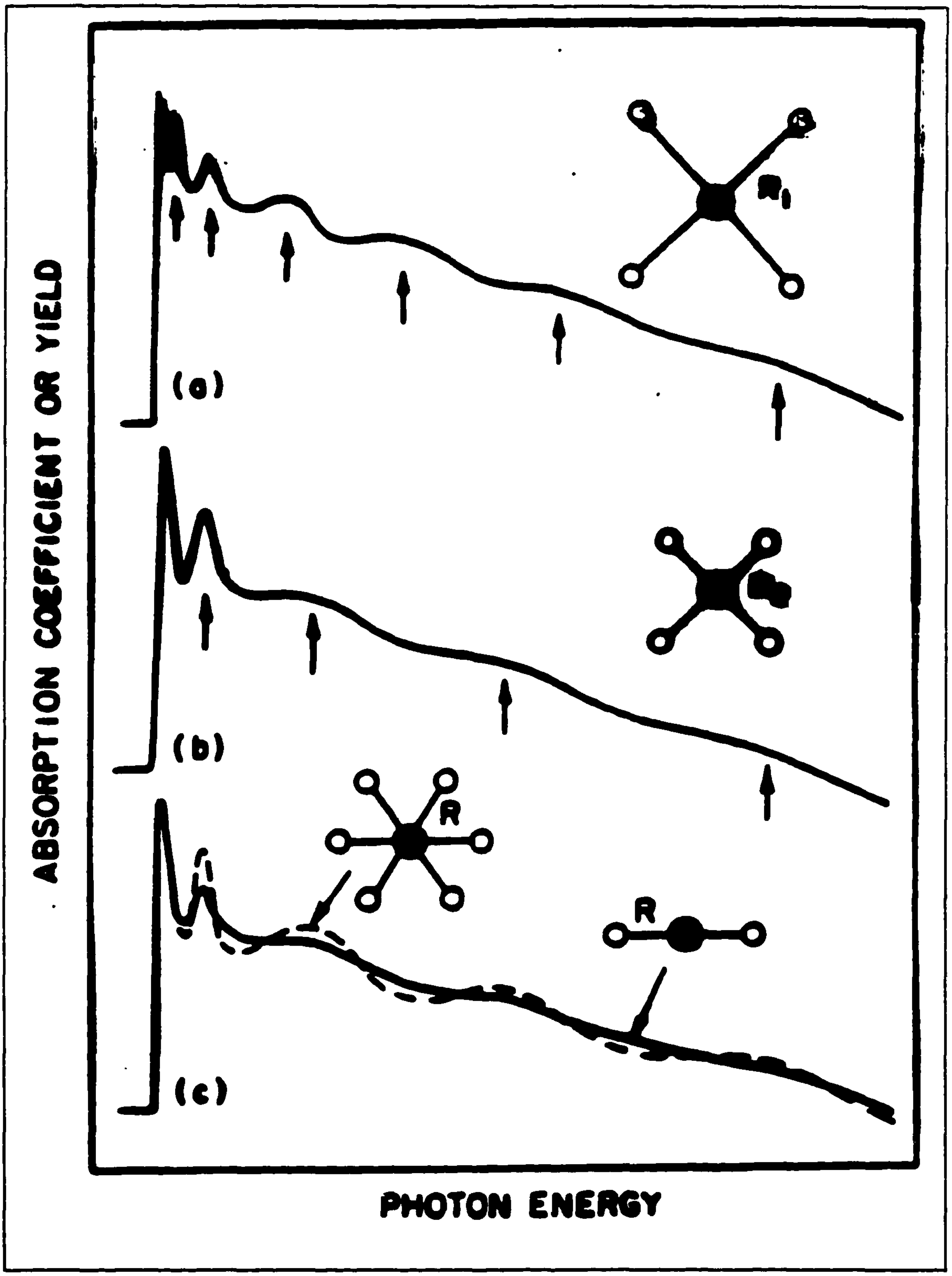

Figure 6-4 Oscillations are closer together for a longer nearest neighbor distance (a) than for a shorter nearest neighbor distance (b).Increasing the number of nearest neighbors results in an increase in oscillation strength (c) (Taken from reference 55).

and reflected waves will be larger than those with a shorter nearest neighbor distance. For a given nearest neighbor distance, the oscillation strength will increase with more nearest neighbors. This oscillation results from scattering of the excited electron off neighboring atoms. There is a reflection and an interference effect that can be correlated with the number of nearest neighbor atoms. The resulting absorption curve with tail can be analyzed to determine the number of nearest neighbors and by further absorption measurements, the identity of neighboring atoms.

Objective

By measuring the EXAFS spectrum of the sol-gel, the local structure around the Ti atom can be elucidated. It seems reasonable to expect that when the sol is first made, it's structure will be similar to the TIP precursor. As the sol-gel begins to condense and polymerize, the structure should become more ordered, perhaps resembling anatase crystal. By analyzing the EXAFS spectra with both TIP and anatase as standards, it should be possible to see the sol-gel evolution.

Experimental Design

In practice, the EXAFS spectra can be measured by recording the absorption or transmission of x-ray radiation by a material. Titanium has an absorption cross-section of 86.8cm^2/g[56] at about 4990 eV and for the sol-gel experiments synchrotron radiation first passed through a monochromator which was then used to scan across an energy range from slightly below the Ti K-edge to about 800eV above the K-edge. Experiments were carried out at Brookhaven National Labs, Synchrotron Light Source, beam line X6B, under the guidance of Professor Pedro Montano.

Before doing the sol-gel experiment, Ti-foil was used to calibrate the energy of the Ti K-edge, and titanium isopropoxide was measured as a test system. The sol-gel sample consisted of a 1:25:3.5:0.08 reactant ratio, and was placed in a sample cell consisting of an aluminum slide about 1.5mm thick with an approximately 1cm x 1cm square hole cut in the middle, with Mylar tape acting as the front and back walls of the cell. Samples were measured every one minute and 43 seconds, using a fast EXAFS acquisition program, from about five minutes after complete mixing through gelation. The spectrum for TIP was measured as a standard. A suitable data set for anatase TiO_2[57] was obtained from the Farel-Lytle database.

Reduction of the raw EXAFS spectra (Figure 6-5) was done using the program WINXAS[58]. WINXAS is a self-contained program for reduction of all types of x-ray data, but it also supports rudimentary fitting from known phases. First, a linear background term was subtracted from the raw data. Then the absorption step was normalized in the region of interest, 4965eV - 5416eV. The absorption fine-structure, $\chi(k)$, was then found by subtracting a smooth cubic spline fit to the absorption spectra. The spectra was then transformed into k-space by transforming the

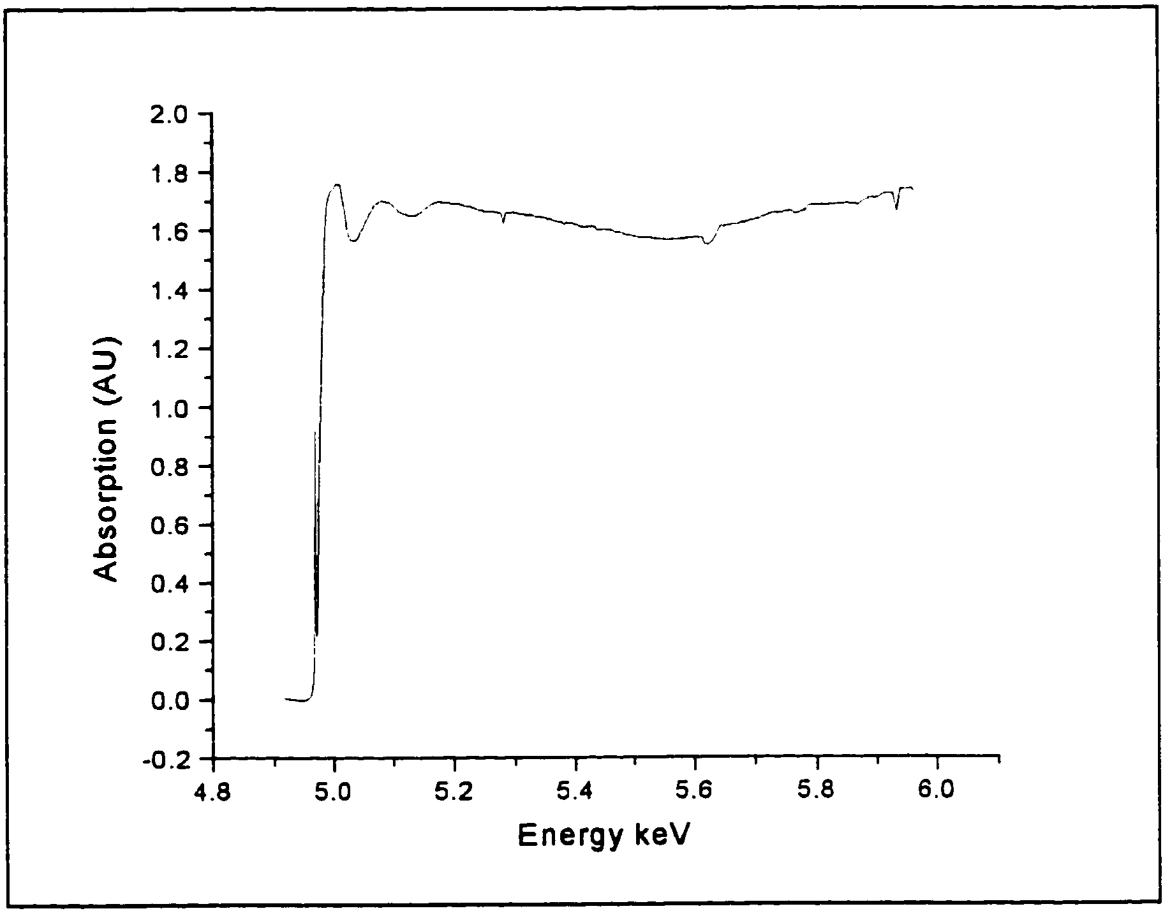

Figure 6-5 The EXAFS spectra for titanium isopropoxide is used as a standard for comparison with the sol Ti-O bond length.

energy according to Equation 6-1 (Figure 6-6). The spectra were then renormalized by multiplying by k^3 and the result is then Fourier transformed (Figure 6-7). Individual peaks were back Fourier transformed to determine the amplitude and phase of the peak (Figure 6-8). Using WINXAS to do the fitting, the known anatase sample with six nearest neighbor oxygen atoms at an average distance of 1.94Å fixed the values of E_0 (edge energy), and S_0^2 (amplitude reduction factor). The amplitude and phase information for the samples were then compared with anatase to determine a relative number of nearest neighbors and the average nearest neighbor distance.

XANES

Additional information can be obtained by examining the X-ray absorption near-edge spectra (XANES). The XANES spectra arises from the transitions of electrons to bound excited states on the absorbing atom, but the transitions are strongly modulated by atoms in the surrounding region(<100 absorbing atoms). In particular the XANES can be interpreted empirically to determine the number of nearest neighbor O around the central Ti[59]. The XANES spectra for a variety of titanium compounds have been measured and the variation in the primary peak position seems to indicate the coordination of oxygen with the titanium in the range 3-6[59,60]. XANES also seems to be strongly dependent on particle size and the surface/volume ratio[61].

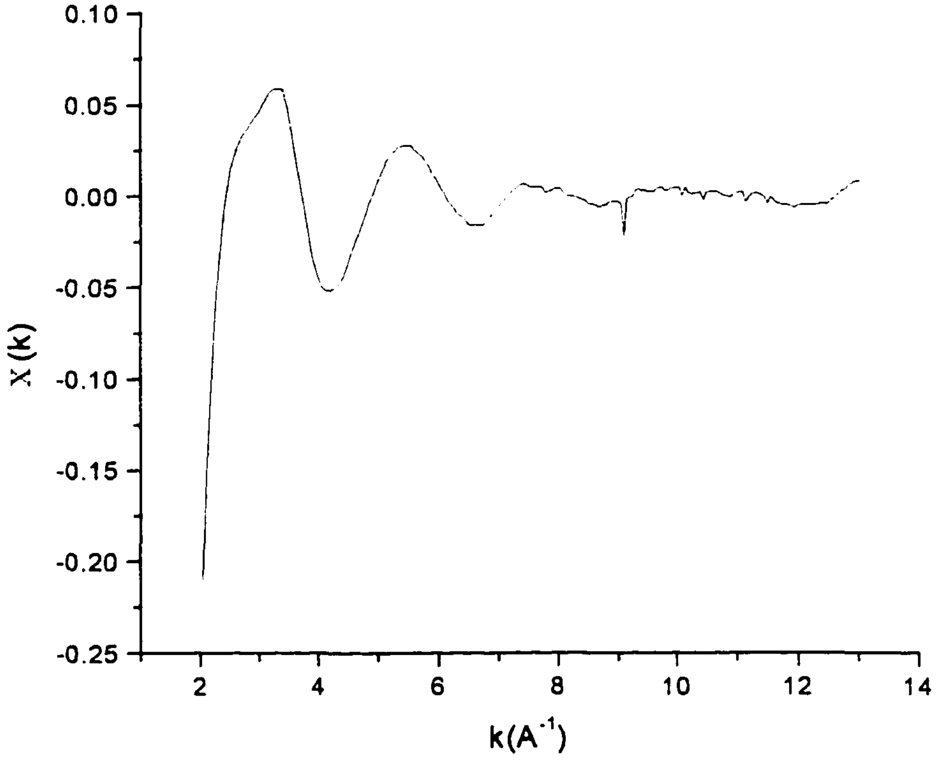

Figure 6-6 After subtracting the spline fit, and converting from energy to wave-vector, the spectra of the TIP is purely oscillatory with decreasing amplitude.

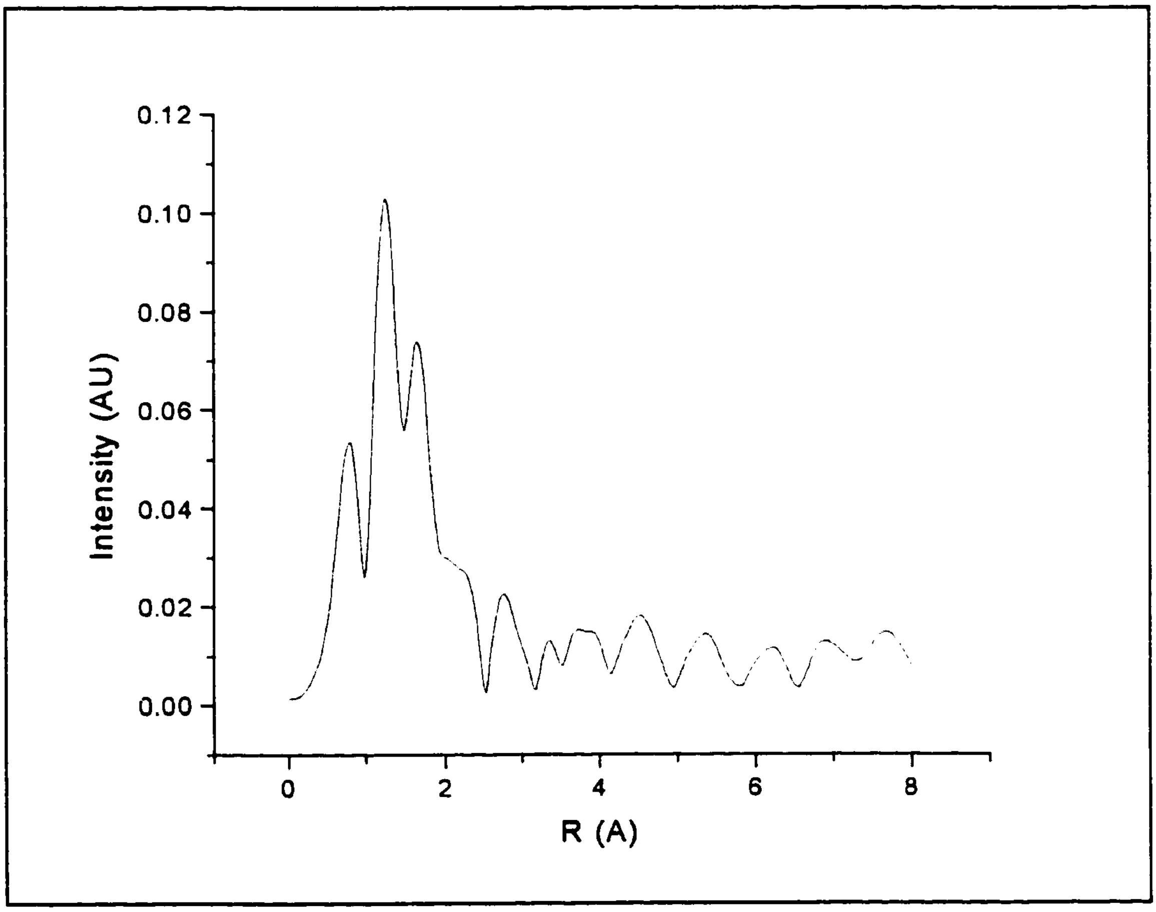

Figure 6-7 The Fourier transform of $k^3 \cdot X(k)$ for TIP.

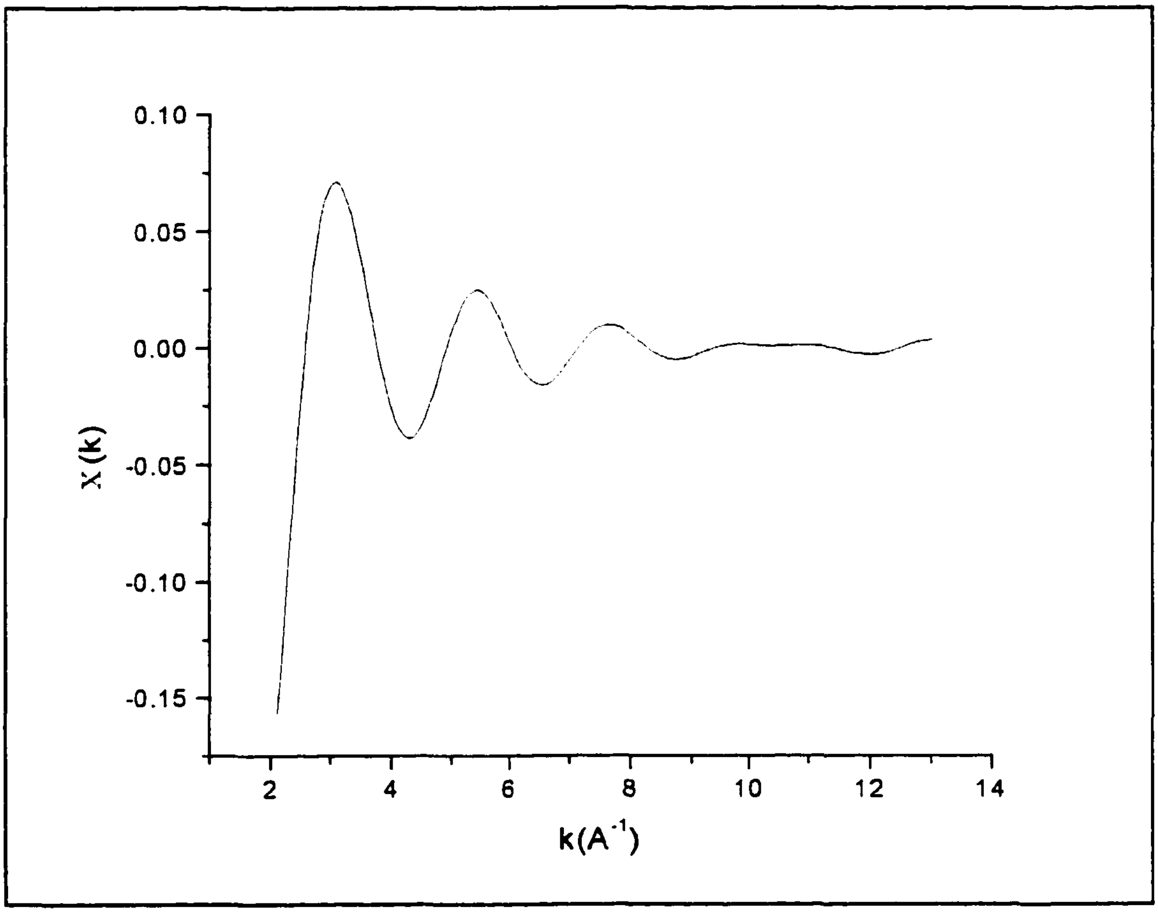

Figure 6-8 Back-Fourier transform of first peak in TIP FT. Analyzing for phase and amplitude and comparing with standard material gives an effective bond length for TIP.

Results

The sol changes very quickly from the TIP almost perfect four-fold coordination to a new, but still four-fold configuration. Analysis of the sol-gel data with TIP amplitude and phase showed very poor convergence. Essentially the peak position of TIP is very far away from the sol-gel samples. Utilizing the anatase data yielded much better results.

The number of nearest neighbors for the core Ti (3.96) does not initially change from that of TIP(3.96), but the initial Ti-O bond length for the sol-gel (1.92Å) is much larger than that of TIP (1.64Å) and quite close to that of anatase (1.94Å). Curiously enough the number of nearest neighbors does not vary much from the initial value of 3.96 but seems to fluctuate, with an average number of nearest neighbors of 3.77 for the whole sol-gel process. The bond length also does not seem to change much but has an average value of 1.90Å for the sol-gel process. The results of fitting for the TIP and the time-evolving sol-gel are shown in Table 6-1. The Debeye-Waller factor, σ^2, is determined by WINXAS during the fitting process and follows the equation of Teo:

$$\sigma_{AB}^{2} = \left\langle (\vec{r}_{AB} \cdot U_A)^2 \right\rangle + \left\langle (\vec{r}_{AB} \cdot U_B)^2 \right\rangle - 2\left\langle (\vec{r}_{AB} \cdot U_A)(\vec{r}_{AB} \cdot U_B) \right\rangle \qquad \textbf{(6-3)}$$

In Equation 6-3, $\vec{r}_{AB}$ is a unit vector along A-B, $U_A(U_B)$ are the instantaneous positions of atom A(B). For crystalline anatase TiO_2, the Debeye-Waller factor has been calculated to be σ^2=0.0010[62,63].

Sample	N (nearest neighbors)	R (Å)	σ^2(Å^2)
Anatase	6	1.94	
TIP	3.96	1.64	.004
Sol age (min)			
5.15	3.96	1.92	.004
6.87	3.83	1.91	.004
8.58	3.70	1.90	.003
10.30	3.66	1.89	.004
12.02	3.94	1.90	.003
13.73	3.78	1.91	.005
15.45	3.72	1.89	.004
17.17	3.61	1.90	.004
18.88	3.73	1.90	.004
20.60	3.76	1.88	.004
22.32	3.77	1.91	.003
24.03	3.82	1.92	.004
25.75	3.80	1.92	.006
27.47	3.93	1.94	.004
29.18	3.65	1.88	.005
30.90	3.76	1.90	.005
32.62	3.59	1.87	.005
34.33	3.85	1.88	.004

Table 6-1 Number of nearest neighbors and distance for the sol-gel evolution as compared with anatase data from the Farel-Lytle database.

Anatase crystal should have a six-fold coordination of O around the core Ti atom. The reduced coordination has been seen however by others working with sol-gel derived TiO_2 xerogels. In particular, Luca et al. found a nearly four-fold coordination for an x-ray amorphous xerogel which had not undergone any aging or annealing after drying. For these samples, a single Ti-O shell was seen to have a coordination of 3.90 and an average bond length of about 1.88Å[63]. In another set of experiments, Manzini et al., found that their sol-gel derived amorphous TIO_2 materials had a nearly five-fold Ti-O coordination and an average bond length of 1.85Å[64] after mild heating.

It seems clear that the EXAFS spectra indicates that although TiO_2 bonding changes from the initial TIP bonding, it is not crystalline. At the heart of this matter is the limit on what size defines a crystallite. For very small crystallites, it is thermodynamically favorable for the amorphous state to form[65]. It has been shown that a stable form of five-coordinate Ti can exist on the surface of anatase crystals[66].

The XANES spectra for the sol also shows good agreement with the literature. There is single pre-edge feature at approximately 4.971 keV which corresponds to a four-fold coordination of Ti-O[67] (Figure 6-9). The data were not taken with XANES measurements in mind, however, so the resolution is not sufficient to see all of the features that should be present in the pre-edge spectra.

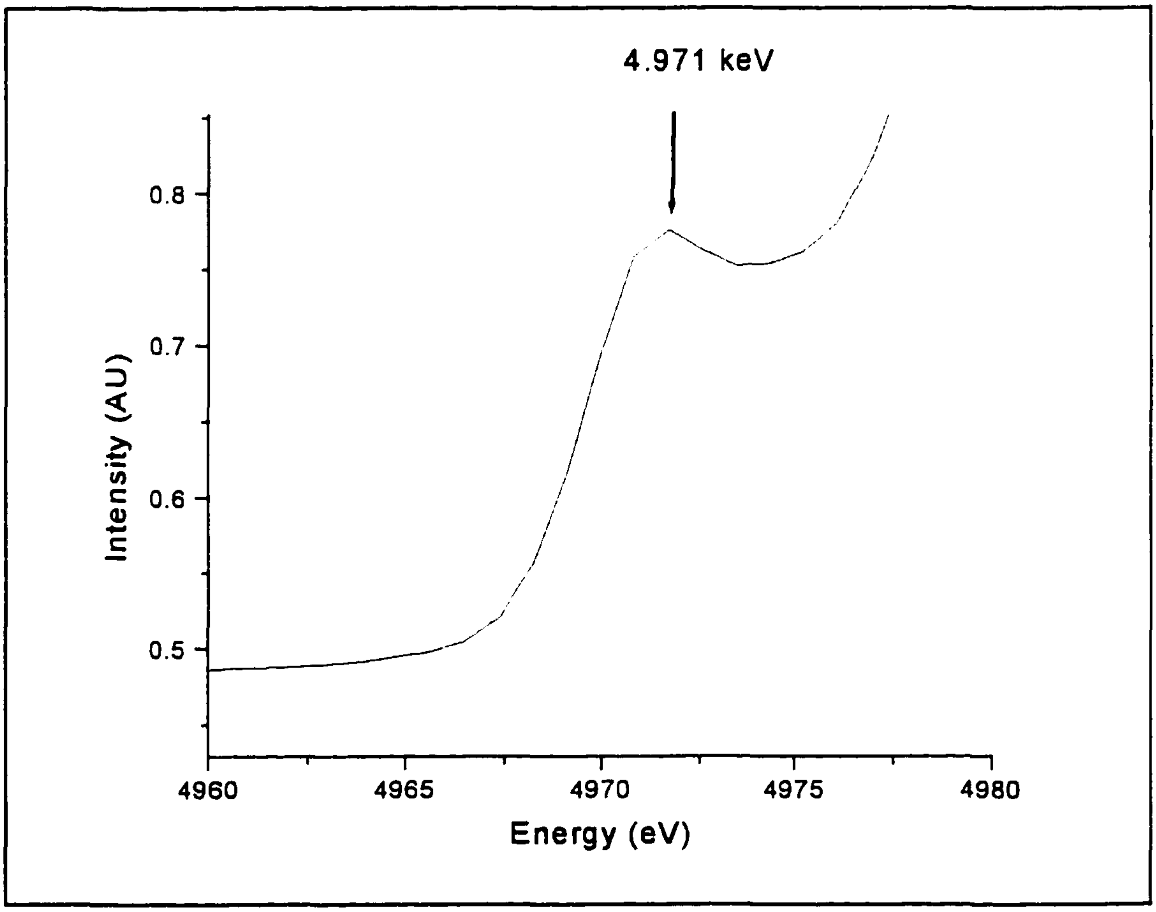

Figure 6-9 The XANES spectra of the TiO_2 sol-gel shows a primary peak at about 4.971 keV which has been shown to correlate with a fourfold Ti-O coordination.

Chapter 7 - Photocatalysis

Theory of Photocatalysis

As a semiconductor, electron hole pairs are excited in the TiO_2 when a photon with energy greater than the bandgap is absorbed. The TiO_2 aerogels have been shown to have a bandgap similar to that of single crystal TiO_2[68]. For anatase the bandgap is about 3.2eV and for rutile it is about 3.0eV. The energy of the holes is about 3eV below the H^+ flat band potential[69]. They have sufficient energy to catalyze any organic substance they comes in contact with. The electron and hole must separate sufficiently and move to the solid-liquid interface where they can chemically interact with the solution. It has been noted by Gerischer that "In a photocatalytic reaction, the rate of oxidation by holes has to be balanced by the rate of reduction by electrons"[70]. If the electrons are not transported chemically to the solution then their buildup on the surface will reduce the number of holes left for catalyzing the oxidation of SA. Gerischer also notes that a material with many shallow surface states (~0.1eV - 0.3eV) can trap electrons at the surface[68]. The reduced mobility of these trapped electrons means they are less likely to recombine with holes at the surface.

The energy band structure at the TiO_2-electrolyte interface has been studied by many people, including Gerischer[19], Graetzel[71] and Siripala[72]. The relationship between the aerogel morphology and photocatalysis has also been studied by us before[73,74,75]. In the interest of standardization, we use salicylic acid (SA) as a "pollutant" in the aqueous aerogel-electrolyte system. We assume that the light intensity is such that photo-decomposition is not rate limited by mass transport, with SA and O_2 chemisorbed concentrations maintained at the surface of the TiO_2 crystallites. In addition the oxygen taking part in the oxidation was only atmospheric oxygen dissolved in the solution. This assumption is reasonable because at normal atmospheric pressure the concentration of dissolved atmospheric O_2 is about 10^{-3} M. Salicylic Acid is oxidized at the surface of the TiO_2 crystallites and eventually is completely oxidized to CO_2 by the following reaction:

$$C_7H_6O_3 + 7O_2 \rightarrow 7CO_2 + 3H_2O \tag{7-1}$$

In determining the effectiveness of a photocatalyst, it is necessary to determine how efficiently light energy is being utilized in the photocatalytic process. Measuring the total reaction rate is difficult to do in practice, because at any one time there may be several byproducts of the initial reaction. We chose to monitor only the concentration of the original Salicylic Acid solution. Concentration is measured by checking UV absorption at 295nm with a Perkin Elmer Lambda 3B UV/Vis spectrophotometer. The SA concentration is determined by the Beer-Lambert Law which linearly correlates the absorbance with concentration for a large range of concentration. In practice the UV absorption at 295nm is measured for several known concentrations, then a fit is obtained which allows interpolation of an unknown concentration. The Quantum efficiency (QE) calculations assume that all light illuminating the aerogel samples is absorbed and refer strictly to the disappearance of SA as measured by absorption not on the formation of a product. The apparatus for the photocatalysis experiments is shown in Figure 7-1 and was designed to allow full absorption of incoming light, regardless of the quantity of TiO_2 present.

Experimental Procedure

The supercritical process involves the washing of ethanol from the pores of the gel by liquid CO_2. Although ethanol removal is sufficient to keep the gel from shrinking due to capillary forces, it is certainly not sufficient to remove all the ethanol from the surface. In particular there is substantial evidence supporting the presence of physically absorbed ethanol on the surface of the dried aerogel[23]. The presence of the ethanol complicates interpretation of the SA concentration measurement as there is a significant absorbance near the 295 SA peak. The absorption can mostly be removed by washing the aerogel multiple times with de-ionized water and draining off the wash water.

Following the washing, 25mL of a starting concentration of 500μM SA solution is added to the reaction vessel along with 50mg of TiO_2 aerogel. The vessel is placed in the dark for a period of time, at least 24 hours, before illuminating it with UV radiation. During the dark absorption phase, 1mL aliquots of the solution were sampled and measured using a Perkin-Elmer UV/VIS spectrophotometer. The aliquot was then replaced in the reaction vessel. Measurement of the absorption of the SA solution was confined to a

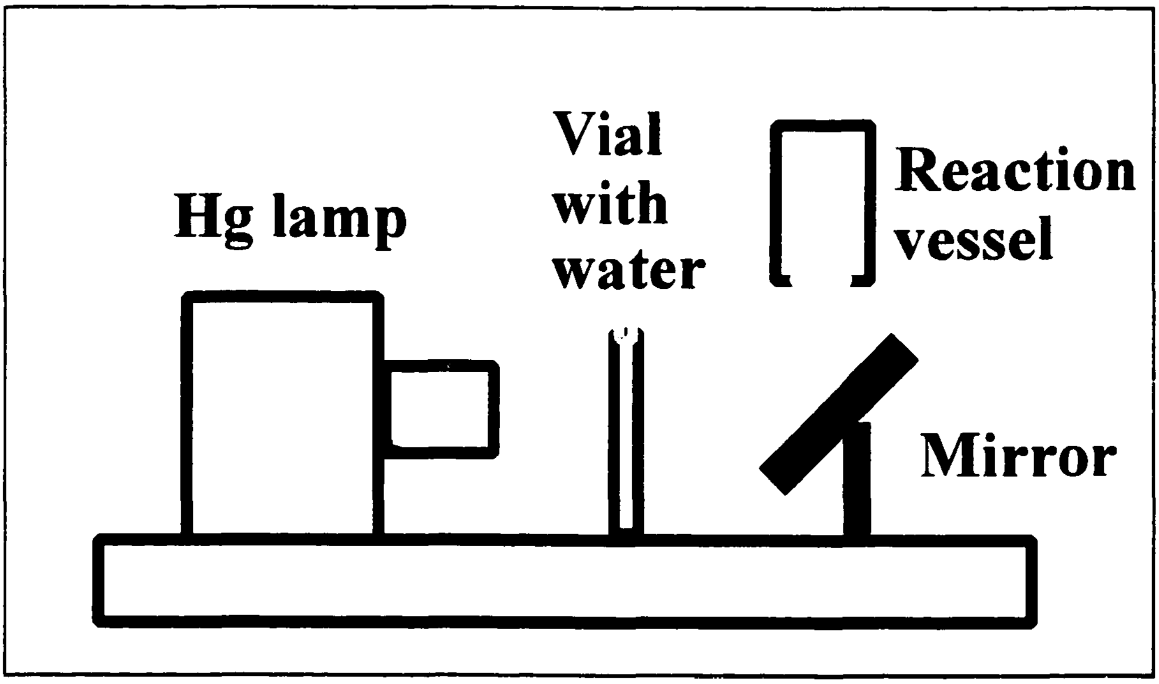

Figure 7-1 Experimental apparatus for photocatalysis. All incident light is assumed to be absorbed by the reaction vessel.

narrow region around 295nm as this was determined to follow the Beer-Lambert law with regard to absorbance concentration. Measuring the absorption spectrum takes approximately 5 minutes.

The samples were illuminated with 500mW of UV radiation as measured by an Eppley light intensity measurement. The distribution of light was measured by a monochromator and from the total intensity, an accurate illumination profile was determined. From the illumination spectrum, an actual photon count was generated for use in quantum efficiency measurements. The reaction vessel was illuminated in fifteen minute intervals, then allowed to equilibrate. The concentration was determined and the samples continued to be illuminated until either the concentration was below a measurable limit of approximately 10μM, or the concentration ceased to decrease. Some samples were then cleaned by repeated washing with de-ionized water and used for further experiments.

Experimental Results

Dark Adsorption

The vessel is kept in the dark for at least 24 hours to allow absorption into the aerogel structure. For the various aerogel samples the dark adsorption is presented in Figure 7-2. Clearly the higher the surface area, the more salicylic acid is removed from the solution during dark adsorption. The thickness of the adsorbed salicylic acid layer can be estimated by assuming uniform coverage of the aerogel surface. For a single crystal

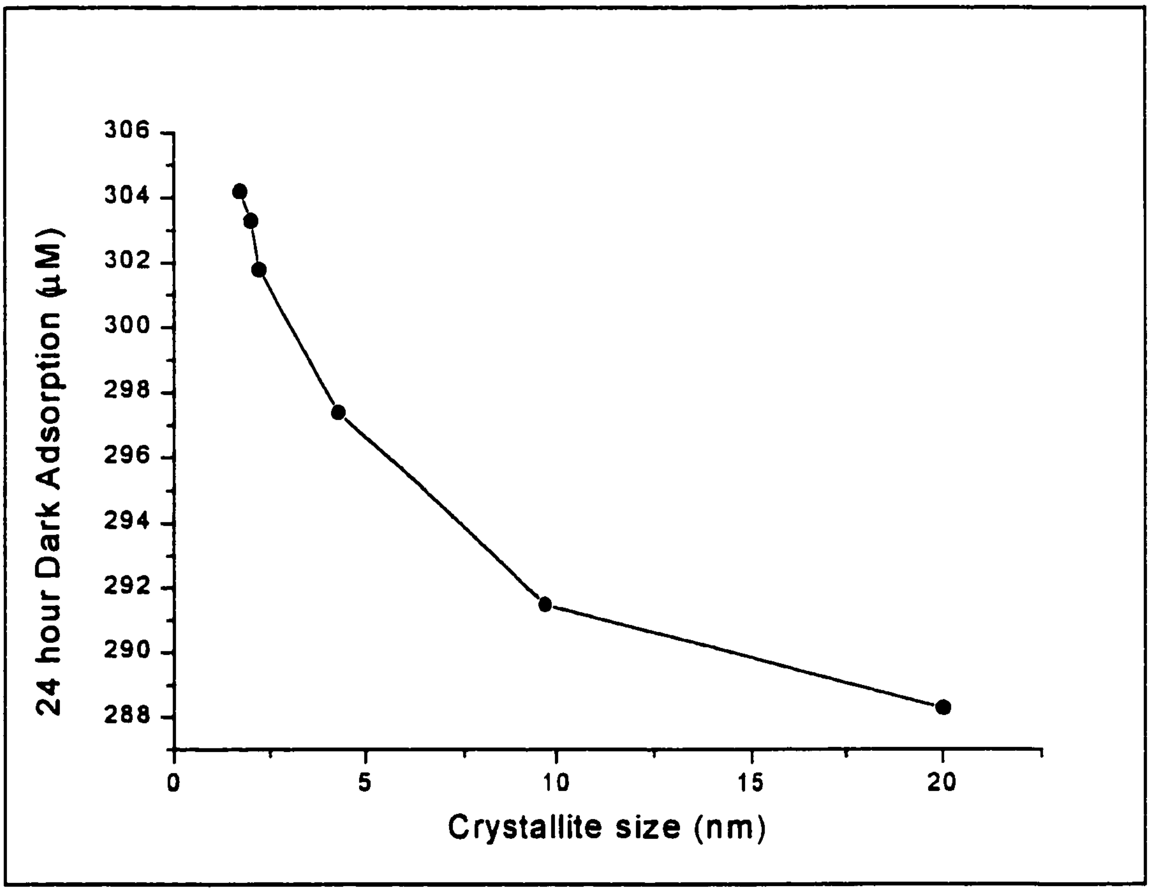

Figure 7-2 The dark adsorption in 24 hours of salicylic acid on the aerogels as a function of crystallite size.

substrate, a reasonable value for monolayer coverage is about 10^{15} molecules/cm^2. The surface coverage for the aerogels and the Degussa P25 is given in Table 7-1.

With increasing surface area, the surface coverage of salicylic acid decreases. Clearly the concentration of salicylic acid is too small to achieve complete coverage of the aerogel surface. In principle, we might expect that the quantum efficiency to decrease with increasing surface area, because not all of the surface area is covered.

Sample	Surface Area (m^2/g)	Crystallite Size (nm)	ΔN (10^{18} molecules SA)	Surface Coverage (10^{11} molecules/cm^2)
Aerogel A	464	1.7	1.831	3.946
Aerogel B	395	2.0	1.825	4.620
Aerogel C	359	2.2	1.816	5.058
Aerogel D	184	4.3	1.790	9.728
Aerogel E	81	9.7	1.755	21.667
Degussa P25	39	>20	1.736	44.512

Table 7-1 The number of molecules of salicylic acid per unit area after dark adsorption on the aerogels and Deguss P25 powder shows ...

After dark absorption the samples are illuminated in fifteen minute intervals, then allowed to equilibrate. In previous work, it was shown that the concentration would continue to drop for several hours after illumination had stopped[76]. Indicating that surface adsorption sites were not being filled as quickly as they were being freed.

Samples were illuminated until they no longer resulted in a drop in concentration. In Figure 7-3 the results of the photocatalysis experiment are shown. The concentration for all of the samples showed a rapid decline, but for decreasing surface area, the final concentration would not go below a certain value. For the all but aerogel E, the aerogel samples were able to clean nearly all of the salicylic acid from the solution. Sample E and the Degussa powder both reach a threshold below which they are unable to remove anymore salicylic acid. One possible explanation might be that the surface sites are being occupied by products of the salicylic acid oxidation. These products were not measured in the UV/Vis absorption, so this remains an unknown.

To compare these materials in another quantitative way, quantum efficiency was determined for the various samples. The quantum efficiency being used here is related to the disappearance of salicylic acid as measured by UV/Vis absorption. The Hg lamp spectra was measured using a monochromator and is shown in Figure 7-4. From the total intensity as measured by a radiometer (Eppley PSP), the photon flux between 300nm and 400nm was determined to be 10^{15} photons/sec. The quantum efficiency for the aerogel samples is shown in Figure 7-5 as a function of BET surface area. The quantum efficiency increases with surface area but seems to reach a plateau.

If we renormalize the quantum efficiency with surface area, it can be seen that the normalized quantum efficiency increases approximately linearly with increasing crystallite size (Figure 7-6). Important to note from this result, the crystalline phase did

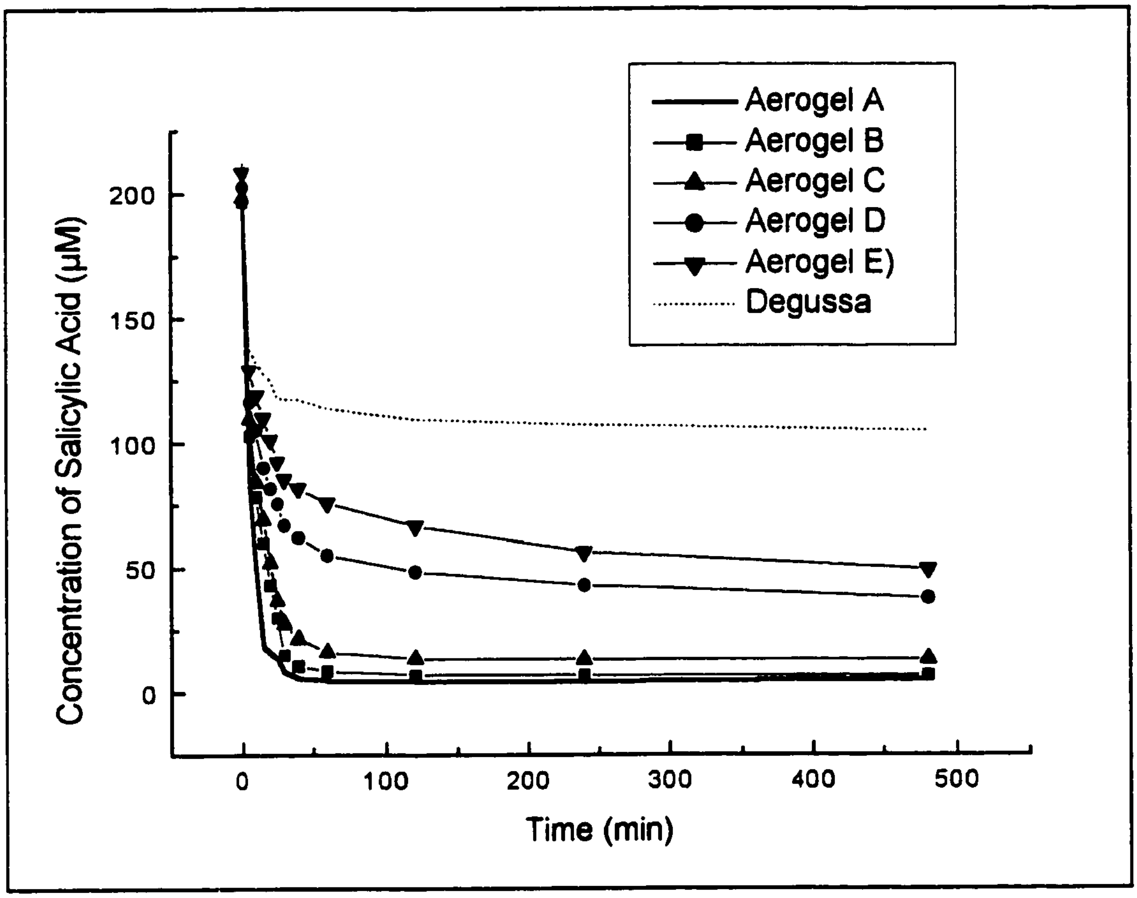

Figure 7-3 The concentration declines to a constant value for various TiO2 samples. The higher the surface area, the more SA was removed from the solution.

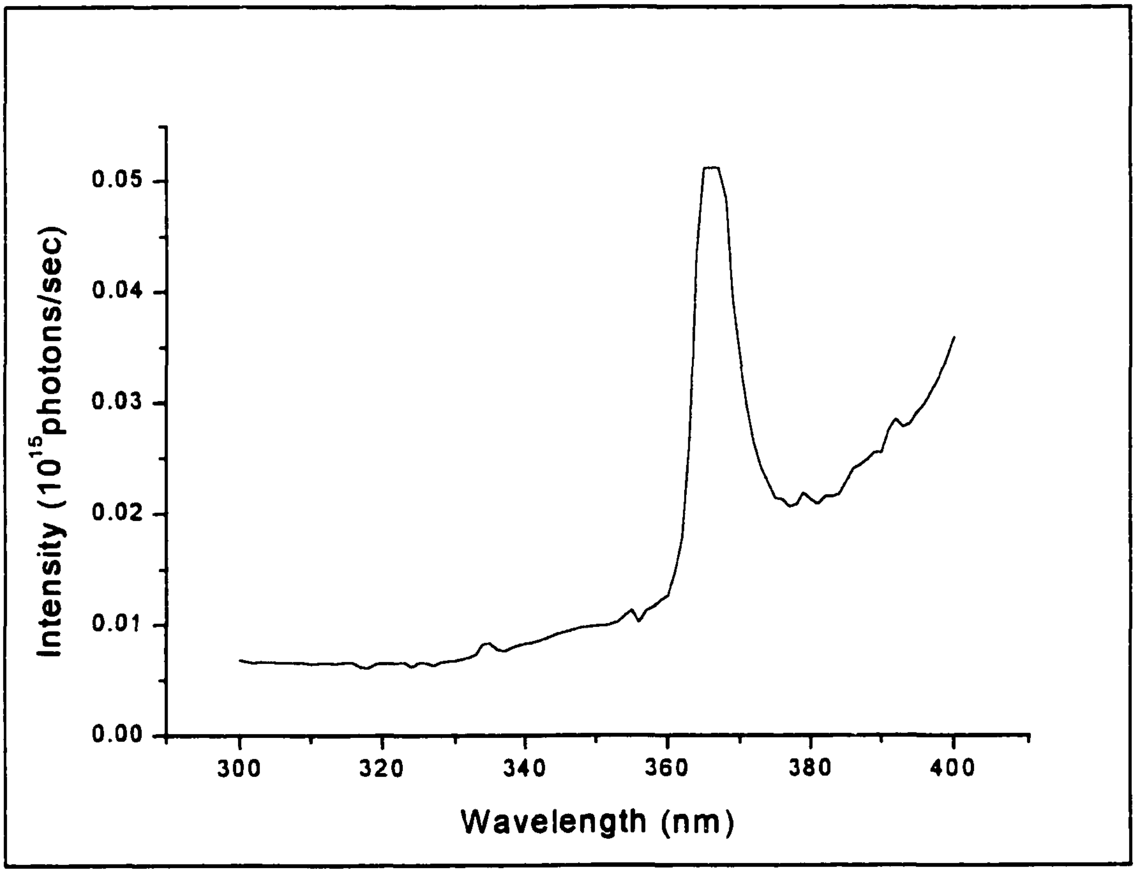

Figure 7-4 The spectrum for the Hg lamp between 300nm and 400nm was calibrated to determine the photon flux.

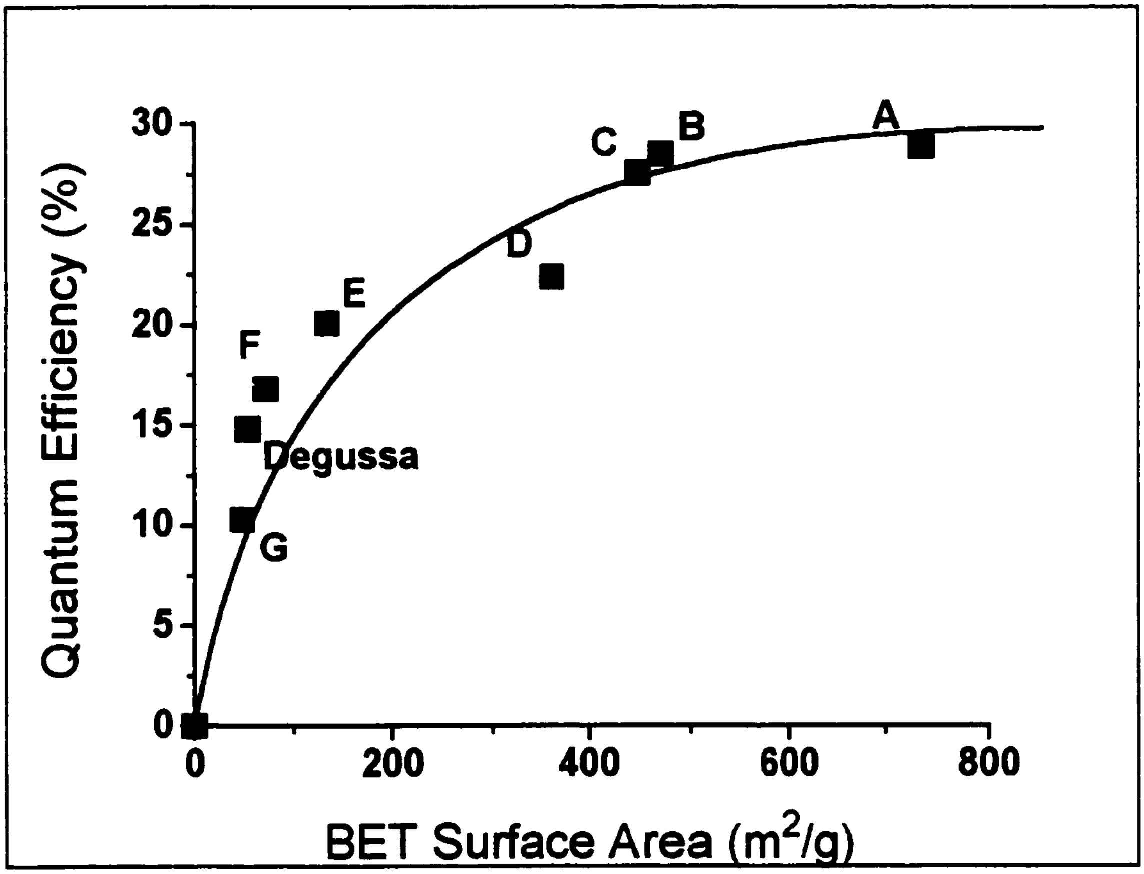

Figure 7-5 The QE increases with increasing SA, but seems to be reaching a plateau. This may be due to the fact that concentrations of salicylic acid were low.

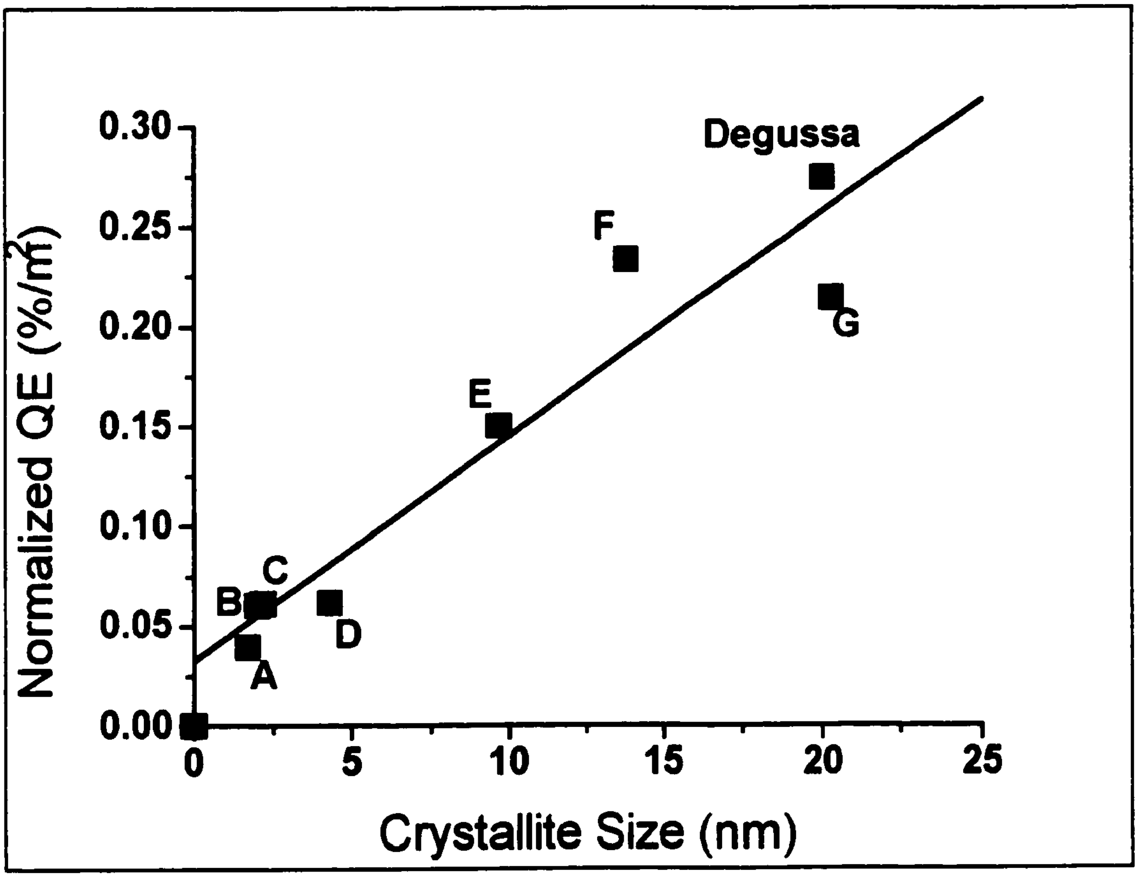

Figure 7-6 The relationship between the normalized QE and the crystallite is roughly linear. It seems to also be independent of crystallite type.

not appear to play a factor in determining the quantum efficiency. Although this may be correct, it may also be a result of using too low a concentration to effectively utilize the whole aerogel surface.

Interpretation

The results in Figures 7-5 and 7-6 can be interpreted in terms of a fragmentation model in which the total surface area scales as 1/grain-size. This is shown schematically in Figure 7-7. Using a fixed mass of aerogel, the average grain size is r, and the density of the

$$N_g = \frac{3}{4\pi\rho r^3} \tag{7-1}$$

material is Δ. Then the number of particles per gram is given by:

The total surface area per gram is then given by Equation 7-2.

If the quantum efficiency is assumed to follow a general form (Equation 7-3):

It assumes that the quantum efficiency is independent of the surface area of the individual

$$SA_{total} = N_g \cdot SA_{nanocrystal} = \frac{3}{\rho r} \tag{7-2}$$

$$QE = \frac{aSA_{total}}{(1 + bSA_{total})} \tag{7-3}$$

$$\frac{QE}{SA_{total}} = \frac{a}{(1 + bSA_{total})} \tag{7-4}$$

particles. Then the normalized quantum efficiency (normalized to total surface area) becomes:

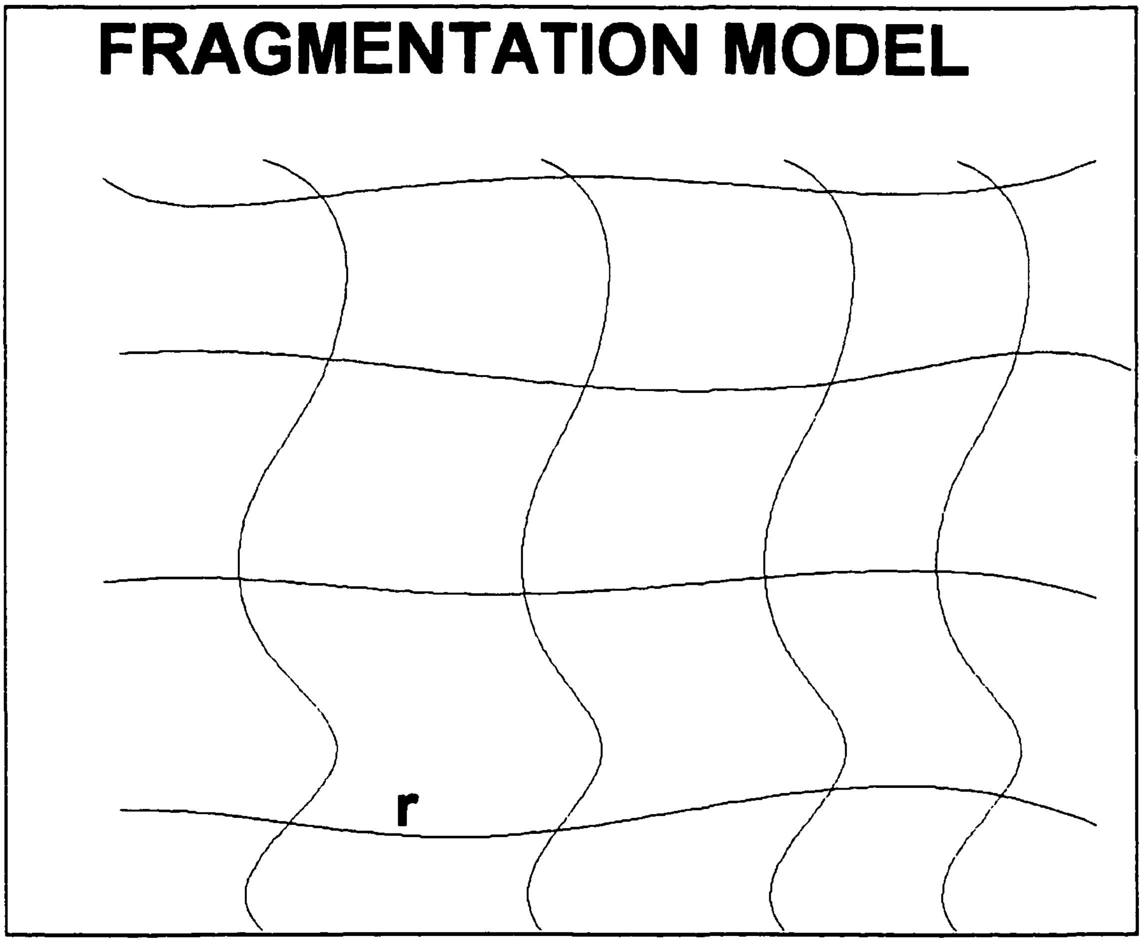

Figure 7-7 The fragmentation model of the aerogel is presented to account for the relationship between normalized quantum efficiency and crystallite size.

In the limit that $bSA_{total} >> 1$, this expression reduces to:

$$\frac{QE}{SA_{total}} = \frac{a}{bSA_{total}} \tag{7-5}$$

Using Equation 7-2 this becomes:

$$\frac{QE}{SA_{total}} = \frac{a\rho r}{3b} \tag{7-6}$$

Which is proportional to the crystallite size, r. A mechanism that will be consistent with quantum efficiency that is independent of the surface area in a system in which the average adsorption is considerably smaller than a monolayer , is based on limited penetration of the substrate into the mesosphere. The measured porosity of the mesospheres is 29%. This is consistent with close-packing and pore size in the neck area of few Angstroms. Such pores constitute a barrier for small molecules such as N_2 and they almost certainly constitute impenetrable barriers for larger organic substrates. A schematic representation of a mesosphere with the differential surface coverage is shown in Figure 7-8.

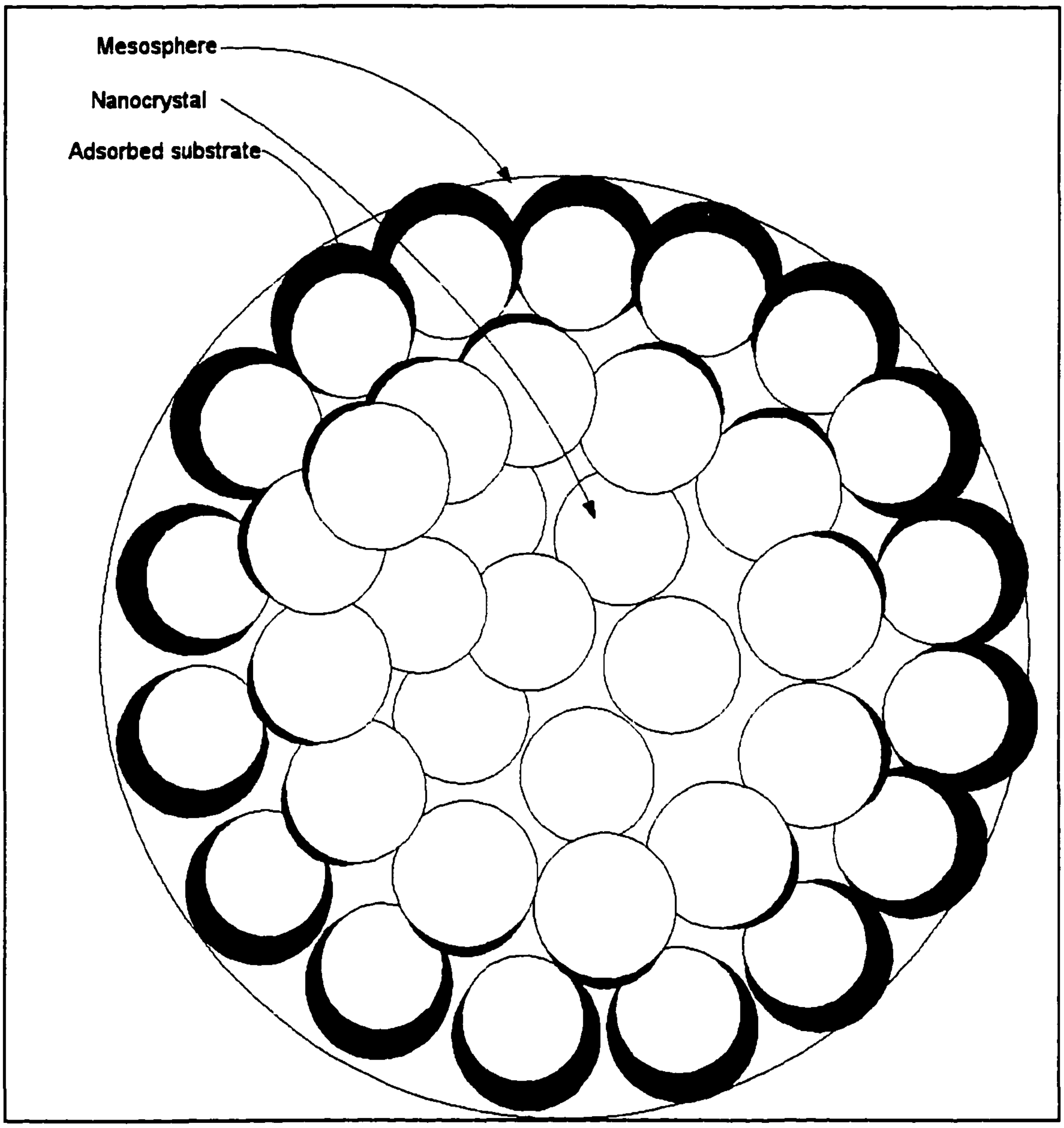

Figure 7-8 The mesosphere coverage is a function of the porosity, with outer nanocrystals receiving a full coverage and inner nanocrystals receiving none.

Chapter 8 - Conclusions and Future Work

The objective of this work was to contribute to the capacity to control aerogel morphology. Specifically, optimizing the morphology of a complex photocatalyst such as TiO_2 aerogels, to achieve better photocatalytic activity under given environmental conditions. The ultimate achievement in this direction will be a photocatalyst that will self-assemble under given environmental conditions, to optimize its photocatalytic activity. The first step in this direction is summarized in Appendix 1, in which is presented the award-winning project of a high school student, Ms. Laurie Ferguson, performed under my guidance, as part of the Intel Science Competition.

The two essential milestones toward achieving this objective are: 1. Development of non-destructive, in-situ, analytical tools that will trace the development of the morphology from its initial precursors toward the final crystallinity and 2. Understanding of the physical, chemical and structural mechanisms that correlate the photocatalytic activity with the morphology. We have clearly achieved important landmarks toward these objectives but it is obvious that an extended further effort is required.

In terms of the morphological dependence of the photocatalytic activity, the results show that the quantum efficiency increases monotonically with the surface area and that the quantum efficiency per unit surface area increases linearly with the size of the nanocrystallites. These results are interpreted in terms of a “cracking model” of fixed size mesospheres and limited penetration of the substrate into the mesospheres. This is an interpretation of the data taken with the macroscopic system, using assumed microstructure of the reactant-mesosphere distribution. A direct evidence can be obtained by examining individual mesospheres with atomic probe microscopies such as AFM and NSOM. An effort in this direction is currently in progress.

In addition, the photocatalytic activity was investigated only under one set of conditions, in terms of light intensity and substrate concentration and adsorption. We expect that the morphological requirements will drastically change with the parameters of the photocatalytic reaction. As an example, under high light intensity in which the diffusion of the reactants and products will be rate limiting, we expect that the pore structure will be of key importance. Again, the ultimate adjustment will be achieved if the catalyst will be able to self-adjust its morphology to achieve optimized performance under given conditions.

In terms of the development of analyticsl techniques that will follow continuesly the development of the morphology and the long range interaction from the monomers to the ultimate crystallinity, we were able to demonstrate a good beginning that is urgently in need of a follow-up.

Both, the Raman and the EXAFS results demonstrate that an identifiable signature of the long range ordering is emerging during the gelation process before the critical point drying step. In the Raman it is the 200cm^{-1} peak that was tentatively identified with a shifted 142cm^{-1} peak of anatase, shifted through the scaling relationship that we have identified for nanocrystalline TiO_2 with different crystallite size. The corresponding finding with EXAFS is the shrinkage of the Ti-O first shell peak from 1.86 Å to 1.6 Å and the emergence of the second-shell peaks at 2.7 Å. Both numbers agree with the published corresponding values for anatase. These findings are new and important for the synthesis of crystalline materials from simple precursors, however, the conclusions are tentative and require further strengthening.

Appendix 1 - Self-Organizing Aerogel

Self-assembly of Titanium Dioxide Aerogels by Inclusion of Degussa P25 Powder

Laurie Ferguson
Midwood High School at Brooklyn College
2839 Bedford Ave.
Brooklyn, NY 11210

Acknowledgments:
Professor Micha Tomkiewicz's laboratory group
& Sean Kelly(Graduate Student)
Brooklyn College: City University of New York
Physics Department
2900 Bedford Ave.
Brooklyn, NY 11210

Abstract

Aerogels are highly porous materials, formed by sol-gel synthesis followed by critical point drying. Aerogels have extraordinary surface areas as high as 1000 m^2/g, and porosities as high as 95%. Titanium dioxide aerogels are excellent photocatalyst capable of quickly breaking down organic pollutants into Carbon Dioxide and water.[1] The aerogel morphology (surface area, porosity, crystalline phase) affects the photocatalytic ability of the aerogel.[2] Changing the morphology affects the available surface as well as the kind of surface seen by the organic molecule. Changes in the synthetic conditions, such as acidity and the presence/absence of light, affect the final morphology of the aerogel. For my project I created a self-modifying gel which automatically responded to varying environmental conditions, such as pH and also different levels of light. These aerogels may be used for decomposing organic waste materials.

Introduction

Aerogels are open pored materials derived from the supercritical drying of highly cross linked, inorganic gels. Due to their properties such as, high porosity of 93-96 percent, and a low density of 0.1-0.3 gm/cm^3, and a very large surface area, aerogels have a large number of practical applications.[3] They are excellent catalysts and insulators as well as detectors. Aerogels are currently being investigated for use in windows and walls as insulators. Silica aerogels have been used as insulating materials in both the Mars Rover and the Hubble space telescope.[4] Carbon aerogels have been shown to work well in desalinating water by dissociation of the water.[5] Aerogels are also being examined for their catalytic properties, to be used in removing impurities from water. Our goal was to modify the environment in which the gel formed, and to determine which factors will increase the aerogels photocatalytic ability.

Self-assembly is a method used to control molecular assembly. In general self-assembly means that a group of objects "assemble" themselves. In our case, the controlled addition of an independent substance, such as Degussa P25, was used to achieve the desired effect. This technique has been very successful in forming nanocomposite films. By the altering the recipe for the polymer by creating positive charges, an electrical attraction can be induced between the different layers of titanium. With this method the layers of titanium can be approximately 3nm thick.[6] This idea of self-assembly is key to the altering of the aerogel structure. Self-assembly usually helps to form more stable and controllable substances.[7]

Self-assembly is a practical concept for the medical world. Self-assembly has been useful in the transfer and formation of medications. Self-assembly is being tested in chemotherapy drugs to prevent the breakdown of the drug by the body, this way the drugs remain active for a longer period of the time. By allowing the drugs to form on their own, researchers have found a way to quickly produce a strong outer layer for the drugs, allow them to arrive at their prescribed destination intact. Self-assembly is also an extremely efficient way to produce organic polymers and manufacture medications. [8]

A magnificent sample of self-assembly is the formation of a pearl. A pearl is made up onion-like layers of mother-of-pearl. When the clam is stimulated, a series of proteins assemble themselves into a scaffolding around the stimulant. This scaffolding becomes the guide for small ceramic plates which create a new outer layer for the pearl.[9]

Another aspect of self-assembly is functional optimization. The particles arrange

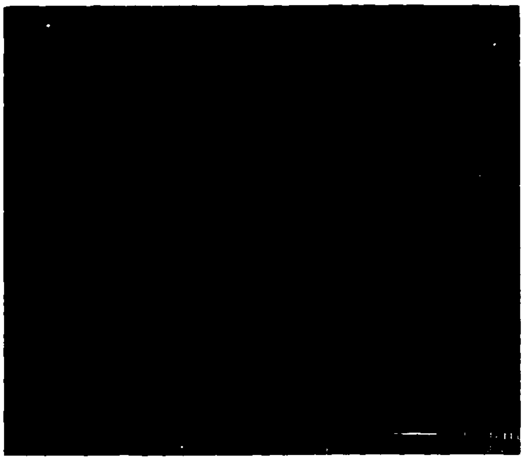

***Figure 1**: SEM image of an aerogel. The structure is extremely porous, and contains clusters of mesospheres.*

themselves to optimize their interaction with the environment. Leaves on trees grow in order to maximize the surface area exposed to light. This is useful to optimize the tree's energy formation and growth.

Aerogels consist of nanocrystals of TiO_2 about 5nm in diameter[10]. The nanocrystals are tightly packed into mesospheres about 50nm. The mesospheres are then loosely arranged into a sponge-like network which is the aerogel.[11]

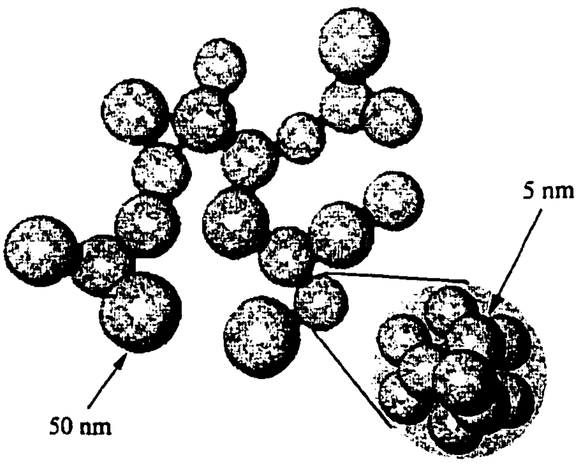

***Figure 2**: Aerogels consist of loosely pack mesospheres approximately 50nm in size. These mesospheres contain tightly pack nanospheres approximately 5nm in diameter.*

The aerogel is formed by sol-gel synthesis followed by critical point drying. Sol-gel synthesis is a process in which metal alkoxides are hydrolyzed and condensed until a gel is formed. A sol is made consisting of Titanium isopropoxide(TiP), ethanol(EtOH), water(H_2O) and nitric acid(HNO_3) in the molar ratio of, 1:25:3.5:0.08. There are two fundamental reactions which lead to the condensation of TiO_2, hydrolysis and alcolysis. The TiP reacts with the EtOH in a hydrolysis reaction as follows:

$$Ti(OPr^i)_4 + H_2O \rightarrow Ti(OPr^i)_3OH + Pr^iOH.$$[12]

The products of the reaction then form Ti-O-Ti chains from:

$$Ti\text{-}OH + Ti\text{-}OH \rightarrow Ti\text{-}O\text{-}Ti + H_2O$$

These Ti-O-Ti chains branch out to form a polymer, then a crystal. A secondary reaction that takes place is alcolysis, which is:

$$Ti(OPr^i)_4 + EtOH \rightarrow Ti(OPr^i)_3OET + Pr^iOH$$

The products again react with each other to form another set of Ti-O-Ti chains

$$Ti\text{-}OEt + Ti\text{-}OH \rightarrow Ti\text{-}O\text{-}Ti + EtOH.$$[13]

The drying of the gel is a critical part in the formation of an aerogel. Liquids in the sol-gel pores adhere to the surface of the gel. While the liquid is evaporating, the surface tension pulls the walls of the gel closer causing the gel to collapse. If the gel collapses, the resulting material (xerogel) will have much smaller porosity and surface area than the aerogel. To prevent collapse due to surface tension, a critical point must be reached. The critical point of a substance is where the liquid and gas state of a substance are equivalent. This eliminates the surface tension as there is no longer a boundary between the two phases.

When aerogels were first made, the sol-gels were heated and pressurized in an autoclave to the critical point of Ethanol in order to remove the ethanol from the pores. This proved to be quite difficult since the critical point for the ethanol is hard to reach at 275°C and 1700psi[14]. In the 1970s, S. Teichner and his graduate students invented a new technique which involved another step. In an autoclave, the ethanol in the gel is replaced with liquid carbon dioxide. Once the ethanol is purged, the chamber is brought to the critical point of carbon dioxide at 35°C and 1100psi. Then the gas-liquid carbon dioxide is removed from the system leaving behind the skeleton structure which is an aerogel. This proved to be a much easier method since the critical point for carbon dioxide is only 1100psi and 35°C.[15]

Titanium dioxide(TiO_2) has many interesting properties. It is used commercially in sun screens due to the fact that TiO_2 absorbs UV light and is highly reflective. Titanium dioxide is also known for its catalytic properties. Chemists have used crystalline TiO_2 as a catalytic surface for many different chemical reactions.[16] Titanium dioxide aerogels can act as catalyst for reactions similar to the use of crystallite TiO_2. Titanium dioxide is a semiconductor and as such, light with energy greater than the band-gap will excite an electron-hole pair. For TiO_2 the band-gap is ~3.2 eV which corresponds to UV light[17]. The hole is the positively charged space left behind when an electron is excited and removed from the valence band. It is the hole which reacts chemically with a material adsorbed on the surface and can break apart even carbon-carbon bonds, which are characteristic of all organic substances. An organic material, such as salicylic acid($C_7H_6O_3$), can be broken down into final products of carbon dioxide and water.

Titanium dioxide can be found in many different forms. Anatase and rutile are two of the crystalline forms that TiO_2 can form. Degussa powder is an example of titanium dioxide powder, made by Degussa which consists of a mixture of rutile and anatase forms of tio2. The crystals that form from a gel contain only anatase. While the Degussa powder has a surface area of only 50 m^2/g, an aerogel has a surface area of 500-1000 m^2/g.

Nitric acid slows the condensation process. This occurs because the presence of the acid allows the break up of the polymer chain by weakening bonds along the end of the chain which can then form newer and stronger bonds. The initial acid molar ratio plays an important role in the formation of the gel and its morphology. It has been found that by controlling the amount of nitric acid the size of the mesopheres can be controlled without significantly altering the surface area of the gel.[18] When the acid content becomes too large, the structures become so tightly bound that they prevent the cross linking of the mesopheres and the formation of the gel.

The aerogel is a catalyst for reactions when exposed to UV light. The sol itself is not sensitive to UV light. If Degussa P25 is added to the sol, it becomes light sensitive. The gel should organize itself in such a way as to maximize the amount of light absorbed by the gel. This would be an ideal way to make the gels, so that their photocatalytic ability is maximized.

I studied and observed the self modifying characteristics of the sol, and the effect of light and nitric acid on the sol and the final product, aerogel. By finding the changes made by the addition of Degussa powder, light and an increase in HNO_3, or acidity of the sol, the differences in the aerogel structure were determined by the surface area measured by nitrogen adsorption, crystallite size through Raman spectroscopy and qualitative properties of the gel. I showed that the aerogel can photo-degrade organic matter efficiently.

Methods

Sample Preparation

First a sol is made by combining 1 part Ti(O-C3H7)4(TiP): 25 parts EtOH: 3.5 parts H_2O: 0.08 parts HNO_3. The total amount of titanium isopropoxide(TiP) is mixed with approximately half the total amount of EtOH. In a separate flask the rest of the EtOH is mixed with the H_2O, and HNO_3. Slowly add the solution of EtOH, H_2O and HNO_3 to the solution containing TiP and EtOH, with a steady stream of drops. The sol was allowed to stir until clear. Then Degussa powder or P25 was added, and the solution was stirred for an additional five minutes to ensure homogeneity. The sol was separated into two containers. One container was placed under a UV light, the other into a dark drawer. A 200 watt mercury arc lamp was used to illuminate the sol and the light was reflected by a mirror. The light shone on the bottom of the container so that it hits the maximum surface of the sol-gel. After the sol forms a gel, it is removed from the UV light and placed into a drawer. In making the samples, the amount of HNO_3 was increased by a molar ratio of 1:0.08 TiP to HNO_3 in making four different samples. The Degussa added was altered, the samples contained either no Degussa, 25mg, 50 or 100 mg of Degussa depending on the sample, creating gels with 0, 1.81%, 3.55%, and 6.85% titanium from the addition of Degussa powder.

Critical Point Drying

A Tousamis Auto SAMDRI-814 critical point dryer is used in order to dry the sol-gel. A sample is placed in a basket in the autoclave, then submerged in ethanol. The chamber is cooled to 0°C. Liquid CO_2 then fills the chamber at 800psi. Once the chamber is filled, the ethanol is purged from the system, a process that takes around one hour. The sample is heated to the critical point of CO_2, 35°C and 1100psi. Then the pressure is slowly reduced while maintaining a constant temperature, allowing the CO_2 to be bled from the system. This leaves only the skeletal structure of the gel, or aerogel behind.

Surface Area

The surface area of the aerogel was found by using the Brunauer-Emmett-Teller(BET) method with a Micromeritics Gemini 2360. The adsorption of N_2 gas was measured as a function of the pressure. The measurements are taken at a constant temperature which is kept a constant by submerging the sample in liquid N_2.

Raman Spectroscopy

The Raman effect refers to the transfer of energy from light to the material. This energy is turned to vibrational energy within the material. The source of light is a He/Ne multi-mode laser tuned to 514.5 nm. Raman spectroscopy is used as a characterization tool for identifying materials as well as determining the purity of a crystal. The matching of a series of peaks in the Raman spectra will determine whether a material is present. The presence/absence of these peaks gives the presence/absence of the material. The Raman spectra also provides information on the average crystallite size and crystallite size distribution. The Q-Vector Relaxation Model(QVRM)[19] model shows the shape and location of individual peaks of the Raman spectra and relates them to the average crystallite size. The QVRM is derived from the uncertainty principle, which states that the position and momentum of a particle cannot be measured with unlimited accuracy.

Photocatalysis

The samples were submerged into a solution of salicylic acid of known concentration. The samples were exposed to ultraviolet light, so that a maximum amount of the sample was exposed to the light. In thirty minute intervals, a small portion of the solution was removed and the absorption of light was measured using a Perkin Elmer Lambda 3B UV/Vis spectrophotometer. The measured sample was then returned to the cell to continue photodegration of the salicylic acid by the aerogel sample.

In determining the concentration of salicylic acid in the solution, the Beer-Lambert Law was necessary. This law states that there is a linear relationship between absorbance and concentration of an absorbing species.[20] Using that law, the formula for a line, $y = mx + b$, and a graph of concentration vs. absorbance for a certain peak of the UV graph, an effective formula can be used to determine the concentration(m) of a solution from the absorbance(x). The absorbance of Salicylic Acid in a 50, 100, 250, and 500g/mL concentration was measured. From the 295nm absorption peak, a linear relationship between the height of the peak and the concentration was derived.

Dark Adsorption

Dark adsorption refers to the adsorption of salicylic acid on the surface of the aerogel. The amount of salicylic acid which will absorb on a surface is related to the available surface area, as well as the adsorption rate. The dark adsorption measurements were taken using a similar method to the photocatalysis measurements. A sample of aerogel was submerged in a solution of salicylic acid. The absorbance of the salicylic acid solution was measured every minute for 3000 minutes, or 50 hours. The concentration of salicylic acid was then determined using the Beer-Lambert Law. The adsorption curve can be used to determine the adsorption rate.

Results/Discussion

Gelation Time

In determining whether changes occurred in the sol-gel, the first indication of modifications in the sol-gel is a change in the gelation time. Gel time is the time from when the sol has completely mixed, until a solid, gel-like structure is achieved. There were very distinct differences between the gelation times of different samples.

Unilluminated Samples	1:0.08 Ti:HNO_3	1:0.32 Ti:HNO_3	**Illuminated Samples**	1:0.08 Ti:HNO_3	1:0.32 Ti:HNO_3
No Degussa	4 hrs	26 hrs	No Degussa	4 hrs	19.5 hrs
1.81% Ti from Degussa	1.5 hrs	43 hrs	1.81% Ti from Degussa	1.5 hrs	19 hrs
6.85% Ti from Degussa	4 hr	45 hrs	6.85% Ti from Degussa	4.5 hrs	22.5 hrs

Table 1: Gel time for samples with extreme(high/low) amounts of HNO_3, and Degussa. One set unilluminated the other exposed to UV light for the duration of time for the sol to form a gelatin structure.

There was a distinct lengthening in the gelation time with an increase in HNO_3 content or a lower pH level. The gelation time ranged from 1.5 hr to 45 hr.

The Degussa powder has an effect on the gelation time with a low concentration of HNO_3. The gelation time decreased with the addition of 25mg of Degussa. The gelation was then increased by the addition of 100mg of Degussa. In the dark, the Degussa may cause an adsorption of ions on the surface. This causes a change in the pH level surrounding the Degussa, or the local pH. The change in the local pH may effect the gelation time for the sol.

Light doesn't appear to have an effect on the gelation time of samples with a low acid concentration. At high acid concentrations the gelation time reverts back to no Degussa conditions, maintaining a time similar to the samples without Degussa added. This could be due to the fact that the absorption of light by the Degussa will counteract the effect of the ion adsorption on the surface of the Degussa.

Syneresis

Before drying the gel, to form an aerogel, a few of the physical properties of the gel were recorded. These were additional indications of modifications in the gel.

Syneresis occurs when the gel pulls away from the sides of the container walls, forming a denser structure. Syneresis occurred mainly in the samples with increased HNO_3. There was an increase in syneresis with an increased amount of Degussa.

Opacity

In addition to changes in the syneresis, there were also changes in the clarity of those gels without any Degussa. There was a decrease in gel clarity with increasing acid ratio. This effect is due to the scattering of light by large particles which are found primarily in the high acid ratio gels. The gels with low acid ratio are nearly transparent. It was difficult to determine if this effect is also present in the samples with Degussa, due to the fact that the Degussa also scatters light strongly.

Gel Strength

A comparative study of the strength of the gel was made. The strength was determined by the ability of the gel to "bounce back." This was a qualitative measurement, but presented a clear difference between the samples.

The amount of Degussa played little part in the strength of the gel. The nitric acid was the factor which showed a change in the gel strength. As the amount of HNO_3 added to the sol increased, the strength of the gel decreased.

Unilluminated Samples	1:0.08 Ti:HNO_3	1:0.32 Ti:HNO_3	**Illuminated Samples**	1:0.08 Ti:HNO_3	1:0.32 Ti:HNO_3
No Degussa	Strong	Weak	No Degussa	Strong	Weak
1.81% Ti from Degussa	Strong	Weak	1.81% Ti from Degussa	Strong	Weak
6.85% Ti from Degussa	Strong	Weak	6.85% Ti from Degussa	Weak	Weak

Table 3: Relative strength/weakness of the gel. Based on the gels comparative ability to "bounce back"

Surface Area

There appears to be an optimization of the surface area for the aerogel with the TiP to HNO_3 molar ratio of 1:0.16. This could be due to a competition occurring between reactions. The amount of HNO_3 acts to increase the surface area of the aerogel up to a point, after that the addition of HNO_3 has a reverse effect. Perhaps the addition of too much HNO_3 hinders an additional reaction. A factor may be the effect of HNO_3 on the condensation process. After a certain concentration of HNO_3 the gel forms a structure so tightly packed that the sol never forms a gelatin structure. Particles that are tightly packed tend to have a smaller in surface area. If so, then the changes in the condensation process become extremely noticeable, especially in the surface area measurements. Further studies of the effect of nitric acid near the TiP acid ratio of 1:0.16 are warranted.

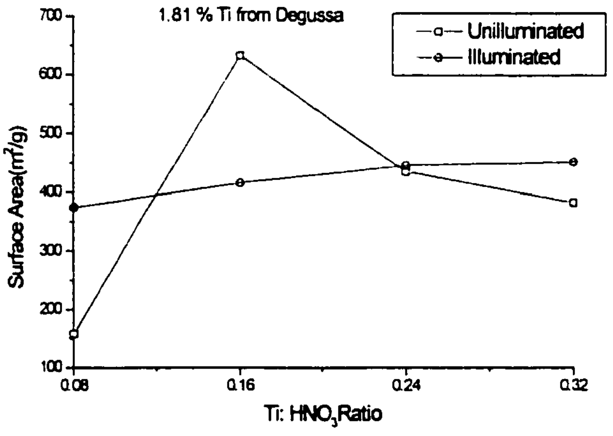

Graph 1: Surface area vs. molar ratio between Ti and HNO_3, for 1.81 % titanium due to the addition of Degussa powder. Comparing the illuminated and unilluminated samples.

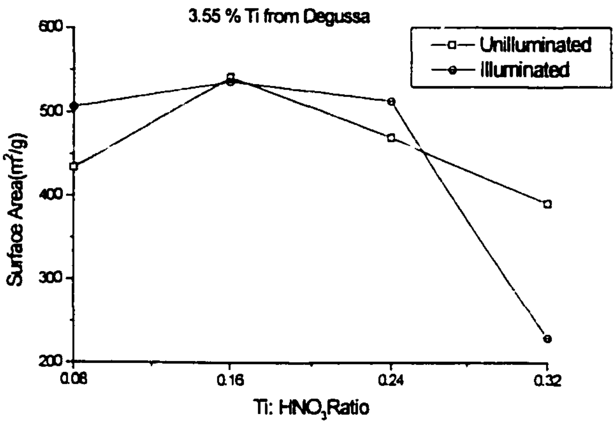

Graph 2: Surface area vs. molar ratio between Ti and HNO_3, for 3.35 % titanium due to the addition of Degussa powder. Comparing the illuminated and unilluminated samples.

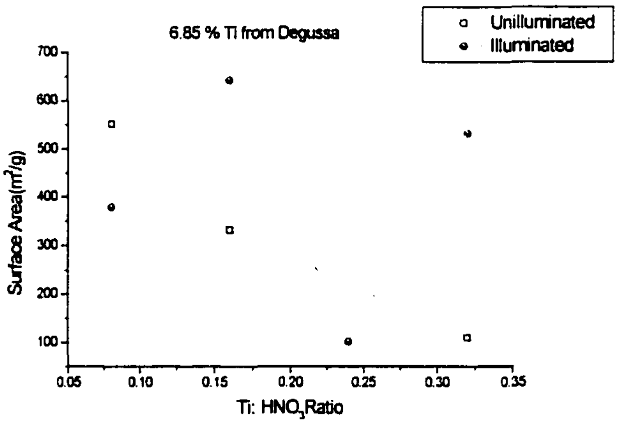

Graph 3: Surface area vs. molar ratio between Ti and HNO_3, for 6.85 % titanium due to the addition of Degussa powder. Comparing the illuminated and unilluminated samples.

Particle Size-Raman spectroscopy

The peaks of the Raman spectra can be analyzed to determine the average crystallite size in the TiO_2 aerogel. In particular the full width at half maximum(FWHM) can be related to the crystallite size through the following equation. [21]

$$\Gamma = k\left(\frac{1}{L^{\alpha}}\right) + \Gamma_0$$

Where α=1.86, Γ_0=8 and k=320. From this equation we can determine the average crystallite size for the various aerogel samples.

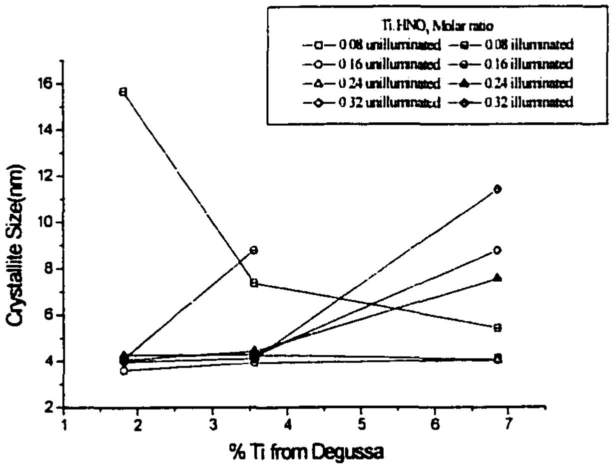

The most significant variation in crystallite size occurred with 6.9% Ti from Degussa. The Degussa is sensitive to light, so it is expected that an increase in Degussa will have an increased effect on the gel. The sample with the molar ratio 0.08 illuminated were set apart from the majority of the samples. The sample with the 0.08 molar ratio was the only one to show a decrease in crystallite size with increasing concentration of Degussa. The sample with 0.16 molar ratio followed the general pattern of an increase in crystallite size with increasing concentration of Degussa, although the effect occurred at a lower concentration of Degussa.

Photocatalysis

Photocatalysis experiments were done in order to prove that the aerogels can completely break down salicylic acid. Figures 5 and 6 show the decrease in the absorbance of the light by the salicylic acid vs. time of illumination of the sample. The absorbance by the salicylic acid is used to characterize the concentration of the solution. The absorbance has a straight line relation to the concentration of salicylic acid, based upon the beer-lambert law. Through this relation it can be determined that the concentration of salicylic acid decreases along with the absorbance.

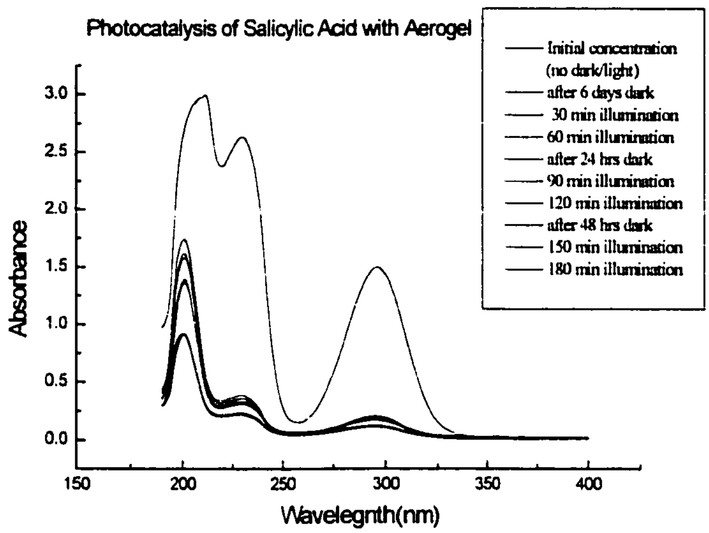

Graph 5: Photocatalysis of salicylic acid using aerogel sample 0.24-100 illuminated. This graph demonstrates the decay of salicylic acid by the aerogel.

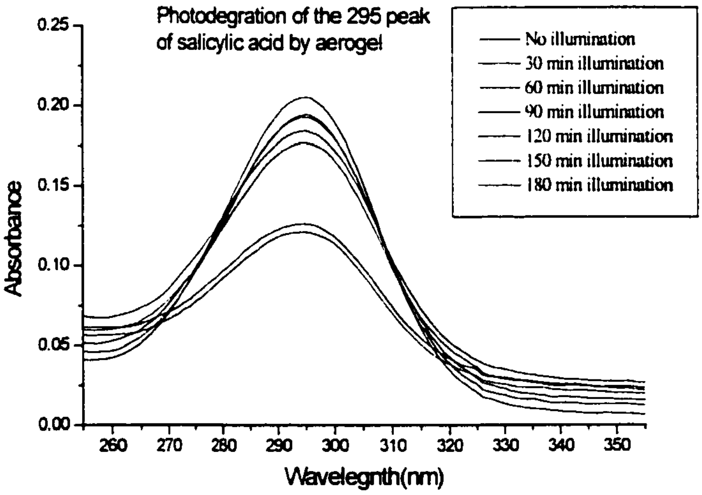

Graph 6: The decay of the 295 peak using aerogel sample 0.24-100 illuminated. The decrease in absorbance is related to a decrease in concentration due to the beer-lambert relation.

Conclusion

We wanted to create a self-assembled aerogel which would tailor itself to changing environmental conditions in particular acid content and illumination. The gel was known to be sensitive to acid content already, and by addition of Degussa P25 we made the gel sensitive to light.

The gel time results showed that the illuminated samples with Degussa P25 powder gelled faster than the unilluminated samples. It was observed that with increasing acid ratio there was increased syneresis, increased opacity and a decrease in gel strength.

The surface area had a maximum value when the sample contained a 1:0.16 molar ratio for TiP:HNO_3. The surface area maximum implies that an optimization is taking place with the effect of nitric acid and Degussa P25 both affecting the gel formation.

The size of the crystallites which make up the aerogel, was greatly affected at the highest Degussa concentration. The sizes of the crystallites varied from 4 to 16 nm in size. For the bulk of the samples there was little variation in crystallite size. This shows that the Degussa had an effect on and, was a factor contributing to the changes in the crystalline size.

By adding Degussa to the sol the sol becomes sensitive to changes in pH as well as changes in illumination. We conclude that factors in the environment of the sol such as pH and light can cause the sol to self-assemble. This could lead to a new class of aerogel materials which can tailor their morphology to optimize their use as photocatalysts in a particular environment.

References

1. Dagan, G.; Tomkiewicz, M. *The Journal of Non-Crystalline Solids*, **1994**, 175, 301-302

2. Ibid

3. Ibid p294

4. Dooling, D.; Porter, L. "NASA/Marshall Aerogel Research and the Rover" Internet. Available. http://www.ssl.msfc.nasa.gov/newhome/headlines/msad08jul97_2.htm, 6/98

5.Carbon-Aerogel Capacitive Deionization of Water. Internet. Available: http://www.llnl.gov/IPandC/op96/03/3b-car.html, 10/98

6. Liu, Y.; Wang, A.; Claus, R. *J. Phys. Chem. B* 1997, 101, 1385

7. Caruana, Claudia M. "AIChE Report: Polymers Gain from Self-Assembly". Internet. Available: http://news.chemicalonline.com/feature-articles/19980519-238.html , Dec. 1998

8. Service, Roberts, Self Assembly Comes Together, *Science*, July 15, **1994**, 256, p316-318

9. Ibid p316

10. Zhu, Z.; Lin, M.; Dagan, G.; Tomkiewicz, M. *The Journal of Physical Chemistry*, **1995**, 99, 15953

11. Ibid

12. Brinker, C.J., ; Scherer, G.W. *The Physics and Chemistry of Sol-Gel Processing*. Academic Press. New York, 1990. Chapter 1

13. Ibid, ch. 1

14.Fricke, Jochen, Aerogels, *Scientific American*, May 88, 256, 92-93

15. Zhu, Z.; Tsung, L.Y.; Tomkiewicz, M. *The Journal of Physical Chemistry*, **1995**, 99, 15945

16. Fujishima, A.; Honda, K. *Nature*, **1972**, 238, 37

17. Dagan, G.; Tomkiewicz, M. *The Journal of Non-Crystalline Solids*, **1994**, 175, 294

18.Suh, D.J.: Park, T. *Chem. Mater.* **1996**, 8, 509-513

19. Kelly, S.; Pollak, F.H.; Tomkiewicz, M. *The Journal of Physical Chemistry B*, **1997**, 101, 2730

20. Tissue, B.M. "SCIMEDIA: Beer-Lambert Law" Internet. Available. http://www.scimedia.com/chem-ed/spec/beerslaw.htm, 12/97

21. Kelly, S.; Pollak, F.H.; Tomkiewicz, M. *The Journal of Physical Chemistry B*, **1997**, 101, 2730

References

1. US News and World Report, "Exxon Valdez revisited", May 12, (1999).

2. Webcrawler Internet search engine results, search for terms '+valdez +"oil spill"', accessed 1 March 1999; available from http://www.webcrawler.com.

3. *T/V Exxon Valdez Oil Spill: Federal On Scene Coordinators Report, Volume 1*, U.S. Coast Guard (1993).

4. Tomkiewicz, M., Ninth International Conference on Photochemical Conversion and Storage of Solar Energy, Beijing, China (1992).

5. Fujishima, A. and Honda, K., Nature **37**, 238 (1972).

6. Daude, N., Gout, C. and Jouanin, C., Physical Review B **15**, 3229 (1997).

7. Glassford, K.M. and Chelikowsky, J.R., Physical Review B **47**, 12550 (1993).

8. Mo, S.D. and Ching, W.Y., Physical Review B **51**, 13023 (1995).

9. Wu, Z.Y., Ouvrard, G., Gressier, P. and Natoli, C.R., Physical Review B **55**, 10382 (1997).

10. Wu, Z.Y., Ouvrard, G., Gressier, P. and Natoli, C.R., Physical Review B **55**, 10385 (1997).

11. Berger, H., Tang, H., and Levy, F., Journal of Crystal Growth **130**, 108 (1993).

12. Krishnamurthy, N. and Haridasan, T.M., Indian Journal of Pure and Applied Physics **17**, 67 (1979).

13. Ohsaka, T., Izumi, F. and Fujiki, Y., Journal of Raman Spectroscopy **7**, 321 (1978).

14. Dupont, *Ti-Pure homepage*, accessed 17 December 1999; available from http://www.dupont.com/tipure/index.html, Internet.

15. Ohko, Y., Tryk, D., Hashimoto, K. and Fujishima, A., Journal of Physical Chemistry B **102**, 2699 (1998).

16. Vidal, A., Chemosphere **36**, 2593 (1998).

17. Zeltner, W.A., Hill C.G. Jr. and Anderson, M.A., Chemtech **23**, 21 (1993).

18. Serpone, N., Lawless, D. and Pelizzetti, E., *Fine particles Science and Technology: From Micro to Nanoparticles*; Pelizetti, E., Ed., Kluwer Academic Publishers, Boston,

MA, 657 (1996).

19. Gerischer, H., Electrochimica Acta **38**, 3 (1993).

20. Brus, L.E., Journal of Physical Chemistry **79**, 5566 (1983), **80**, 4403 (1984).

21. Tsu, R. and Ioriatti, L., Superlattices and Microstructure **1**, 295 (1985).

22. Höfler, H.J., Hahn, H. and Averback, R.S., Defect Diffusion **75**, 195 (1991).

23. Dagan, G. and Tomkiewicz, M., Journal of Non-Crystalline Solids **175**, 294 (1994).

24. Brinker, C.J. and Scherer, G.W., *Sol-Gel Science*, Academic Press, Boston, MA, 599 (1990).

25. Kistler, S.S., Journal of Physical Chemistry **36**, 52 (1932).

26. Meyer, T., *The NASA Stardust homepage*, accessed 17 December 1999; available from http://stardust.jpl.nasa.gov/photo/aerogel.html, Internet.

27. Gesser, H.D. and Goswami, P.C., Chemical Reviews **89**, 765 (1989).

28. Nicolaon, G. and Teichner, S.J., Journal of Chemical Physics **65**, 1480 (1968).

29. Zhu, Z., Lin, M., Dagan, G. and Tomkiewicz, M., The Journal of Physical Chemistry **99**, 15950 (1995).

30. Zhu, Z., Lin, M., Dagan, G. and Tomkiewicz, M., The Journal of Physical Chemistry **99**, 15945 (1995).

31. Brinker, C.J. and Scherer, G.W., *The Physics and Chemistry of Sol-Gel Processing*, Academic Press, New York, NY, Chapter 1 (1990).

32. Iida, Y., Furukawa, M., Kato, K. and Morikawa, H., Applied Spectroscopy **51**, 673 (1997).

33. Suh, D.J. and Park,T., Chemistry of Materials **8**, 509 (1996).

34. Brinker, C.J. and Scherer, G.W., *The Physics and Chemistry of Sol-Gel Processing*, Academic Press, New York, NY, Chapter 3 (1990).

35. Rangarajan, B. and Lira, C.T., The Journal of Supercritical Fluids **4**, 1 (1991).

36. Campbell, L.K., Na, B.K. and Ko, E.I., Chemistry of Materials **4**, 1329 (1992).

37. Li, F. and Lannin, J.S., Applied Physics Letters **61**, 2116 (1992).

38. See for example, Eisberg, R. and Resnick, R., *Quantum Physics Of Atoms, Molecules, Solids, Nuclei, and Particles*, John Wiley & Sons, New York, NY , Chapter 3 (1985).

39. Merle, P., Pascual, J., Camassel, J. and Mathieu, H., Physical Review B **21**, 1617 (1980).

40. Bobvich, Ya.S., Vovk, S.M., Petrov, V.I., Tsenter, M.Ya. and Sharygin, L.M., Optical Spectroscopy (USSR) **59**, 834 (1985).

41. Doss, C.J. and Zallen, R., Physical Review B **48**, 15626 (1993).

42. Kelly, S., Pollak, F.H. and Tomkiewicz, M., Journal of Physical Chemistry **101**, 2730 (1997).

43. Pollak, F.H., *Analytical Raman Spectroscopy;* Grasselli, J.G. and Bulkin,B.J., Eds., John Wiley & Sons, New York, Chapter 6 (1991).

44. Bersani, D., Lotticci, P.P. and Ding, X.-Z., Applied Physics Letters **72**, 73 (1998).

45. Hart, T.R., Aggarwal, R.L. and Lax, B., Physical Review B **1**, 638 (1970).

46. Porto, S.P.S, Fleury, P.A. and Damen, T.C., Physical Review **154**, 522 (1967).

47. Private correspondance with Ladislav Kavan, EPFL, Lausanne, Switzerland.

48. Traylor, J.G., Smith, H.G., Nicklow, R.M. and Wilkinson, M.K., Physical Review B **3**, 3457 (1971).

49. Persans, P.D., Tu, A., Wu, Y.-J. and Lewis, M., Journal of the Optical Society of America B **6**, 818 (1989).

50. Zallen, R., *The Physics of Amorphous Solids*, Wiley, New York, NY, 89 (1983).

51. Nakamura, K., Fujitsaka, M. and Kitajima, M., Physical Review B **23**, 6348 (1981).

52. Best, M.F. and Condrate, R.A., Sr., Journal of Material Science Letters **4**, 994 (1985).

53. Kozlowski, R., Pettifer, R.F. and Thomas, J.M., Journal of Physical Chemistry **87**, 5172 (1983).

54. Vlaic, G., Bart, J.C.J. and Cavigiolo, W., Z. Naturforschung **36a**, 1192 (1981).

55. Teo, B.K., *EXAFS: Basic Principles and Data Analysis*, Springer-Verlag, New York, NY, Chapter 2 (1986).

56. Lide, D.R., *CRC Handbook of Chemistry and Physics 71st Edition* , CRC Press, Boston, MA, 10-271 (1990).

57. Boyanov, B, *Farrel-Lytle Memorial Database*, database of EXAFS data taken mostly by Farrel, accessed 17 December 1999; available from http://ixs.iit.edu/database/data/Farrel_Lytle_data/index.html; Internet.

58. Ressler, T., Journal of Physics IV, **7**, 269 (1997).

59. Farges, F., American Mineralogy **92**, 44 (1997).

60. Wu, Z.Y., Ouvrard, G., Gressier, P. and Natoli,C.R., Physical Review B **55**, 10382 (1997).

61. Chen, L.X., Rajh, T., Wang, Z. and Thurnauer, M.C., Journal of Physical Chemistry B **101**, 10688 (1997).

62. Howard, C.J., Sabine, T.M. and Dickson, F., Acta Crystallografica **B47**, 462 (1991).

63. Luca, V., Djajanti, S and Howe, R., Journal of Physical Chemistry B **102**, 10650 (1998).

64. Manzini, I., Antonioli, G., Lottici, P., Gnappi, G. and Montenero, A., Journal of Non-Crystalline Solids **192**, 519 (1995).

65. Sun, N.Y. and Lu, K., Physical Review B **59**, 5987 (1999).

66. Primet, M., Pichat, P. Mathieu, M.-V., Journal of Physical Chemistry **75**, 1221 (1971).

67. Farges, F., American Mineralogist **92**, 44 (1997).

68. Gerischer, H. and Heller, A., Journal of the Electrochemical Society **139**, 113 (1992).

69. Bard, A.J. and Wrighton, M.S., *Semiconductor Liquid-Junction Solar Cells*, proceedings Volume 77-3 of The Electrochemical Society, 195 (1977).

70. Wang, C.M., Heller, A. and Gerischer, H., Journal of the American Chemical Society **114**, 5230 (1992).

71. Kavan, L., Gratzel, M., Gilbert, S.E., Klemenz, C. and Scheel, H.J., Journal of the American Chemical Society **118**, 6716 (1996).

72. Siripala, W., PhD Dissertation, *Study of Surface States at the Semiconductor/Electrolyte Interface of Liquid-Junction Solar Cells*, City University of New York, NY (1983).

73. Tomkiewicz, T. and Kelly, S., *Fine Particles Science and Technology, From Micro to Nanoparticles*, Pelizetti, E., Ed., Kluwer Academic Publishers, Boston (1996).

74. Tomkiewicz, M and Kelly, S., *Nanoparticles in Solids and Solutions*, Fendler, J., Ed., Wiley, Boston (1998).

75. Kelly, S., Shen, W.-M. And Tomkiewicz, M., *Nanostructured Materials in Electrochemistry*, Searson, P. and Meyer, G.J., Eds., Electrochemical Society, Boston (1995).

76. Tomkiewicz, M., Dagan, G. and Zhu, Z., Research on Chemical Intermediates **20**, 701 (1994).